SPUTTER DEPOSITION PROCESSES FOR THIN FILM OXIDE DIELECTRICS

A Dissertation

Presented to the Faculty of the Graduate School

of Cornell University

in Partial Fulfillment of the Requirements for the Degree of

Doctor of Philosophy

by

Sara Cordero Barron

January 2009

SPUTTER DEPOSITION PROCESSES FOR THIN FILM OXIDE DIELECTRICS

Sara Cordero Barron, Ph.D.

Cornell University 2009

As new semiconductor systems are developed and implemented in niche or mainstream applications, the need for new dielectric materials becomes prevalent. Sputter deposition is a versatile approach to preparing candidate materials for thin film dielectrics, affording a large processing space for optimization. The choices made for these sputtering parameters can effect significant variation in dielectric properties. We find that for the complex amorphous dielectric oxide of $Zr_{0.2}Sn_{0.2}Ti_{0.6}O_2$, the dielectric constant is strongly dependent on substrate temperature during reactive sputter deposition, with ε_r ~55 if deposited at 150 to 280 °C; at higher and lower temperatures, the dielectric constant falls to ~30-35. A high quality dysprosium-substituted titania is prepared by reactive RF sputter deposition on unheated substrates. Preparation by thermal oxidation of a sputtered metal film, however, results in an oxide with a defect polarization along phase boundaries. Finally, we develop a methodology to co-sputter dielectric oxides in a composition gradient. When deposited from an oblique sputtering source, such as that used in composition spreads, dielectric thin films exhibit an abnormal low frequency polarization. We implement a negative electrical bias to the substrate, which eliminates the void-mediated polarization and recovers the intrinsic properties of the dielectric. The validity of this technique is demonstrated in the model system Ta_2O_5. Implementation of the technique and its implications for resputtering are considered in the mixed TaO_x-GeO_x dielectric system.

BIOGRAPHICAL SKETCH

Sara Barron was born May 24, 1980, in Chattanooga, Tennessee, to Dan and Mila Barron. Two years later she was joined by her sister Kathleen. The family lost Dan to cancer in 1988, but his mark–pride in hard work and personal integrity–was already firmly in place. Mila took it upon herself to continue his lessons with her own courage and love.

Sara was additionally blessed with a strong education and dedicated teachers. Her first years at Saint Jude School were filled with love and important lessons on family, generosity, and justice. Her high school teachers at the Girls Preparatory School sought to foster in her and her classmates a clarity of thought and of written and spoken communication. Mrs. Carolyn Chandler and Mr. Keith Sanders stand out in particular for lending invaluable support as Sara developed some confidence in her voice.

In 1998, Sara finished high school and left Chattanooga for undergraduate work in Boston, Massachusetts. Sara and Kathleen were in many ways inseparable through the Chattanooga years, and Kathleen joined her in Boston three years later. In 2002, Sara received a bachelors of science in Course III (Materials Science and Engineering) from the Massachusetts Institute of Technology. Her most important lessons during these years in Massachusetts may not have been along the Infinite Corridor, but in a yellow Victorian house in Brookline. With her housemates at Epsilon Theta, she found the freedom to explore science and friendship without prejudice.

In August 2002, Sara journeyed west to Ithaca, New York, and joined the Cornell Department of Materials Science and Engineering. It is here that she learned about materials.

ACKNOWLEDGEMENTS

This thesis and my time here at Cornell benefitted from the feedback, support, and friendship of many people. I would like to thank my advisor Bruce van Dover for his guidance and resourcefulness in my development not only as researcher but also as a professional. Professors Jack Blakely and Chris Xu were generous in their time and feedback in reviewing my dissertation. Thank you.

Many collaborators have contributed to this work. Jaegoo Lee was a fearless and patient co-worker, who integrated my dielectrics into his non-volatile memory device (and provided lots of useful feedback along the way). Lena Fitting Kourkoutis provided beautiful TEM images. There have been a host of talented undergraduate and M. Eng. students whose hard work and creativity I co-opted to my latest "theory" and whose company I enjoyed: Bryan McGowan, Daniel Ruebusch, John Hevey, Maxim Noginov, Leo Small, and José Fonseca. My labmates, Jon, John, Steve, Karen, Mark, Noble, Maxim, Totka, and Rob have been invaluable resources for equipment questions, constructive criticism, and company. Thank you all for (so pleasantly) enabling so much of my work here.

Outside of the department, I have been refreshed and strengthened by our Monday (or Tuesday) night Emmaus group, my companions on the road: Matt, Lori, Jolanda, Sabrina, Michael, Katie, and Sister Donna. And I have found a home in the welcome and comfort of my roommates and their associated four-legged furry companions: Azadeh, Corinne, Sarah, Jon, Simon, Pudge, Joe, K. R., and Tamino. Thank you to all of these for sharing my every-day.

Finally, I have not enough words of gratitude for my family. Thanks to my Mamie, the bravest lady I know, who knew how to give her girls every good thing. And to Kathleen, who knows my weaknesses better than any and still expects the world of me. I think the world of you, bean.

TABLE OF CONTENTS

LIST OF TABLES

LIST OF FIGURES

CHAPTER 1

INTRODUCTION

The drive for smaller, cheaper, or faster electronics is motivating a drive toward the material research and development that will enable these electronics. One of the key materials systems in any electronic device is the dielectric material. In the past year, microprocessor manufacturers have integrated hafnium-based dielectric oxides and metal gates into mainstream silicon integrated circuits [1]. Simultaneously, new semiconductor systems such as organic and polymeric semiconductors are being developed and implemented in niche and increasingly mainstream applications [2]. As new semiconductor materials and applications come to fruition, the need for new dielectric materials–new processing windows, requirements for new and different properties–becomes prevalent.

Fundamentally, high κ dielectrics are electrical insulators with significant polarizability in an electric field. The high polarization in an electric field enables a high charge buildup on the oxide's electrodes at a minimal voltage applied; this minimizes the power necessary to switch a transistor, for example. In contrast, low κ dielectrics minimize the charge density even at high voltages and are an important material for electrical isolation of closely spaced metal interconnects in integrated circuits [3].

In the following sections, we motivate the study of high κ dielectrics by considering applications which rely on well-understood dielectric oxides. In doing so, we discuss both the state of the art in academic research and also current industry standards. Additionally, we discuss the available deposition techniques for inorganic oxide thin films, including our deposition choice of sputtering.

1.1 Motivation: thin film dielectric oxides

There are two predominant applications for high κ thin film dielectrics: storing charge, e.g. the capacitor in dynamic random access memory (DRAM) cell, and gating charge, e.g. the gate dielectric in a metal-oxide-semiconductor field effect transistor (MOSFET) [4]. In both applications, the historical dielectric choice has been silicon dioxide or silicon oxynitride [4]. In the following sections, we motivate the study of alternative dielectrics by considering the inability of silicon dioxide to meet application demands in the coming years.

1.1.1 Dielectrics for logic devices on silicon

The bulk of research in dielectrics is dedicated to the pressing need for a robust dielectric material on silicon. Silicon semiconductors are the workhorse of complementary metal oxide semiconductor (CMOS) integrated-circuit technology. The requirements for its dielectric are stringent and for many years were amply filled by silicon's own oxide, SiO_2. Silicon dioxide enables excellent performance with its stable interface with silicon and its high electrical breakdown field, commonly 10-15 MV/cm [5].

The concerns surrounding silicon dioxide's use as a dielectric stem from the decreasing size (scaling) of MOSFETs. The integrated circuit (IC) industry is driven to fabricate increasingly smaller transistors both to increase the number transistors per chip and to decrease the channel length. Shorter channel lengths in transistors enable faster processing speeds, but also require scaling of other transistor dimensions, namely the thickness of the gate dielectric oxide.

The necessity of scaling the gate dielectric thickness is predicated on the increasing areal capacitance required to maintain the transistor's drive current. The drive current I_D is

$$I_D = \frac{W}{L}\mu C_{\text{inv}}\frac{(V_G - V_{\text{th}})^2}{2} \tag{1.1}$$

in which W and L are the channel width and length, respectively, μ is the carrier mobility in the channel, C_{inv} is the capacitance of the gate in inversion, V_{th} is the semiconductor's threshold voltage, and V_G is the voltage applied to the gate [6]. We assume the mobility and threshold and gate voltages constant and consider the capacitance and device geometry. For the simple planar metal-oxide-semiconductor gate structure shown in Figure 1.1, the gate capacitance C is given by

$$C = \frac{\varepsilon_o \varepsilon_r A}{d} \tag{1.2}$$

in which A is the gate area (= $W \times L$, in this case), ε_o is the permittivity of free space (=8.85×10^{-12} F/m), ε_r is the permittivity of the dielectric, and d is the dielectric thickness.

Scaling the channel length and width to 70%, as is commonly done at each successive generation of IC circuit technology, requires a 50% increase in areal capacitance, $C/A = \varepsilon_o \varepsilon_r / d$ to maintain the same drive current. The engineering choices then are to decrease in the thickness of the SiO_2 gate dielectric or to implement a dielectric material with a higher permittivity than SiO_2 with ε_r = 3.9.

Switching of transistors requires a gate voltage maintained across the gate oxide; as the thickness of the oxide approaches a nanometer, a very significant current (~100 A/cm^2) flows in response to the gate voltage [8]. Leakage or tunneling currents across the gate oxide increase power consumption and may lead

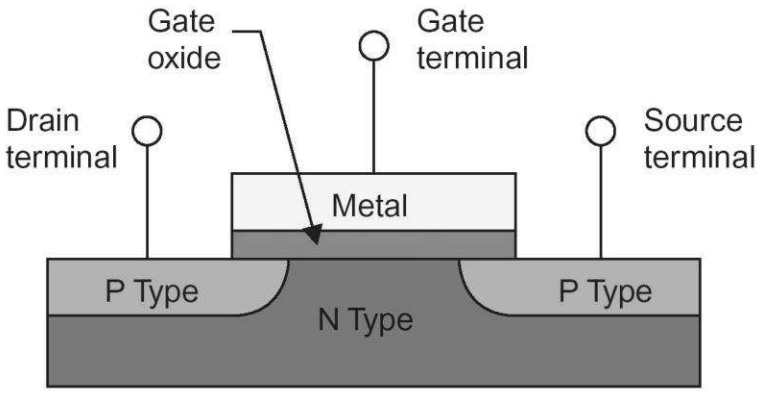

Figure 1.1: Schematic drawing of a MOSFET. From Reference [7].

to heat dissipation concerns [5]. In 2007, technology relied on an SiO_2 gate oxide at 1.2 nm thickness [9].

At these dielectric thicknesses, electron leakage current through the gate is dominated by electron tunneling from the gate electrode to the conduction band of the semiconductor; tunneling through this triangular barrier is known as Fowler Nordheim tunneling. The tunneling probability Θ increases exponentially with decreasing thickness of the gate dielectric, according to

$$\Theta = \exp \frac{-4\sqrt{2qm^*}\phi_B^{3/2}}{3\hbar E} \tag{1.3}$$

in which q is the carrier charge, m the carrier effective mass, ϕ_B the , E is the electric field. The electric field is the voltage drop across a distance d, leaving $\Theta \propto \exp -d$

Classical (continuum) models such as Equation 1.3 require quantum mechanical corrections at these distances, and Lo and co-workers have developed a quantum-mechanical model for tunneling probabilities through an SiO_2 layer <40 [8]. They find that oxide thicknesses <20 may allow tunneling currents of 1 A/cm^2 at a gate voltage of 1.5 V. Gate leakage currents of this density are negli-

gible compared to source–drain currents, but the power consumption is beyond specifications for heat dissipation [8].

In addition to high leakage across nanometer-scale SiO_2, the bulk dielectric constant itself is not realizable in the thinnest oxide layers. Electron energy loss spectroscopy by Muller *et al.* indicates that the minimum thickness for 'bulk' properties is 0.7 nm, or alternatively that the first 0.7 nm is 'interfacial' SiO_2, and that the minimum thickness of a gate oxide is 1.4-1.5 nm [10].

Realizing a high areal capacitance and low leakage currents may seem incompatible priorities, given their dependence on dielectric thickness. However, areal capacitance may be additionally increased with an increase in dielectric constant. The dielectric constant is a material property dependent on chemical composition, bonding structure, and density. Thus, even as we reach fundamental physical limitations of continued scaling of SiO_2 gates, a new dielectric material with a higher dielectric constant ε_r may buy the electronics industry several more generations of continued increases in areal capacitance.

Current research in alternative dielectrics

We have argued that a dielectric material with a $\varepsilon_r > 3.9$ is required to increase oxide thickness while maintaining the areal capacitance. A number of materials have been considered for this duty with dielectric constants ranging from 7 to 100+. The dielectric constant of a material is dependent on the polarizability of electron clouds and ionic bonds. We defer a discussion of the detailed relationship between dielectric constant and polarization mechanisms to Section 2.1 and here discuss some of the materials chosen thus far.

Of primary importance in choosing a new dielectric material is the integration of the new material with silicon or other semiconductor. The first, largely incremental improvement to SiO_2 was the transition to silicon oxynitride, SiO_xN_y. Silicon nitride has a dielectric constant of 7 and can be mixed uniformly in silicon dioxide, raising its dielectric constant slightly [6]. A surprisingly effective improvement was research into substituting small amounts (<6%) of zirconium [11] and hafnium [12] into silicon dioxide. These can bring the dielectric constant up to 9.5, a significant enhancement over an extrapolation between the dielectric constant of ZrO_2 and SiO_2 [13]. Neither nitrogen nor these small amounts of hafnium and zirconium disrupt the high quality interface of SiO_2 with silicon [11, 12], and in the case of small amounts of nitrogen, may improve the interface quality [14].

The interface with silicon is more problematic with non-silicate materials, some of which have significantly higher dielectric constants. A comparison of commonly studied oxide dielectrics is given in Table 1.1. Materials with dielectric constants greater than 20 are required for future electronics generations [9].

Marginally higher dielectric constants have been realized for alumina ($\varepsilon \sim 8$) and for hafnium, zirconium, and lanthanum aluminates and silicates. Recent research has focused on ZrO_2 and, especially, HfO_2.The pure transition metal oxides have dielectric constants of ~25; the dielectric constant decreases with increasing amounts of silicon or aluminum oxide, which stabilize the amorphous phase [18].

There are many other concerns for gate dielectrics than the dielectric constant, including thermodynamic stability on silicon, carrier mobility in the vicinity of the oxide-semiconductor interface, band gap, band offset from the semi-

Table 1.1: Properties of alternative dielectrics. *a*: Ref. [15], *b*: Ref. [16], *c*: Ref. [17]. All others from Reference [6] and references therein.

Material	Dielectric constant, ε_r	Band gap (eV)	Breakdown field (MV/cm)	Material structure
SiO_2	3.9	9	10-20	amorphous
SiO_xN_y	4-7	5.3[a]	10-20	amorphous
Al_2O_3	9	8.7	4-5[b]	amorphous
Y_2O_3	15	5.6	3-4	amorphous
HfO_2	25	5.7	4	polycrystalline
ZrO_2	25	7.8	4	polycrystalline
Ta_2O_5	23	4.4[c]	4	amorphous
TiO_2	60-100	3	1	amorphous to polycrystalline
$(Ba,Sr)TiO_3$	300	3	1	crystalline

conductor bands, and leakage currents. Hubbard and Schlom [19] have analyzed the thermodynamic stability of unary oxides in contact with silicon at 1000 °C and have suggested that rare earth oxides, group II oxides, and several other transition metal oxides, including HfO_2 and ZrO_2, may be stable. Notably, they concluded that the oxides of tantalum and titanium were thermodynamically unstable.

Thermodynamic stability can fall victim to kinetic reactions in non-equilibrium deposition processes, however, as evidenced by the admittedly thin, interfacial hafnium silicate layers found by Lee *et al.* when depositing HfO_2 on silicon [20]. The thickness and composition of an interfacial silicate is

the ultimate limit for scaling the gate oxide thickness and is a strong function of the deposition conditions and techniques. The impact of university research is therefore limited in the integration field, and industrial leaders pursue their own in-house research, evidenced most recently by Intel's 2007 integration of a hafnium-based dielectric oxide in its 45 nm node transistors [1].

Mixing of dielectric materials, in hopes of realizing the best properties of each constituent oxide, has been a significant research area, including studies on Ti-Al oxides [21], Hf-Al oxides [18], Hf-Ta oxides [17], Hf-Ti oxides [22, 23], and lanthanum-Ti oxides [24, 25, 26]. The pairing of titanium with another oxide dielectric is a common theme. Titanium dioxide has a high polarizability (ε_r ~35 to 110) but considerable variation in its dielectric properties [6, 27] and is not considered thermodynamically stable on silicon [19]. Its band gap is low for a dielectric, ~3 eV, and leakage current densities have been a concern [27]. An amorphous oxide solution with another dielectric oxide–one with higher band gap, lower leakage, better thermal stability, but lower polarizability–is has been considered a good compromise [21, 17], though comparisons to the pure oxides in the same test has been limited.

Thus far, pure titanium oxide and barium-strontium titanate ((Ba,Sr)TiO_3, or BST), which has a higher dielectric constant yet, have not been aggressively pursued for use as gate dielectrics. BST presents a significant integration challenge. BST also incorporates heavy metals, traditionally avoided in industrial silicon lines due to trapping levels and the lack of appropriate etchants. Its high dielectric constant is observed because at room temperature it is close a ferroelectric transition; at the transition temperature (which depends on the Ba:Sr stoichiometry), the dielectric constant increases rapidly. Like all known materials with a

ferroelectric transition, BST is crystalline. Thus far in gate dielectrics research, crystalline materials have been avoided because of the high temperatures required for crystallization and the challenges of lattice matching to a crystalline channel, though there is promising research on this front [28]. Poly-crystalline materials lead to spatial fluctuations in polarization on the order of the grain size, giving rise to a scattering mechanism in the semiconductor channel that reduces mobility. Additionally, there is the suggestion that poly-crystalline materials suffer from higher leakage currents along grain boundaries. This assumption is often made though experimental evidence is lacking, and crystalline materials may be critical in the future both to take advantage of crystalline materials close to their ferroelectric transition and to stabilize an epitaxial interface against subcutaneous oxide formation [4, 28].

Use of titania or BST as a gate dielectric will require a significant paradigm shift in terms of processing expectations, possibly even the shift to a new workhorse semiconductor. Most recently, these dielectrics have been pursued for other applications, including thin film memory devices.

There are accompanying materials challenges in high-κ gate dielectrics integration: polycrystalline silicon (polysilicon) will be replaced by metal gates to optimize the charge injection barrier and to minimizethe small charge screening in the metal gate that results in an undesirable series capacitance.

1.1.2 Dielectrics for memory applications

Dielectrics in memory applications are primarily charged with storing electrons, for which they require high areal charge densities and low leakage

($J < 10^{-8}$ A cm^{-2}). On the other hand, since no carrier transport is required on the electrodes, the quality of the interface is crucial only for minimizing the interfacial reactions that decrease capacitance, not for carrier mobility at the interface region [6].

Alternative dielectrics are used in both in volatile and non-volatile memory devices. Non-volatile memory, such as FLASH memory, is an archival memory, and writing is much slower than in dynamic random access memory (DRAM) [4]. These memory devices require charge storage on metal particles embedded in the gate dielectric of an adapted transistor. DRAM is a volatile memory which employs a MOSFET switch to charge an MIM capacitor. The memory is stored as either a '0' or '1', depending on the charge stored on the capacitor. At each generation, the area of the capacitor decreases but charge stored remains constant, requiring an increase in areal capacitance [4, 29].

For the DRAM MOSFET, the industry roadmap [9] calls for an areal capacitance equivalent to that achieved by 5.0 nm of SiO_2, while for the DRAM capacitor, the required equivalent SiO_2 thickness is 0.9 nm. In the case of DRAM, then, the dielectric material for the capacitors is the more pressing concern than the dielectric material for the MOSFET switch. Industry has already moved from silicon dioxide and silicon oxynitride dielectrics to Ta_2O_5 ($\varepsilon_r \sim 23$) and has additionally implemented trench gate structures to increase capacitor areas [4, 29]. BST is also a candidate dielectric, but is still in a research phase for many of the reasons cited in the previous section [4, 29].

1.2 Motivation: sputter deposition

To prepare dielectric oxides for evaluation, we choose sputter deposition. Sputtering affords a straightforward approach to preparing candidate materials for thin film dielectrics. Sputtering unary oxides requires no preparation of precursor materials, only a sputter target of the cation metal or the metal oxide. Targets for mixed oxides can be prepared by metal or ceramic processing of the constituent materials; the target material does not need to be atomically mixed as it deposits as atoms or dimers. Mixed oxides are also prepared by simultaneous or sequential sputter deposition from several metal or metal oxide targets. In our research group, we exploit the geometry of multiple sputter targets held at oblique angles to the substrate to create samples with a gradient in composition as a function of physical position on the sample [30]. Only directional deposition techniques such as sputtering enable depositions of such composition gradients.

While sputtering is a common tool in researching dielectric oxides (see, for example, References [21, 31, 32]), other deposition techniques predominate in industry for deposition of the dielectric oxides. Chemical vapor deposition (CVD) and its derivative process atomic layer deposition (ALD) are more common for depositing the dielectric material in high performance transistors [6].

Chemical vapor deposition, along with its many derivatives, is a versatile deposition technique for oxides, nitrides, carbides, and metals [33]. The desired film components are introduced into the reaction chamber as volatile compounds which react in the gas or on the substrate [33].

ALD is a related technique, which relies on sequential introduction of each

precursor compound into the chamber, separated by vacuum pumpout or purging cycles of argon [34]. Precursors are chosen which do not self-react, and because each precursor is introduced individually, only a monolayer of material can be deposited with each cycle. For oxide deposition, a volatile compound of the metal ($AlCl_3$, $Al(CH_3)_3$, or $TiCl_4$, or $HfCl_4$) is sequentially introduced with water vapor [35]. The technique affords strong control of the oxide thickness and conformity to step edges, highly desirable for the convoluted structures of non-planar transistor geometries [36, 37].

A rarely discussed issue is the incorporation of impurities into deposited material. Both sputtering and CVD techniques lead to the inclusion of impurities due to the deposition gases: argon in sputtered films [38] and carbon or chlorine in CVD [39, 37]. Though the effect of the impurities are often ignored, they can contribute to defect states in the insulator [40, 41].

Depending the allowable processing conditions, other deposition conditions are possible. In the less stringent paradigm of polymer electronics with its emphasis on low cost, solution processing and spin casting of dielectric materials are implemented.

Recently, Van Elshocht and co-workers at IMEC in Belgium have developed an aqueous solution technique for preparing Nd_2O_3 [42] and ZrO_2 [43]. A solution containing the cation precursor is spin cast on to a silicon wafer and annealed on a hot plate in air; the technique offers low equipment and material costs, and the film quality approaches that of ALD prepared films [43]. Deposition of inorganic materials from solution has occasioned enough interest to support a symposium during the Fall 2008 Materials Research Society (MRS) Conference, titled “Low-Cost Solution-Based Deposition of Inorganic Films for

Electronic/Photonic Devices."

1.3 Executive summary

Many qualities can affect a material's suitability as a dielectric, including polarizability, leakage current, crystallinity, and chemical reactivity. These are considered in this thesis. There are others: cost, ease of processing, and integration into the current processing norms, etc. These are covered only briefly or neglected in this thesis.

Since dielectric measurements are a particularly sensitive probe of defects, interface quality, and growth conditions, this thesis also covers considerations for sputter depositions of many oxide materials. In particular, ion bombardment, resputtering, and interference among neighboring sputter sources are considered in off-axis, multisource configurations and on-axis, alloy target configurations. These are contributions to the field of reactive sputtering of oxides for any application.

We choose to evaluate dielectric properties in metal-insulator-metal (MIM) capacitors, with noble metal electrodes to allow evaluation of the material properties without consideration of the chemical interaction with a semiconductor (e.g., Si). In Chapter 2, we describe our thin film deposition technique as well as measurements of the MIM capacitors.

In Chapter 3, we discuss a complex amorphous dielectric oxide of $Zr_{0.2}Sn_{0.2}Ti_{0.6}O_2$ that has a dielectric constant of ~55, but only if deposited at substrate temperatures of 150 to 280 °C; at higher and lower temperatures, the

dielectric constant falls to ~30 due to crystallization and low density, respectively.

Deposition parameters other than substrate temperature can also have a strong effect on the dielectric properties of an oxide. In Chapter 4, we consider a dysprosium-substituted titanium oxide. When prepared by reactive RF sputter deposition, $Ti_{0.7}Dy_{0.3}O_{1.7}$ has a dielectric constant 24, low leakage current, and low dispersion up to 1 MHz. Dielectric properties are substantially different when the metal is deposited and then thermally oxidized.

In Chapter 5, we describe the effect of ion bombardment on sputter deposited dielectric oxides by considering the particular case of 90° off-axis sputtering. When deposited from an oblique sputtering source, such as that used in composition spreads, the thin film is subject to a low level of bombardment. Applying a negative electrical bias to the substrate during deposition affords control over the level of bombardment by Ar^+ ions in the plasma. Densification of the film by ion bombardment eliminates a low frequency void-mediated polarization, which could mask the intrinsic properties of the dielectric material. The effect is demonstrated in the well-studied model dielectric Ta_2O_5 and the results are implemented in analysis of the less-well understood dielectrics considered in Chapter 6.

Finally, chemical composition can have a strong effect on the dielectric properties of an oxide. In Chapter 6, we explore dielectric properties across composition space. To do so efficiently, we prepare samples by co-sputtering from several off-axis elemental sources. Results from the tantalum-germanium oxide system are discussed in detail.

CHAPTER 2

MATERIAL PREPARATION AND ANALYSIS

This chapter discusses the experimental methods used to prepare and evaluate the dielectric oxides. Thin films are deposited by sputtering and evaporation. Metal-insulator-metal (MIM) capacitors are prepared for measuring the dielectric constant and electron leakage current. For structural characterization, some films are deposited directly on silicon or another substrate.

2.1 Polarizability, dielectric constant, and capacitance

Dielectric materials are used in a variety of device structures and for various purposes. They are employed to store charge (information), to separate voltage, or to gate charge carriers into semiconductor channels. For many of these applications, the critical parameter is the charge density supported on the electrodes; charge density (Q/A) is the product of the capacitance of the structure C and the voltage applied V, as

$$\frac{Q}{A} = \frac{CV}{A} \tag{2.1}$$

in which A is the area of the electrode. We consider first the capacitance.

The capacitance of a given device structure is the proportionality constant between the charge on the electrodes and the voltage across them:

$$C = \frac{Q}{V}. \tag{2.2}$$

The capacitance of a given structure depends both on the geometry of the device and on the dielectric material chosen. For a parallel plate capacitor, the

capacitance is given by

$$C = \frac{\varepsilon_o \varepsilon_r A}{d} \tag{2.3}$$

in which ε_r (alternatively denoted as k or κ) is the relative dielectric constant of the oxide, ε_o is the permittivity of free space, A is the area of the electrodes, and d is the distance between the electrodes. For air or vacuum, ε_r is 1, and so ε_r can be considered the factor by which the dielectric is more polarizable than air.

We note that polarizability is not always desirable in an electrical insulator. In the study of low κ dielectrics, for example, we require insulating materials that do not polarize to prevent "cross-talk," or passage of electronic information between closely spaced metal interconnects [3]. These materials have a $\varepsilon_r = \kappa \approx 1$ but are preferable to air both because of their higher breakdown field and their mechanical strength.

We may think of the polarization of a dielectric material in an electric field as a series of induced dipoles between oppositely charged electrodes (see, for example, Ref. [44, 45, 46]), as shown in Figure 2.1. The (induced) polarization charge density σ_{pol} is not as large as the charge density on the electrodes, which we will call the free charge, σ_{free}. The density of induced positive charges equals exactly the density of induced negative charges, however, such that we may consider only the charge density at the interface with the electrodes. The positively charged σ_{pol} at the top electrode plate and the negatively charged σ_{pol} at the bottom electrode give rise to a polarization vector, $\mathbf{P}$, that is antiparallel to the electric field $\mathbf{E}$ due to the oppositely charged electrode densities, σ_{free}. The presence of a dielectric material between the electrodes results in a decrease from the field across the equivalently charged electrodes in vacuum or air and thereby, an increase in the capacitance.

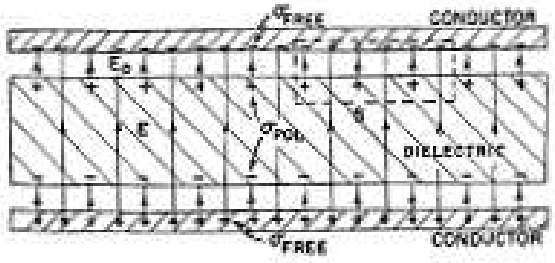

Figure 2.1: Induced dipoles in a dielectric material between oppositely charged electrodes. From Reference [44].

The magnitude of the electric field in the absence of a dielectric material is solely due to σ_{free} according to

$$E_{\text{free}} = \frac{V}{d} = \frac{Q}{C_o d} = \frac{\sigma_{\text{free}}}{\varepsilon_o} \tag{2.4}$$

in which ε_o is the permittivity of free space, as given above. Quantifying the increase in capacitance requires knowledge of the polarization vector, **P** [44]. For many materials, within a range of field strengths, the polarization is found to be linearly proportional to the applied electric field, with a proportionality constant χ, according to

$$\mathbf{P} = \chi \varepsilon_o \mathbf{E}. \tag{2.5}$$

The electric field including the polarization field is

$$E = \frac{\sigma_{\text{free}} - \sigma_{\text{pol}}}{\varepsilon_o} = \frac{\sigma_{\text{free}} - P}{\varepsilon_o} \tag{2.6}$$

$$E = \frac{\sigma_{\text{free}}}{\varepsilon_o} \frac{1}{1+\chi}. \tag{2.7}$$

With the presence of a dielectric, the field is thus reduced by a factor of $\frac{1}{1+\chi}$, while the charge density on the electrodes remains σ_{free}. The capacitance is then

$$C = \frac{Q}{V} = \frac{\sigma_{\text{free}} A}{Ed} = \frac{\varepsilon_o (1+\chi) A}{d} \tag{2.8}$$

which is just Equation 2.3 with the definition of $\varepsilon_r = 1 + \chi$.

Another formalism, useful for understanding dielectric response and relaxation in a AC field, is presented by several authors [47, 48, 49]. The current density $\mathbf{J}$ experienced by a material in response to an electric field $\mathbf{E}$ is the sum of a conduction current $\varsigma\mathbf{E}$ and a displacement current $\frac{\partial \mathbf{D}}{\partial t}$, as in

$$\mathbf{J} = \varsigma\mathbf{E} + \frac{\partial \mathbf{D}}{\partial t}. \tag{2.9}$$

(In this case, we use ς for conductivity to differentiate it from σ for areal charge density in the previous discussion.) The displacement $\mathbf{D}$ is defined as

$$\mathbf{D} = \varepsilon_o\mathbf{E} + \mathbf{P} = \varepsilon\mathbf{E} \tag{2.10}$$

in which $\varepsilon = \varepsilon_o\varepsilon_r$. The displacement current is not a real current passing through the material, but rather represents the motion of charge carriers in an AC field to satisfy the capacitance of the material. In an AC field of frequency ω, then, the dielectric response of the material is represented by the displacement current, while any DC conduction at these frequencies is contained in the first term:

$$\mathbf{J} = \varsigma_{\mathrm{dc}}\mathbf{E} + \varepsilon\frac{\partial E_o \exp(\jmath\omega t)}{\partial t} = \varsigma_{\mathrm{dc}}\mathbf{E} + \jmath\omega\varepsilon\mathbf{E} \tag{2.11}$$

in which ς_{dc} is the DC conductivity and ε is the dielectric constant of the material structure. The dielectric constant additionally has real and imaginary components, ε' and ε'', respectively, such that

$$\mathbf{J} = \varsigma_{\mathrm{dc}}\mathbf{E} + \jmath\omega\varepsilon_o(\varepsilon' + \jmath\varepsilon'')\mathbf{E}. \tag{2.12}$$

The general relationship between current density and an applied electric field may be given then as

$$\mathbf{J} = (\varsigma_{\mathrm{dc}} + \omega\varepsilon_o\varepsilon'')\mathbf{E} + \jmath\omega\varepsilon_o\varepsilon'\mathbf{E} = \varsigma\mathbf{E} + \jmath\omega\varepsilon_o\varepsilon'\mathbf{E}. \tag{2.13}$$

The components of the conductivity ς_{dc} and $\omega\varepsilon_o\varepsilon''$ may be considered as a leakage current and a dielectric relaxation, respectively. For high quality dielectric materials, in their frequency range of the operation, both components of the conductivity are negligible, and the response is dominated by the real part of the dielectric constant. In agreement with this analysis, in an ideal capacitor with no loss and no DC conductivity, the current density leads an AC electric field by 90°. This formalism of the dielectric response will be useful in understanding data collection of capacitance and loss factors in Section 2.2.3.

2.1.1 Microstructural origin of dielectric constant

We have discussed the effect of a material's polarization on the capacitance of a device by imagining a polarization due to many induced dipoles. These induced dipoles have their origin in polarization mechanisms on atomic and molecular length scales, and thus the macroscopically measured polarization is intimately related to the bonding structure of the material[1].

The polarization vector $\mathbf{P}(\mathbf{r})$ of the material that we previously discussed in terms of the induced areal charge density σ_{pol} is the volume density of individual dipoles $\mathbf{p}$, according to

$$\mathbf{P}(\mathbf{r}) = \frac{1}{V}\mathbf{p}(\mathbf{r}) \tag{2.14}$$

in which V is the volume. The polarization $\mathbf{p}(\mathbf{r})$, however, can only be properly defined in relation to the electric field it experiences; the field is not the macroscopic applied field $\mathbf{E}(\mathbf{r})$ but rather is diminished by the field of the polarization

[1]The following discussion is similar to that found in Reference [46].

itself. We define a local electric field then as

$$\mathbf{E}^{\text{local}}(\mathbf{r}) = \mathbf{E}(\mathbf{r}) + \frac{\mathbf{P}(\mathbf{r})}{3\varepsilon_o} \tag{2.15}$$

and eliminate $\mathbf{P}(\mathbf{r})$ using the definition of displacement in Equation 2.10:

$$\mathbf{E}^{\text{local}}(\mathbf{r}) = \frac{(\varepsilon_r + 2)\mathbf{E}(\mathbf{r})}{3}. \tag{2.16}$$

It is this local electric field that the individual dipole at position $\mathbf{r}$ experiences as it polarizes:

$$\mathbf{p}(\mathbf{r}) = \alpha\varepsilon_o\mathbf{E}^{\text{local}}(\mathbf{r}) \tag{2.17}$$

in which α is the microscopic polarizability. The macroscopic polarization density $\mathbf{P}(\mathbf{r})$ may then be related to the macroscopically applied electric field $\mathbf{E}(\mathbf{r})$ by

$$\mathbf{P}(\mathbf{r}) = \frac{\alpha}{V}\varepsilon_o\mathbf{E}^{\text{local}}(\mathbf{r}) = \frac{\alpha}{V}\varepsilon_o\frac{(\varepsilon_r + 2)\mathbf{E}(\mathbf{r})}{3}. \tag{2.18}$$

Again using the definition of displacement in Equation 2.10, we may eliminate $\mathbf{P}(\mathbf{r})$ to give a relationship between the relative dielectric constant ε_r and the density of polarizing units α/V:

$$\frac{\varepsilon_r(\omega) - 1}{\varepsilon_r(\omega) + 2} = \sum \frac{\alpha(\omega)}{3V} \tag{2.19}$$

in which ω is the measurement frequency and V is the molecular volume. This equation, which relates a macroscopically observed dielectric constant to the polarizability α and density V^{-1} of molecular units, is called the Clausius Mossotti equation.

Our next goal, then, is to understand the molecular scale polarization mechanisms α that give rise to dipoles $\mathbf{p}(\mathbf{r})$. In any material, there may be several polarization mechanisms active; to the extent that each is independent of the oth-

ers, the polarizabilities α are additive. Commonly observed polarization mechanisms at increasing length scales include electronic, ionic, and dispolar polarizabilities. Electronic polarizability is the displacement of negatively charged electrons relative to the positively charged nuclei in response to an applied electric field. The relative displacement of oppositely charged ions is termed ionic polarizability; an example is the the flexing of the TiO_6^{2-} structure, in which the Ti^{4+} ion is displaced with respect to the surrounding oxygen octahedron. Finally, dipolar polarizability is the re-orientation of permanent dipoles in an electric field.

By Clausius Mossotti (Equation 2.19), the dielectric constant depends on the polarizability density (α per volume), and thus we consider both the polarizability and the density of each of these polarizing components–electrons, ionic bonds, and dipoles. A simple exercise to demonstrate the relative importance of density is to consider the two crystalline forms of TiO_2: anatase and rutile. Figure 2.2 gives a schematic of the crystal structure of each. Both structures have titanium ions octahedrally coordinated by oxygen ions, but the octahedra in rutile share two edges, while those in anatase share four edges [50]. The octahedra in both structures are distorted, with two elongated Ti-O bonds; the elongation is longer in rutile than anatase [51].

Despite the similarity of their basic building blocks, however, rutile and anatase differ dramatically in their dielectric constants, with $\varepsilon_r \sim 60$ to 110 for rutile and $\varepsilon_r \sim 30$ for anatase. This difference could be due to the difference in inter-octahedra bonding or to the associated difference in density, 4.2 g cm^{-3} for rutile and 3.84 g cm^{-3} for anatase.

We may test whether the difference in density is sufficient to account for the

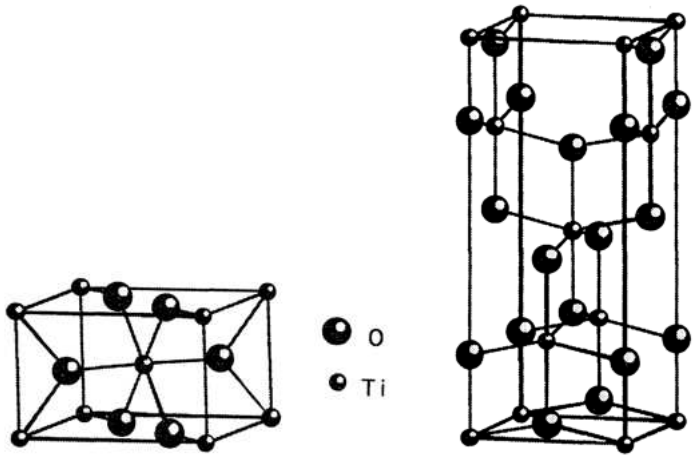

(a) Rutile (b) Anatase

Figure 2.2: Schematic drawings of the crystal structure of TiO_2. Large atoms are oxygen; small are titanium. From Reference [50].

difference in dielectric constant. Taking the ratio of polarizability densities from the known dielectric constants, we have

$$\frac{\alpha_{\text{ru}}/V_{\text{ru}}}{\alpha_{\text{an}}/V_{\text{an}}} = \frac{(\varepsilon_{\text{ru}} - 1)(\varepsilon_{\text{an}} + 2)}{(\varepsilon_{\text{ru}} + 2)(\varepsilon_{\text{an}} - 1)} = \frac{109}{112} \cdot \frac{32}{29} = 1.074 \tag{2.20}$$

in which the subscript ru refers to rutile, while the subscript an refers to anatase [52]. This analysis indicates that rutile must have a 7.4% higher polarizability density (α/V) than anatase to explain the higher dielectric constant measured. The ratio of densities, however, reveals that rutile has a 9% higher density, and thus rutile's higher dielectric constant is due to a higher density, not a higher polarizability, α. In fact, by this analysis, anatase has the higher polarizability α. We will revisit this technique to consider two different amorphous phases in Chapter 3.

In Figure 2.3, we plot the dielectric constant as a function of polarizability density, according to the Clausius-Mossotti equation. The relationship is quite non-linear, and we find that higher dielectric constants are increasingly sensitive

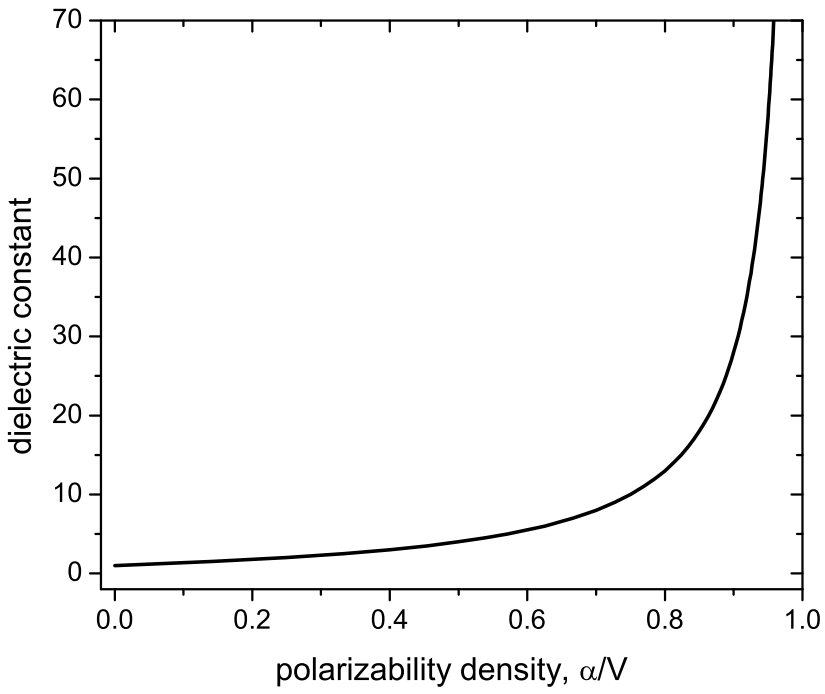

Figure 2.3: Dependence of the dielectric constant on the polarizability per volume, according to the Clausius Mossotti equation.

to the material density (inverse volume).

2.1.2 Dispersion, polarizability, and film quality

Polarization mechanisms are frequency dependent. Ions and dipoles have sufficient mass (inertia) that their motion may be damped out at accessible measurement frequencies. Dipolar polarizability is damped out at frequencies above 10^9 Hz and is not often observed in dielectric oxides. Ionic polarizability often dies off at 10^{12} Hz, as the ions can no longer respond to the changing

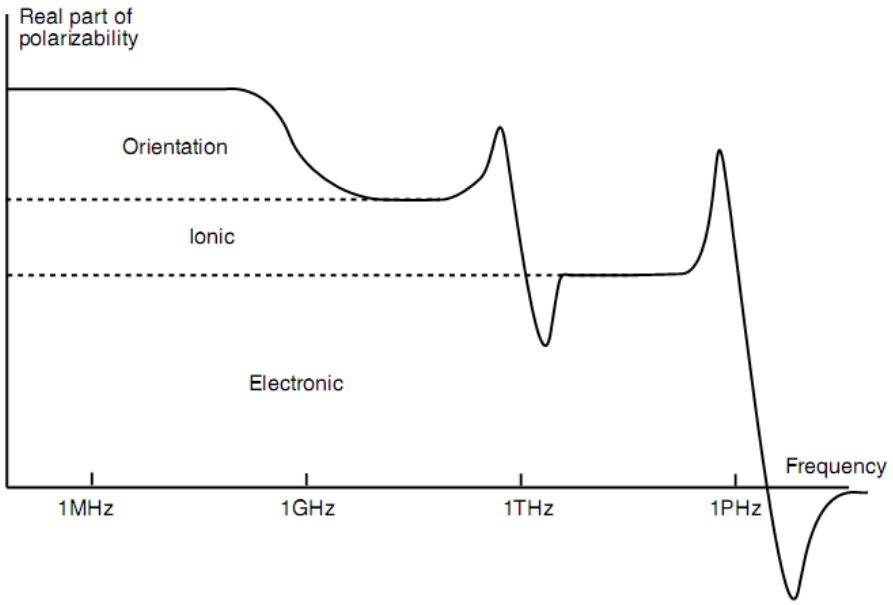

Figure 2.4: The dispersion of the polarizability α. From Reference [53].

electric field, while electronic polarizability is active to greater than 10^{15} Hz. Figure 2.4 is a schematic plot of the polarizability of a material at increasing frequency. As we see in the figure, multiple active polarizabilities are additive: $\alpha_{\text{orientational}} + \alpha_{\text{ionic}} + \alpha_{\text{electronic}} = \alpha_{\text{total}}$.

The Clausius Mossotti equation, therefore, is the relationship between the dielectric constant $\varepsilon(\omega)$ at a frequency ω due to the sum of the polarization mechanisms active at that frequency $\alpha(\omega)$.

The frequencies of interest in electronic devices are 10^3 to 10^{10} Hz. At these frequencies, we may expect that both electronic and ionic polarizabilities are active and contribute to the dielectric constant. For most amorphous unary metal oxides, the electronic and ionic polarizabilities lead to a dielectric constant of 10 to 30, which is frequency independent up to 10s GHz [6, 54]. Titania, TiO_2, is a rare example of a unary metal oxide with a dielectric constant of 60-110. Its high

dielectric constant is due to soft phonon modes (coupled vibrational modes) [4]. R. D. Shannon [54] has tabulated the ionic polarizabilities of many metal cations in their most common oxide and fluoride structures; deviations from his tables are thought to indicate non-standard bonding structures.

At optical frequencies, ~100 THz, only electronic polarizability is active, and the Clausius-Mossotti equation reduces to the Lorentz-Lorenz equation, in which the dielectric constant reduces to the square of the refractive index ~ n^2:

$$\frac{n^2 - 1}{n^2 + 2} = \frac{\alpha_{\text{electronic}}}{3V}. \tag{2.21}$$

The Lorentz-Lorenz equation provides an interesting handle on the relative importance of ionic polarizability on the dielectric constant. For covalently bonded materials such as diamond or silicon, the optical and low frequency dielectric constants are equivalent, since there is little to no ionic contribution [55]. Silicon dioxide is the best characterized thin film dielectric material; it has an index of refraction of 1.45 for an optical dielectric constant, n^2, of 2.10. Its dielectric constant at the lower frequencies of electronics is a modest improvement at 3.9, indicating a limited contribution from the ionic polarizability. Since most oxides have an $n < 2.5$, the maximum possible dielectric constant based solely on electronic polarizability is 6.25. Higher dielectric constants are possible only in oxides that are subject to an additional ionic polarizability; many of these oxides are based on the more ionic and polarizable bonds of oxides of late group II elements and early transition metals (see Table 1.1).

The physical mechanisms underlying electronic and ionic polarizabilities are frequency independent throughout the operation frequency range of modern electronics. Dispersion over the range of 100 Hz to 1 MHz indicates a low frequency polarization mode, which is neither due to electronic nor ionic polariz-

ability. Examples may include filling and emptying of traps, ionic conduction, and dangling bonds [48]. For high quality dielectric oxides, it is desirable to avoid these polarization mechanisms, both because they are unlikely to be reproducible (hard to realize in a different process) and because they may stress the material, leading to an early breakdown. Their properties are also more likely to vary significantly with frequency and temperature, within the desired operating range of the device. We will discuss several mechanisms for low frequency dispersion in Chapters 4 and 5.

2.2 Preparation and electrical analysis of MIM capacitors

We primarily choose to measure our capacitors in a parallel plate Metal-Insulator-Metal (MIM) structure. This is the simplest capacitor structure, is easy to prepare with our equipment, and can be evaluated in a straightforward manner for capacitance and leakage current.

The structure is deposited as outlined in Figure 2.5. We deposit a blanket base electrode on a silicon wafer by electron beam evaporation of a chromium sticking layer (~200-500), followed by evaporation of the platinum base electrode at ~300 . The sample is removed from the evaporation chamber. Often it is cleaved into smaller pieces before it (the whole or a piece) is placed in the oxide sputter chamber. Typically, the oxide is sputtered from a metal target in an argon and O_2 ambient. The top platinum electrodes are also evaporated, this time through a shadow mask. They are 200 micron diameter circles on a square array of 500 micron centers; they are ~200-300 thick. The area of the top electrode defines the area of the capacitor. The top patterned platinum electrodes

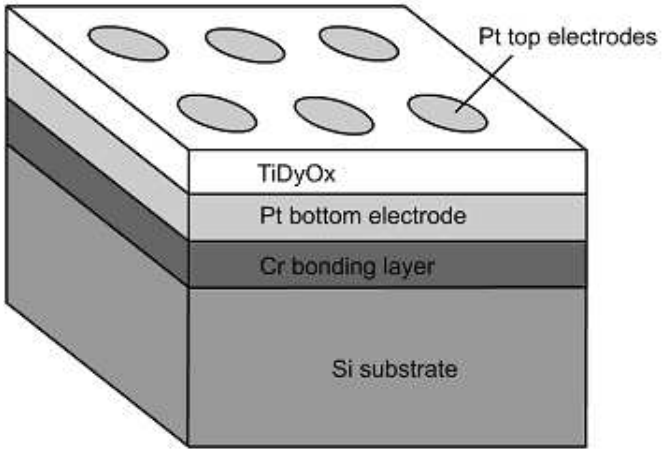

Figure 2.5: Schematic of metal-insulator-metal capacitor structures. Courtesy John Hevey [56].

and the base blanket electrode form parallel electrical contacts across the oxide.

The following sections discuss film deposition and MIM electrical measurements in greater detail.

2.2.1 Sputtering an oxide

The oxide dielectrics described in this thesis are primarily deposited by reactive radio frequency (RF) sputtering in an argon and oxygen sputtering gas. Reactive sputtering allows the use of a metal target to deposit an oxide thin film; oxidation of the metal occurs both at the target, in the gas, and at the substrate on deposition. Since the surface of the target is oxidized during sputtering, an RF power supply is used to apply power to the target [33]. For a DC power supply in an oxygen-containing sputtering gas, the growing surface oxide on the target decreases the sputtering rate with time; in contrast, the sputtering rate

remains constant from an RF power source since it allows target bombardment by electrons during the positive portion of the voltage cycle.

Sputtering is the result of argon ion bombardment of the target during the negative portion of the voltage cycle. Largely a billiard-ball effect, relying on momentum transfer from the Ar^+ ions, sputtering can eject target atoms and dimers with kinetic energy of 10s-100 eV. The sputtered species are subject to inelastic scattering events in the sputtering gas, however, and thus lose energy. At higher sputtering gas pressures, the mean free path in the gas is low, depositing species have lower average energy, and the deposition profile is more disperse. In Chapter 6, we exploit these effects in designing a multi-sourced, oblique deposition technique for our composition spreads.

A number of sputtering parameters can be controlled in reactive sputter depositions. Power to the sputtering target most significantly influences deposition rate, though geometry (substrate to target distance, on-axis versus off-axis) and sputtering gas pressures can additionally affect the deposition rate. Many of the samples in this thesis were deposited on resistively-heated substrates, a technique which increases the surface mobility of depositing species. Surface mobility on oblique substrates may be enhanced by ion bombardment.

Implications of the sputtering plasma with respect to on- and off-axis depositions are discussed in Chapters 4.2 and 5, respectively.

2.2.2 Electrodes

The metal electrodes are deposited by electron beam evaporation. Sources of the target materials are placed in a water-cooled crucible in the evaporation chamber. The crucible can be rotated to expose different targets without breaking vacuum, allowing the deposition of layers of different materials in a single pumpdown. The chamber is evacuated by a roughing-backed diffusion pump down to ~2x10^{-6} Torr. The high voltage power supply applies a voltage across a tungsten filament; at high currents, the filament heats up and emits electrons, which are guided electromagnetically towards the target source. At high electron beam impingement, atoms are evaporated from the source and are deposited on the substrate and the walls of the chamber.

For the study presented here, the top electrodes are platinum, evaporated through a shadow mask. Many of the base electrodes are evaporated platinum on an *in situ* evaporated chromium sticking layer. The evaporation rate of chromium is 3-7 /s, while that of platinum is 1-2 /s. For other samples, the platinum is evaporated on an *ex situ* sputtered tantalum layer. Other metal electrodes (nickel, silver, gold) have also been deposited on by sputtering on silicon wafers or by evaporation on chromium sticking layers on silicon. There was also a supply of titanium nitride coated wafers left over from Bell Labs.

A primary concern in choosing base electrodes is a possible chemical interaction with the depositing film. Many of the results are from capacitors with platinum electrodes for exactly this reason; platinum is a noble metal and does not oxidize or react easily. In contrast, titanium nitride and nickel may oxidize in an atmosphere with energetic oxygen. Another concern is the roughness of the base electrode. The base electrode acts as the substrate for the sputtered

oxide film, and a rough surface can induce a nonideal microstructure in the depositing film or lead to a poor quality interface with the depositing film. Either may mask the intrinsic properties of the dielectric oxide. The effect of base electrodes on dielectric measurements is discussed in Section 4.3.4 for the specific case of $(Ti,Dy)_xO_y$ films.

2.2.3 Measuring capacitance and current-voltage

The deposition described in the previous sections gives a square array of parallel plate MIM capacitors and is pictured in Figure 2.5 in the introduction to Section 2.2. As can be seen in the figure, this capacitor is a two point device; to measure it, we make electrical contact to the metal base electrode and to the platinum top electrode. The top electrode is probed with a one mil diameter BeCu probe tip, while a gold wire is soldared with indium to the base electrode.

The square array of top electrodes allows the measurement of a square array of capacitors and therefore a map of the dielectric properties across the sample. The ~2500 capacitors per square inch provide plenty for statistical averaging of properties. Additionally, the area chosen for the top electrode (3.14×10^{-4} cm^2) is such that it is large enough to probe easily but not so large that capacitors are short-circuited by pinholes in the film. Pinholes are defects in deposited films that extend (most of) the thickness of the film, leading to a conducting path through the dielectric. They are found at some density across the film's surface, such that very large area capacitors have a statistically high probability of being short-circuited by one, while very small area capacitors have very low probability of being shorted. Thus, we must take care when interpreting the

percentage of 'bad' capacitors in any sample; for the same quality oxide film, the percentage depends greatly on the electrode size.

A semiautomatic probe station and a LabView-controlled measurement record enable high-throughput data collection. Coaxial cables connect the electronic meters to the BeCu probe tip and the gold wire on the base electrode.

Both capacitance and leakage current measurements are taken. For the capacitance measurements, the electronic meter is an Hewlett Packard 4284A LCR (Inductance-Capacitance-Resistance) meter [57]. Measuring the leakage current requires a Keithley 617 electrometer (a dc voltage source and current meter). Measurements are taken in series for each sample: first the sample is mapped for capacitance measurements on the LCR meter, then the coaxial cables are moved to the electrometer, and leakage current measurements are taken for the sample.

Capacitance measurements are an ac (alternating current) measurement. In general, an ac voltage of 10 mV to 1 V is applied to the capacitor; no dc bias is applied for MIM capacitors. The ac current is measured at the LCR meter and is converted to capacitance and dissipation data. The ac current can be thought of as a current magnitude and a phase lag from the ac voltage:

$$V = Re(V_o e^{(j\omega t)}) \tag{2.22}$$

$$I = Re(I_o e^{(j\omega t - j\phi)}) \tag{2.23}$$

The complex impedance, therefore, is the ratio of the complex voltage to the complex current and has real and imaginary parts resistance (R) and reactance (X), respectively:

$$\mathbf{Z} = \frac{\mathbf{V}}{\mathbf{I}} = R + jX \tag{2.24}$$

in which $\jmath$ is the imaginary number $\jmath = \sqrt{-1}$. It is convenient in this case to refer to the admittance $\mathbf{Y}$, which is the inverse of the impedance and has real and imaginary parts conductance (G) and susceptance (B), respectively, such that:

$$\mathbf{Y} = \frac{1}{\mathbf{Z}} = G + \jmath B. \tag{2.25}$$

Now we may define the capacitance C by its relationship to the susceptance: $B = \omega C$, in which ω is the frequency. Intuitively, we may think that the capacitance is proportional to B, the imaginary part of the admittance because it is the imaginary component of the admittance that gives the phase difference between the ac current and ac voltage.

To gather complete information about the admittance of our sample, we must also record information regarding the conductance, G. We do so by recording the dissipation factor $\tan\delta$: $G = |B|\tan\delta = |\omega C|\tan\delta$. Thus, the hardware of the LCR meter records $\mathbf{V}$ and $\mathbf{I}$, while the software of the LCR meter calculates C and $\tan\delta$ from the data by the formula

$$\mathbf{Y} = \frac{\mathbf{I}}{\mathbf{V}} = |\omega C|\tan\delta + \jmath\omega C \tag{2.26}$$

To give further intuition into Equation 2.26, we note that the dissipation factor appears in G, the real part of the admittance. The real part of the admittance is the part that represents an ohmic component of the current-voltage relationship and therefore the extent to which current and voltage are in phase. In the case of an ideal capacitor, dissipation is zero; in the real capacitors in this thesis, dissipation has a small positive value ~ 0.008 to 0.05, in general.

Dissipation is also known as the loss tangent, emphasizing its association

with the phase lag between current and voltage.

$$\tan\delta = \cot\phi = \frac{|B|}{G} \tag{2.27}$$

in which $\phi = \pi/2 - \delta$ is the phase difference between current and voltage, or equivalently, δ is the phase difference between the ac current and the ac current to an ideal capacitor. To compare these definitions to the materials' constants we hope to evaluate, the dissipation can also give the ratio between the imaginary part and the real part of the dielectric constant:

$$\tan\delta = \frac{\varepsilon''}{\varepsilon'} \tag{2.28}$$

in which ε'' is the imaginary part of the dielectric constant and ε' is the real part of the dielectric constant.

From the capacitance and dissipation data, therefore, we may calculate the real and imaginary parts of the dielectric constant, ε' and ε'', using the equations given above. For high quality dielectric materials, the imaginary part ε'' is commonly neglected since it is a small fraction of the real part. However, we will find it useful in Chapters 4 and 5, when we consider very lossy capacitors, measured close to their relaxation frequencies.

The measurements of capacitance and dissipation are ac measurements, and, as discussed in Section 2.1.2, the frequency dependence of these quantities can be quite important for elucidating the polarization mechanism active in a sample. To evaluate the frequency dependence, some samples were measured at several frequencies, either by a single probing per capacitor or by probing each capacitor several times.

In contrast, the leakage current is a dc measurement. The electrical contacts between the capacitor and the electrometer are pictured in Figure 2.6. The dc

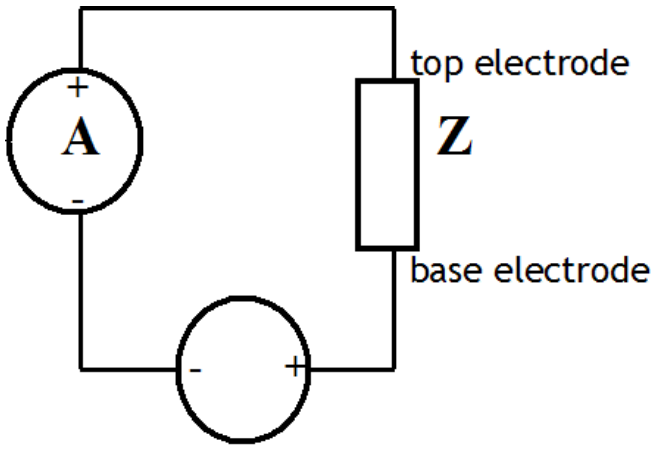

Figure 2.6: Electrical contacts to the Keithley 617 electrometer during I-V measurements.

voltage across the capacitor is ramped in 0.1 to 0.25 V steps. At each step, current is recorded after a 1 s pause. The voltage is ramped until the current density reaches 3 mA cm^{-2}, or 10^{-6} Amps for the 200 micrometer diameter electrode; the voltage at this current is recorded and referred to as the breakdown voltage, V_{br}. The electric field at breakdown is simply the breakdown voltage, normalized to the thickness of the oxide film. The current at $0.75 \times V_{\mathrm{br}}$ is also recorded in the data files to give a crude indication of the shape of the current-voltage curve. For a more detailed analysis, the current-voltage curve is saved for each capacitor, as well.

It is important to note that the current at "breakdown" is somewhat arbitrarily chosen. For a given engineering application, the breakdown condition is defined by an unacceptable current density. Dielectric gate materials in transistors, for example, require only that sufficient charge density be gated into the channel region. In current integrated circuit technology for high power computation applications, 100 A cm^{-2} are tolerated as tunneling current densities

across the ~1-3 nm of SiO_2; even for low power applications such as laptops and cell phones, the leakage current can be 10 mA cm^{-2} (Reference [6]). In contrast, for memory applications, the leakage currents must be much lower. FLASH memory, for example, requires that charge tunnel into a metal particle (gate) and not leak away over the next 10 years; the specification given [6] is on the order of 10^{-7} to 10^{-8} A cm^{-2}. In the present case, we find that defining breakdown at 3 mA cm^{-2} resolves the "hard breakdown" of many capacitors, but limits the current to safe laboratory levels.

Finally, it is important to consider the source of this electronic leakage current. An ideal dielectric experiences no leakage current until the dielectric breakdown of the material. The dielectric breakdown, or "hard" breakdown, is generally an ionization of the material itself. For air, this takes place at an electric field of ~100 kV cm^{-1} and is seen as an electric arc across the electrodes. For solid dielectric materials, the "hard" breakdown may be due to an avalanche, or cascading, current, in which high energy electrons cause the ionization of atoms, thus multiplying the number of available electrons.

Leakage currents in real materials have a variety of mechanisms before reaching a hard breakdown condition (see, for example, Ref. [58, 59]). In many cases, electric currents are defect-mediated [60]. Frenkel-Poole-limited conduction refers to conduction controlled by the thermionic emission of electrons in mid-gap traps into the conduction band. It is characterized by a current (J)-voltage (V) relationship, given by

$$\log(J/V) \sim V^{1/2} \tag{2.29}$$

Schottky-limited conduction, in contrast, refers to conduction limited by thermionic emission of electrons over the insulator-metal Schottky barrier into

the insulator's conduction band. Its J-V is very similar:

$$\log(J) \sim V^{1/2} \tag{2.30}$$

The similarity of these two limiting equations makes differentiation of the mechanisms difficult from J-V curves at a single temperature. In Figure 2.7, we plot the J-V of a single capacitor of $Pt/Ti_{0.77}Dy_{0.23}O_{1.9}/TiN$ with an oxide 300 nm thick. The Frenkel-Poole relationship ($\log(J/V)$ versus $V^{1/2}$) and the Schottky relationship ($\log(J)$ versus $V^{1/2}$) are also plotted for the same J-V. Were either of these mechanisms the current-limiting step, the relationship would linear. Both, however, can be fit well linearly over some J-V range, particularly at the higher electric field values. It is likely that both leakage mechanisms are active in these capacitors.

2.3 Adventitious SiO_2 formation during depositions on silicon

While the majority of the dielectric materials examined in this thesis are evaluated from an MIM structure, we have made some effort to understand their properties in an metal-insulator-semiconductor (MIS) structure, as is common in the literature and in industry. As discussed in Chapter 1, MIS structures are required when gating charge into a semiconductor, most commonly silicon, to turn a transistor on or off. Unlike the MIM capacitors in which we deposited oxide on noble metal base electrodes, MIS capacitors require the deposition of an oxide on a reactive substrate, namely silicon.

For deposition parameters, sputtering on silicon is identical to sputtering on noble base electrodes. The difference occurs at the interfaces of deposited films

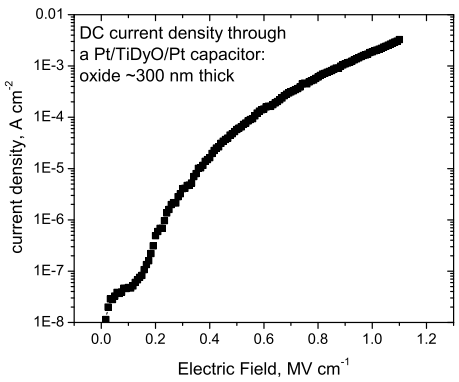

(a) J-E

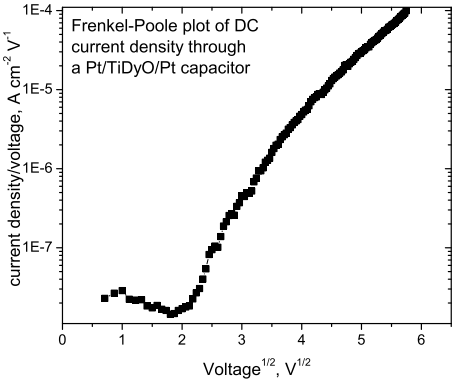

(b) Frenkel-Poole analysis

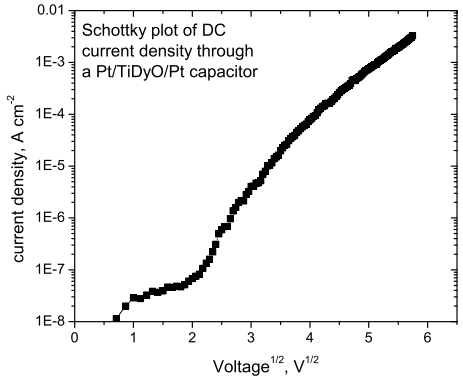

(c) Schottky analysis

Figure 2.7: JV for a Pt/300 nm $Ti_{0.77}Dy_{0.23}O_{1.9}$/TiN capacitor. Sample 05h055.

with the substrate, namely the adventitious silicon dioxide layer that occurs between the deposited oxide film and the silicon wafer. The SiO_2 layer forms a series capacitance which depresses the overall capacitance.

Because the noble metal electrodes (mainly platinum) have a limited chemical reactivity with oxygen, interfacial oxide formation between the electrode and the dielectric oxide is unlikely. Other electrode materials (nickel, TiN, e.g.)

may form more substantial oxide layers. In contrast, silicon forms silicon dioxide easily, and in fact in ambient is always covered with a native SiO_2 layer ~1 nm thick [61].

The silicon dioxide layer in reactive sputter depositions can be even thicker, as seen in the TEM micrograph in Figure 2.8. The micrograph is a cross-sectional high resolution TEM of a $Zr_{0.2}Sn_{0.2}Ti_{0.6}O_2$ film reactively sputtered on a silicon substrate heated to a temperature of 200 °C during deposition. The SiO_2 layer is found to be 4 nm thick, though a native oxide layer is expected to be only 1 nm thick.

Reactive RF sputtering introduces an active oxygen atmosphere (plasma) surrounding the wafer. In addition, the negative self-bias voltage developed on the sputter target sets up an electric field in the chamber in which negatively-charged oxygen ions are accelerated away from the sputter target. Since the substrate is, in general, parallel to and facing the target, these oxygen ions bombard the silicon substrate. At energies of 10s eV, some bury into the silicon wafer itself. Ion bombardment of substrates and the depositing film is discussed further in Chapter 5.

In applications for which a high areal capacitance (low equivalent oxide thickness, EOT) is critical, such as integrated circuit technology, the adventitious silicon dioxide can be a dealbreaker, as its thickness represents the lowest achievable EOT for the dielectric stack.

Oxide thin films deposited on silicon are also preferred for many structural characterization techniques. Crystallinity and texture of a film are evaluated by x-ray diffraction. While diffraction peaks from the single crystalline silicon

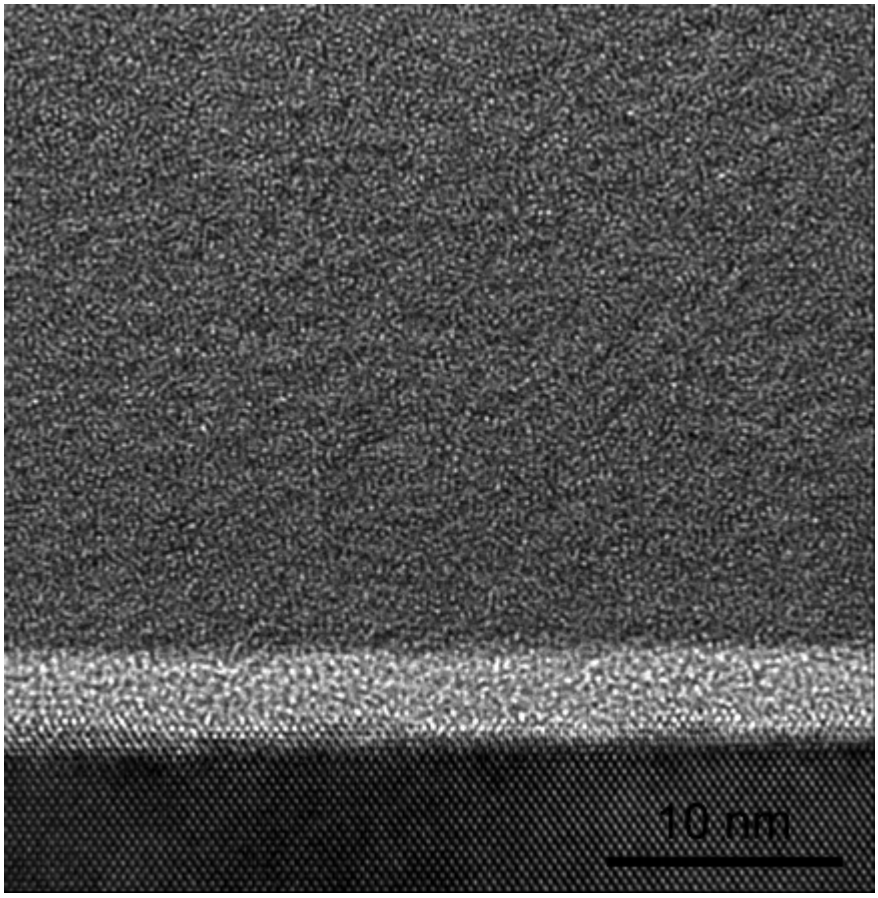

Figure 2.8: High resolution TEM micrograph of $Zr_{0.2}Sn_{0.2}Ti_{0.6}O_2$ film on a silicon wafer. The SiO_2 layer is the brighter interfacial layer. Courtesy Lena Fitting Kourkoutis, Matthew Weyland, and David A. Muller.

wafer are easily avoided by choosing the sample orientation, however, peaks from a polycrystalline base electrode can overlap diffraction peaks from the oxide, complicating identification of phases. We find, in addition, that understanding optical measurements of thickness is more straightforward for transparent oxide films on silicon than on thin metal films. While making a measurement of a film stack including metal films is largely equivalent to the single film on silicon, it is more difficult to develop the optical model to which the mea-

surements are fit, since the refractive indices of metal films may deviate from their bulk values and vary significantly over the visible range. Films deposited on silicon, in contrast, are modeled with an interfacial SiO_2 layer and a silicon substrate. While we must assume a thickness for the SiO_2 layer (~1-3 nm, in general), the refractive indices of silicon and SiO_2 are well-characterized.

CHAPTER 3

EFFECT OF DEPOSITION TEMPERATURE ON DIELECTRIC CONSTANT AND ATOMIC STRUCTURE (ZIRCONIUM, TIN-SUBSTITUTED TITANIUM DIOXIDE)

This chapter is adapted from S. C. Barron and R. B. van Dover: "Molecular volume and polarizability in the amorphous dielectric $Zr_{0.2}Sn_{0.2}Ti_{0.6}O_2$," in *Ferroelectric Thin Films XIII*, edited by R. Ramesh, J.-P. Maria, M. Alexe, V. Joshi (Mater. Res. Soc. Symp. Proc. **902E**, Warrendale, PA, 2006), 0902-T10-65. [52].

3.1 Abstract

The dielectric constant of a material is strongly dependent on both the polarizability and the density of the material through the Clausius Mossotti equation. While the atomic polarizability depends on the stoichiometry of the constituent atoms, the molecular polarizability is a function of the atoms' short range bonding structure and hence can be strongly dependent on processing conditions. Since the density of the material also depends on the thermally activated diffusivity of atoms during processing, varying the processing temperatures has an effect on both the molecular polarizability and the density. The dielectric constant of $Zr_{0.2}Sn_{0.2}Ti_{0.6}O_2$ is shown to be a strong function of the substrate temperature during sputter deposition with the highest value ε 55 at 200 °C and lower values at both higher and lower process temperatures. We have investigated the bonding structure and density of the oxide dielectric deposited at a variety of substrate temperatures in order to elucidate the relative effects of each.

3.2 Introduction

As new semiconductor systems are developed, the need for new dielectric materials becomes prevalent. The benchmark dielectric for the past thirty years has been silicon dioxide for its ease of processing in standard silicon technology. Novel semiconductor systems, such as carbon nanotubes and other organic based materials, are promising in niche applications, however, and have different processing and property requirements than the standard silicon technologies. There is an opportunity, therefore, to develop new dielectric materials whose properties can be exploited by these new semiconductors.

Regardless of the semiconductor chosen, a key parameter for the dielectric material is the maximum areal charge density, $CV_{br}/A = \varepsilon_o \varepsilon_r E_{\mathrm{br}}$, i.e. the charge that can be supported at the breakdown field (E_{br}) of the dielectric. This figure of merit (FOM) physically corresponds to the charge that can be gated into the channel region of a transistor. In 1998, van Dover et al. used a continuous composition spread technique to search for complex amorphous oxides which optimize this FOM [62]. They found that the amorphous form of $Zr_{0.15}Sn_{0.3}Ti_{0.55}O_{2-\delta}$ has a dielectric constant of 62.5 and a breakdown field of 4.4 MV/cm. The dielectric could therefore gate up to 24.3 μC/cm^2 into a semiconductor; this represents a six-fold improvement over the maximum possible performance of SiO_2 and three-fold over some of the other high performance dielectrics under investigation such as ZrO_2 and HfO_2 [6].

Van Dover et al. used a reactive rf sputter deposition technique to deposit the material using both on- and off-axis configurations [62, 63]. They found that the material deposited on a substrate heated to 200 °C gave the optimal

properties and a dielectric constant of 62.5 at 10 kHz. Lu et al. [64] prepared the neighboring composition $Zr_{0.26}Sn_{0.23}Ti_{0.51}O_{2-\delta}$ by pulsed laser deposition on silicon substrates heated to 600 °C; at this temperature, they found an amorphous material with a dielectric constant of 40 at 1 MHz. They found that their films crystallize in a post-deposition anneal during differential thermal analysis to 620 °C. Nakagawara et al. [65] also prepared films of (Zr,Sn)TiO_4 by pulsed laser deposition and found that an amorphous film with a dielectric constant of 27 at 1-2 GHz resulted for substrate temperatures up to 600 °C at O_2 pressures of less than 10 mTorr. At higher pressures, they found that the material crystallized at temperatures as low as 400 °C into a solid solution of tin oxide in the equilibrium $ZrTiO_4$ structure; this material had a dielectric constant of 38 at 1-10 GHz.

Because our thin film dielectrics are prepared by reactive rf sputter deposition, the deposition temperatures and morphologies for the PLD prepared films are not directly comparable but demonstrate a variation of structure and dielectric properties with processing temperature. The goal of this work is to elucidate the relative effects of structure and density on the dielectric constant of Zr-Sn-Ti oxides at different frequencies and to determine the ideal processing temperatures to effect the desired structure and density for optimal properties.

3.3 Experimental methods

Samples were prepared by rf sputter deposition from a 2-inch diameter alloy target with the same metal stoichiometry ($Zr_{0.2}Sn_{0.2}Ti_{0.6}$) as the cations in the desired oxide. The power to the gun was 100 W at 13.56 MHz, and the sputtering

gases were 40% O_2 in Ar at 7 mTorr. Substrates were held 2.5 cm from the target and resistively heated to the desired temperature. For electrical analysis, a base electrode of sputtered TiN or of evaporated Pt was used. For compositional, structural, or thickness analysis, the substrate was a lightly doped silicon wafer, to avoid extraneous signal from the base electrode. Samples ranged from 50 to 120 nm thick as evaluated by ellipsometry.

The dielectric constant was evaluated from capacitance data. After sputter deposition of the dielectric layer, the samples were moved to an electron beam evaporation chamber, and platinum counterelectrodes were evaporated through a shadow mask to a thickness of 20 nm. These top electrodes are 200 micrometers in diameter in a square array on 500 micrometer centers. This geometry gives an array of parallel plate capacitors from which the dielectric constant may be evaluated.

An automated probe station and an LCR meter (HP 4219) measure the capacitance. Electrical contact to the top electrode is made by a beryllium copper probe tip, while a gold wire is soldered with indium to an exposed portion of the base electrode to make the second contact. Capacitors are driven at 1 V_{ac} with no dc bias at a frequency of 10 kHz; capacitance and dissipation factor are recorded for twenty to 200 capacitors per square inch.

To characterize the high frequency dielectric response, optical refraction data is collected on a Woollam spectroscopic ellipsometer for wavelengths from 0.25 to 1.00 microns. To analyze the results, a bilayer model of a silicon substrate and a Cauchy layer were fit to the data for large wavelengths, assuming transparency at these wavelengths. The Cauchy relationship, given by

$$n = A + \frac{B}{\lambda} + \frac{C}{\lambda^2} \tag{3.1}$$

is an empirical relationship for the refractive index (n) as a function of the wavelength of light (λ) for transparent materials. To compare indices from sample to sample, we compare the fitted A values since these are high wavelength limits, far from the absorption edge.

The films were structurally characterized by x-ray diffraction using Theta-Theta scans and cross sectional TEM. The ratio of cations was confirmed by Rutherford Backscattering.

3.4 Results and discussion

Capacitance results

The dielectric constant from capacitance measurements is shown as a function of substrate temperature during deposition in Figure3.1. The shading and shape of the data points indicates the base electrode material (TiN or Pt). There is a great deal of scatter in the data as the material varies from sample to sample. Additionally thickness measurements were evaluated from a small number of samples deposited on silicon, and the dielectric constant shown is calculated from inferred deposition rates and is therefore subject to an error of 15%. It is clear, however, that the dielectric constant reaches its maximum value of ~55 at deposition temperatures between 120 and 220 °C. At temperatures below 100 °C, the dielectric constant falls off sharply to ~28. At temperatures above 250 °C, the material has less consistency from sample to sample, and indeed more than half the samples have a dielectric constant ~35.

To elucidate the effect of processing at different temperatures, we consider

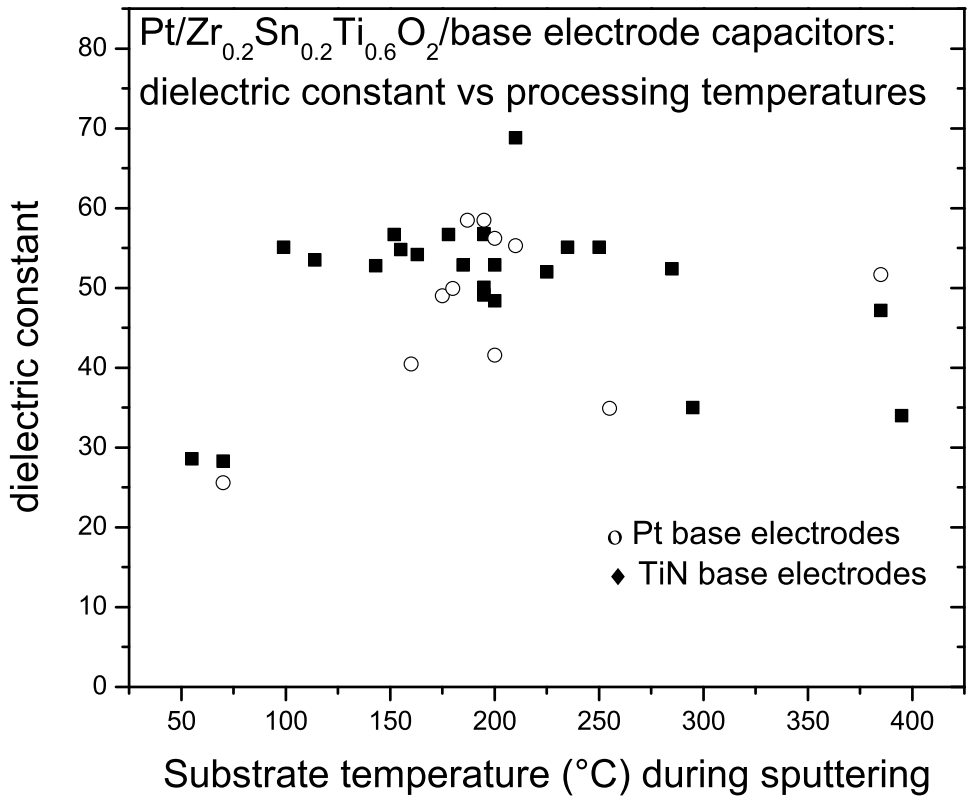

Figure 3.1: The dielectric constant as a function of substrate temperature during rf sputtering. The dielectric constant was measured at 1 V_{ac} at a frequency of 10 kHz for Pt/ZTT/base electrode capacitors. The base electrodes were either TiN or Pt.

the two factors that govern the dielectric constant: the polarizability and the molecular volume. The relationship between these factors is given by the Clausius-Mossotti equation:

$$\frac{\varepsilon - 1}{\varepsilon + 2} = \frac{\alpha}{3V} \tag{3.2}$$

where ε is the dielectric constant, V is the molecular volume, and α is the sum of active polarizabilities. (The inclusion of the factor of three assumes a spherically symmetric local electric field. In this paper, we make the assumption that local bonding environments in amorphous materials are sufficiently spherical that the error associated with the factor of three is negligible.)

Both polarizability and molecular volume are expected to vary with deposition temperature since both are related to the bonding structure. Molecular volume is additionally dependent on the void structure. Bonding structure can be evaluated by x-ray diffraction techniques, while molecular volume can be probed by ellipsometry.

Effect of structure

Structural analysis of this material reveals that samples prepared at less than 200 °C are amorphous. They have no x-ray diffraction peaks, and a cross sectional TEM sample prepared at 180 °C has only occasional crystallites (less than 20 nm in diameter) forming at 70 nm or more from the growth surface. Since most capacitors fabricated were less than 60 nm thick, these crystallites are assumed to have no effect on the dielectric constant inferred from capacitance data. A high-resolution micrograph from this TEM sample is shown in Figure 3.2.

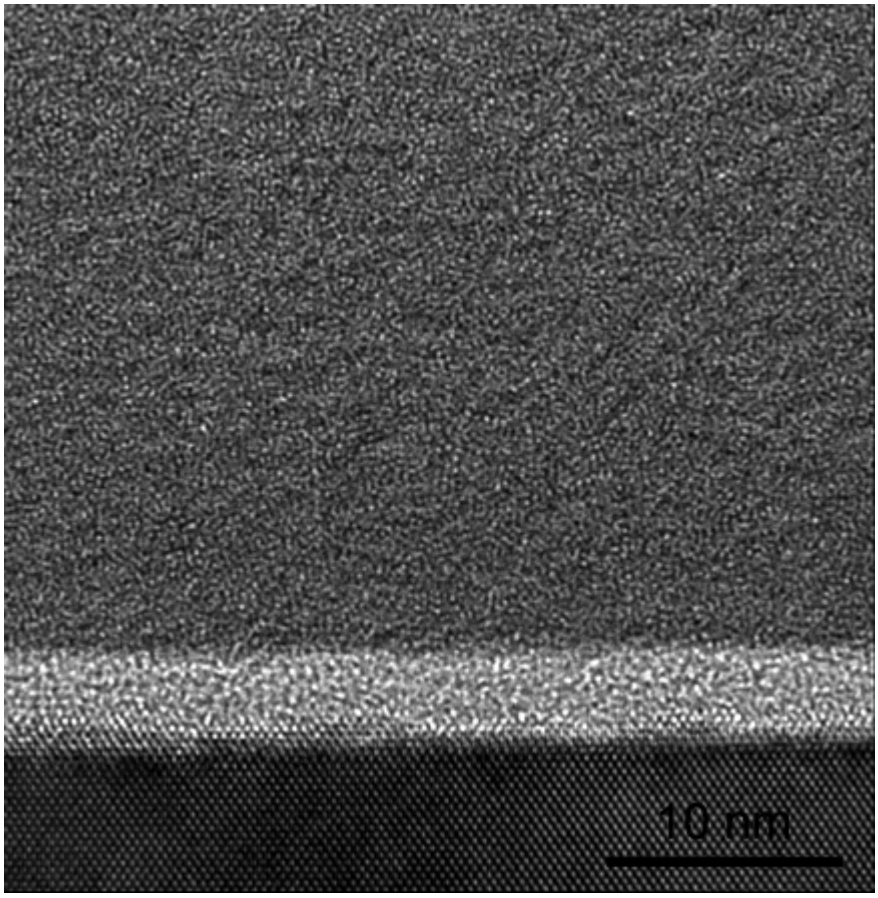

Figure 3.2: High resolution TEM micrograph of $Zr_{0.2}Sn_{0.2}Ti_{0.6}O_2$ film on a silicon wafer. The SiO_2 layer is the brighter interfacial layer. Courtesy Lena Fitting Kourkoutis, Matthew Weyland, and David A. Muller.

Cross sectional TEM (Figure 3.3) of the material deposited at 500 °C revealed some crystallization occurring within 25 nm of the substrate plane. X-ray diffraction results for material deposited at 320, 400, and 500 °C are shown in Figure 3.4. At 320 °C, the deposited material is amorphous. At higher deposition temperatures, two crystalline phases are present. At 400 °C and 510 °C, the crystalline phase is based on TiO_2 rutile (ε ~60) with partial Zr^{4+} and Sn^{4+} cation substitution. For the thicker 500 °C material, the TiO_2 anatase phase (ε ~30) pre-

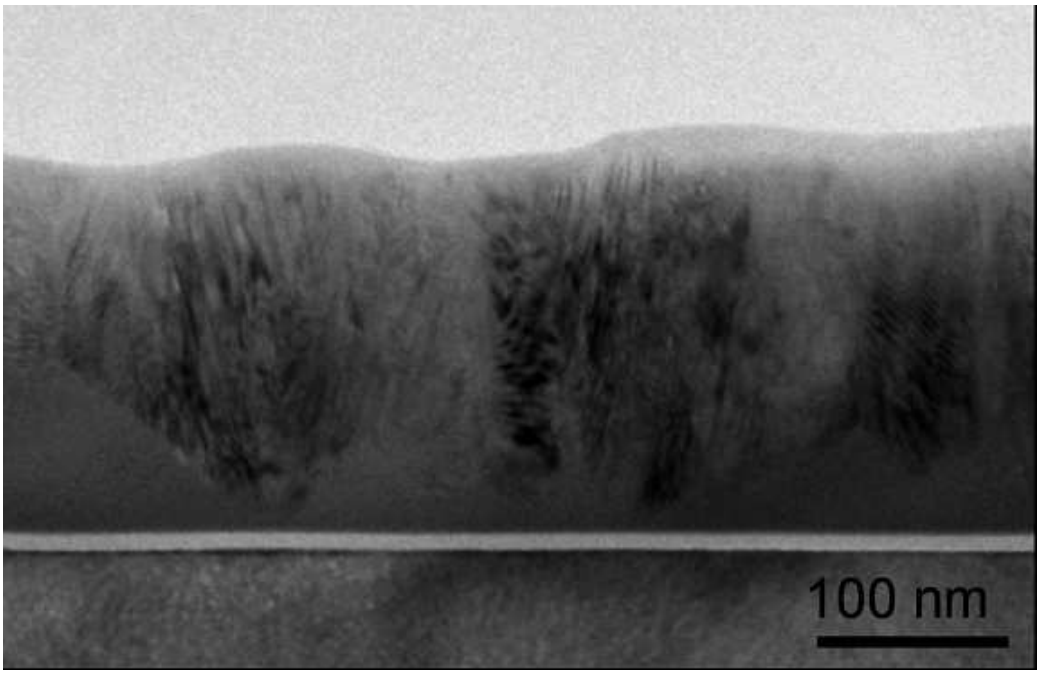

Figure 3.3: TEM micrograph of $Zr_{0.2}Sn_{0.2}Ti_{0.6}O_2$ film deposited on a silicon wafer at elevated temperature, 500 °C. The SiO_2 layer is the brighter interfacial layer. Courtesy Lena Fitting Kourkoutis, Matthew Weyland, and David A. Muller.

dominates over the rutile phase.

A competition between the nucleation of these two crystalline phases could account for the lack of consistency in measurements of the dielectric constant for samples deposited at substrate temperatures greater than 250 °C.

Effect of molecular volume

At a given frequency, the dielectric response of a material is related both to the polarizability and the molecular volume, according to the Clausius Mossotti equation (Equation 3.2). At optical frequencies (> 100 THz), the only active po-

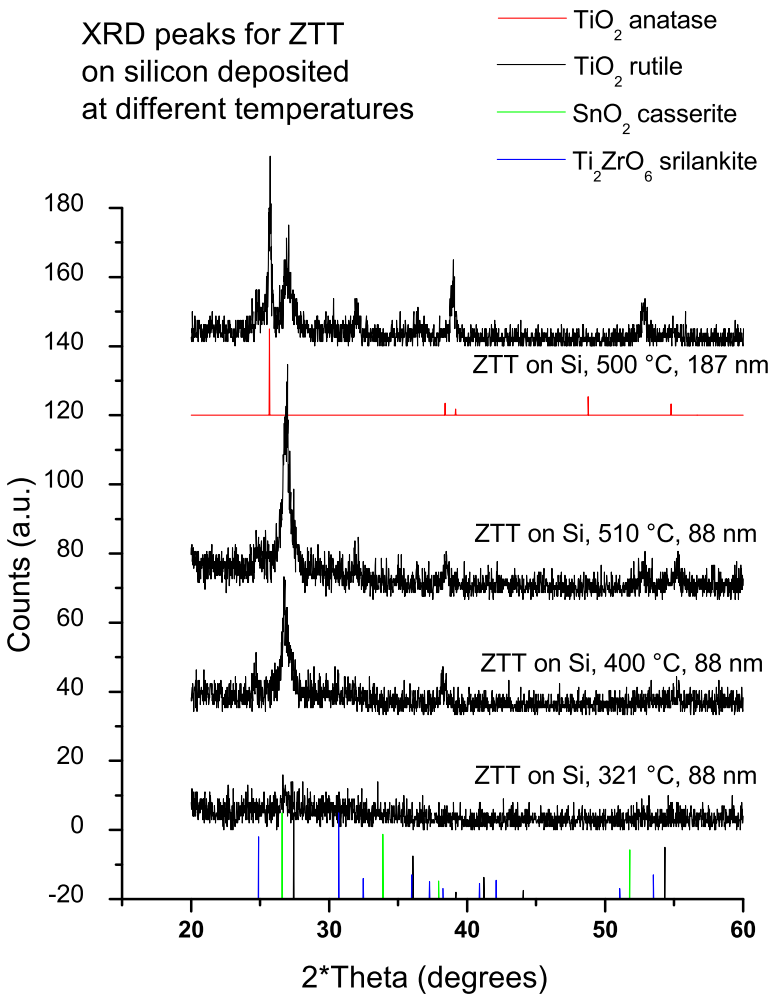

Figure 3.4: Xray diffraction results from a Scintag Theta-Theta diffractometer for films deposited on heated substrates at 320 °C, 400 °C, and 500 °C. Crystalline phases are shown to be either the TiO_2 anatase phase, or a solution of TiO_2 rutile and the related SnO_2 casserite.

larization mechanism is electronic: vibration of the electron clouds about a stationary nucleus. All other polarization mechanisms are frozen out, and the polarizability depends only on the material stoichiometry. The dielectric constant at these frequencies reduces to the square of the refractive index. The Clausius Mossotti equation is equivalent to the Lorentz Lorenz equation:

$$\frac{n^2 - 1}{n^2 + 2} = \frac{\alpha_{\text{electronic}}}{3V} \tag{3.3}$$

in which n is the refractive index, $\alpha_{\text{electronic}}$ is the polarizability of the electron clouds, and V is again the molecular volume as in Equation 3.3.

Measurements of refractive index can elucidate molecular volumes. Since films deposited at different temperatures vary only in structure, not in stoichiometry, the electronic polarizability can be assumed to be a constant. By measuring refractive index for a number of samples, we can find the relative molecular volumes through the Lorentz Lorenz relationship.

Spectroscopic ellipsometry was used to evaluate refractive indices for samples deposited at a series of substrate temperatures; these values are tabulated in Table 3.1. The second column of Table 3.1 is the molecular volume of each film calculated relative to that of the film deposited at 193 °C, according to

$$\frac{V_{193}}{V'} = \frac{(n'^2 - 1)(n_{193}^2 + 2)}{(n'^2 + 2)(n_{193}^2 - 1)} \tag{3.4}$$

in which values labeled 193 refer to material deposited at 193 °C and primed values are material deposited at other temperatures. The substrate temperature of 193 °C is chosen as a reference since the highest dielectric constant is found for material deposited between 120 and 250 °C.

To effect the observed change in dielectric constant with deposition temperature, there must be a corresponding change in α/V, according to the Clausius

Table 3.1: Refractive index measured for material deposited at a series of substrate temperatures. Relative volume and polarizability per volume have been calculated using the Clausius Mossotti equation.

Substrate temperature (°C)	Refractive index, n	Relative volume V_{193}/V'	Measured ε	Relative α/V from measured ε
48	2.1816	1.005	28	0.950
80	2.1867	1.008	28	0.950
115	2.1484	0.988	50	0.995
180	2.1773	1.003	55	1.000
193	2.1665	1.000	55	1.000
320	2.1673	0.998	50	0.995
400	2.2294	1.029	35	0.970
510	2.2020	1.016	35	0.970

Mossotti relationship (Equation 3.2). The α/V values, relative to the film deposited at 193 °C, are calculated as

$$\frac{\alpha'/V'}{\alpha_{193}/V_{193}} = \frac{(\varepsilon' - 1)(\varepsilon_{193} + 2)}{(\varepsilon' + 2)(\varepsilon_{193} - 1)} \tag{3.5}$$

in which ε is the dielectric constant inferred from capacitance measurements at 10 kHz. The dielectric constant from capacitance measurements are given in the fourth column of Table 3.1, while relative α/V values appear in the fifth column.

We may now evaluate the effect of density on the dielectric constant. From column 3, we observe that the density of the material varies by at most ~1% from the optimal material for amorphous films. As the material begins to crystallize at 400 °C and greater, the density increases by 1-3%, as expected for a crystalline

film.

The observed variation in dielectric constant, however, requires a decrease in α/V on the order of 5% for the low temperature depositions. The observed difference in molecular volume, therefore, is insufficient to explain the difference in dielectric constant between material deposited at 50 °C and the optimal material at 200 °C. We must, therefore, infer that the optimal material has an enhanced polarizability compared to the lowest temperature material. This might be due, for example, to a low-frequency mode that is present only in material with intermediate range order.

3.5 Conclusions

The effect of deposition temperature on the dielectric constant can now be summarized. In the middle range 120 °C to 250 °C, the highest dielectric constant (~55) is achieved for an amorphous, densified thin film. At lower temperatures, the dielectric constant is half that of the optimal material; this difference cannot be explained by an increase in molecular volume. At higher temperatures, multiple crystalline phases may form; the observed dielectric constant depends on which of these phases nucleates. This variability leads to inconsistency from sample to sample.

CHAPTER 4

REACTIVE SPUTTER DEPOSITION OF AN OXIDE FILM AND THERMAL OXIDATION OF A METAL ALLOY FILM (DYSPROSIUM-SUBSTITUTED TITANIUM DIOXIDE)

In addition to substrate temperatures, several other deposition parameters can affect the properties of a sputtered dielectric film. In this chapter, we primarily consider reactive deposition parameters, including sputtering pressure, and gases, target power, and target-substrate distance. In particular, we consider the effect of each on the film's elemental composition which, in turn, affects the film's dielectric properties. We additionally consider the choice of base electrode material and its effect on measurements of capacitance and leakage current density. Finally, in Section 4.4, we compare the dielectric properties of reactively sputtered films to those of oxides prepared by metal deposition, followed by *in-situ* thermal oxidation.

For this chapter, the dielectric material is TiO_2 with a ~23 % dysprosium cation substitution.

Daniel Ruebusch and John Hevey contributed to the work reported in this chapter as undergraduate researchers.

4.1 Previous work on rare-earth substituted titania

Titanium dioxide has an attractively high dielectric constant for a unary oxide, $\varepsilon_r \sim 35 - 110$ [6]. High leakage current is observed, however, making it an unacceptable choice in applications with stringent leakage requirements. The

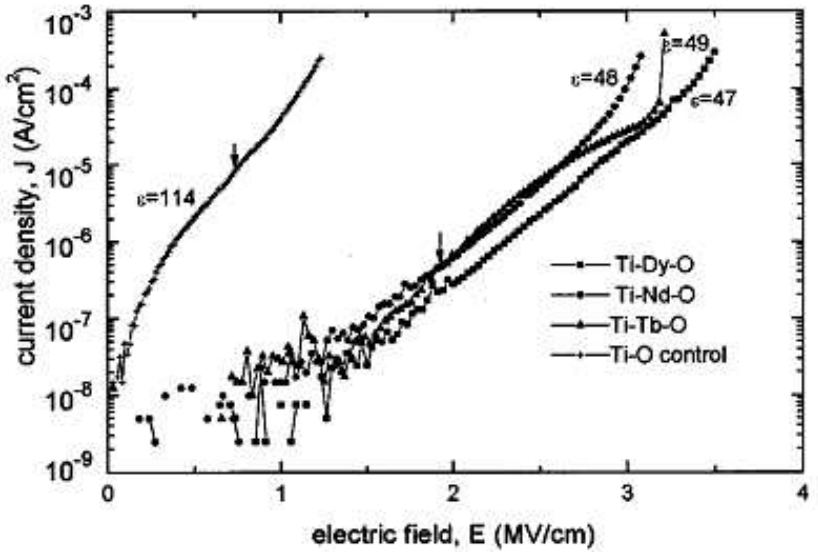

Figure 4.1: Leakage current density versus electric field for Dy, Nd, Tb substituted TiO_2. From Reference [24].

leakage has been attributed to the relative stability of two oxidation states for titanium, Ti^{4+} and Ti^{3+}, the low band gap (E_g ~3 eV), and the small band offset to silicon [27].

Substitution with rare-earth elements has been found to decrease the leakage current of amorphous titanium dioxide by three orders of magnitude at comparable electric fields [24]. The leakage current data from this study is reproduced in Figure 4.1. This study was done in a facing target, 90° off-axis substrate sputtering configuration with elemental targets of titanium and a variety of rare earths and early transition metals. Neodymium, terbium, and dysprosium at 5-15 atomic percent were found to be the most effective at decreasing leakage, presumably by passivating defects or electrostatically stabilizing the Ti^{4+} oxidation state. The substitution depressed the dielectric constant, from $\varepsilon = 114$ for pure titania to $\varepsilon = 47 - 49$ for substituted titanium oxide.

Rare earth oxides have the additional benefit of thermodynamic stability on silicon [19] and have been investigated for gate dielectric applications, most notably $LaAlO_3$ (Reference [66]). The electronic band gaps range from 4.5 to 5 eV; the gap of Dy_2O_3 is reported to be 4.5 eV [67]. Several other workers have investigated rare earth oxide substitution in titanium [25, 26] and hafnium [68] oxides for dielectric applications. Dysprosium substitution in sputtered hafnium oxide may decrease the leakage current over pure HfO_2 in a narrow composition range around 10 atomic percent, but also increases negative fixed charge [68]. Pan and Shu have studied both $Er_{1-x}Ti_xO_y$ [26] and $Nd_{1-x}Ti_xO_y$ [25] for use as gate dielectrics on silicon. Their films are prepared by reactively sputtering the lanthanide to a thickness of 3-7 nm; afterwards titanium metal is sputtered to a thickness of 2-7 nm. The stack is subject to a rapid thermal anneal (RTA) at 600-800°C in oxygen to complete the oxidation and interdiffusion of titanium and the lanthanide. This sample preparation technique allows screening of the optimal titanium content for low leakage and high capacitance, but does not differentiate between the effects of thickness and titanium concentration.

4.2 On-axis reactive sputtering from a U. S. gun

There are many sputtering parameters which can affect the deposition of the oxide film. Importantly, the controllable sputtering parameters (sputtering pressure, O_2 partial pressure, substrate to target distance and orientation, power to the target) do not independently affect the deposition parameters (deposition rate, energy and type of incident species, surface mobility). In this section, we compare the electrical characteristics of six reactively sputtered films of (Ti, Dy)$_x$O$_y$ in a MIM structure with platinum electrodes. All were sputtered con-

Table 4.1: Sputter deposition parameters for reactively sputtered (Ti, Dy)$_x$O$_y$, on-axis in Fenris

Run number	Power (W)/ DC bias (V)	Pressure (mT)	Target-substrate distance (cm)	Deposition time (min)	Comments
06f114	100/-435	30	3	10	.
06f115	75/-390	30	3	5	.
06f116	100/-459	30	4.5	5	.
06f117	100/-520	5	4.5	4	.
06f118	100/-502	5	3	2	.
06f119	50/-311	30	3	5	slight angle

secutively in Fenris during the same week from the same 2" target and gun; power to the gun, sputtering pressure, and substrate distance from the target were varied. Fenris is a larger chamber with three co-planar U. S. Gun sputter guns dedicated to sputtering oxides. The partial pressure of oxygen remained constant at 20% by volume O_2 in argon. The deposition parameters are given in Table 4.1.

Measurements and dielectric properties vary not only from film to film but also across a film as a function of distance from the center of the deposition track. In this section, where appropriate, we present data radially from the center of the target. The oxide is deposited on a 3" silicon wafer, precoated in an evaporated platinum layer 30 nm thick which serves as the base electrode. Measurements are made on a rectangular array of points (defined by the patterned top Pt electrodes) in the automatic probe station.

Table 4.2: Dielectric measurements for reactively sputtered (Ti, Dy)$_x$O$_y$, on-axis in Fenris

Run number	Cap. (pF)	Dissipation	Breakdown voltage (V)	Areal charge density (μC/cm^2)	Inferred thick. (nm) / dep. rate (/s)
06f114	40	0.015	<1 or 4	<1 or 3-4	180 / 3.00
06f115	105	0.020	~5 or ~8	2-4	70 / 2.33
06f116	140	0.020	5-6	2-3	52 / 1.73
06f117	100	0.018	1	<1	73 / 3.00
06f118	140	0.020	2	1-2	52 / 4.33
06f119	175	0.020	~1 or ~4	1-4	41 / 1.37

Before considering the radial variation, we consider measurements obtained from capacitors centered directly in front of the target. In Table 4.2, we give the capacitance and I-V data at the central position for each deposition. The final column of this table is an estimated deposition rate. Since film thickness was not measured for each of these films, we have assumed that the dielectric constant ε_r remains constant at 26 and estimated the film thickness, d, from the measured capacitance, C, according to $d = \varepsilon_o \varepsilon_r A/C$. This is not an ideal assumption, and error bars of 20 to 50 % are appropriate.

The deposition rate is very sensitive to changes to the deposition parameters. Deposition rate increases with increases to the target power and decreases with increases to the sputtering gas pressure and substrate-to-target distance. For $Ti_{0.77}Dy_{0.23}O_{1.9}$ within the range of parameters investigated, target power has the strongest effect on the deposition rate.

At these short target-substrate distances, low sputtering pressures can be highly damaging to dielectric properties. Both samples deposited with a sputtering pressure of 5 mT suffer from areal charge densities <2 $\mu C/cm^2$, largely because of low breakdown voltages.

The films subject to the highest deposition rates are also likely subject to the highest bombardment by negatively charged oxygen ions accelerated away from the biased target. Neutral argon atoms are also reflected off the target and bombard the depositing film. The damaging effects of bombardment are most obvious in deposition 06f117. The raw data for capacitance, dissipation, breakdown voltage, and maximum areal charge density are given in Figure 4.2; the radial symmetry militates for presenting the data as a function of distance on the substrate from the center of the sputtering fluence, as is done in Figure 4.3. The capacitance data behaves as expected, with a center region of high deposition rate (high thickness) directly in front of the target; outside of the target region, capacitance increases radially as the oxide thickness decreases and, possibly, the dielectric constant due to defect polarizations increases. The dissipation data similarly indicates a center region of $\tan\delta = 0.015$, with an abrupt transition to a region of $\tan\delta = 0.04$. Regions of high $\tan\delta$ values in the center is observed in all films prepared around this time, including some thermally oxidized films deposited in a sputter chamber dedicated to depositing metals, nitrides, and carbides (Tubby). High dissipation, or loss, can be due to non-ideal electrical contacts. In this case, the regions of high loss are consistently found in streaks at a certain angle to the square array of electrodes and are attributed to penumbra under the top electrode shadow mask due to slack in the mask. They do not noticeably affect I-V measurements.

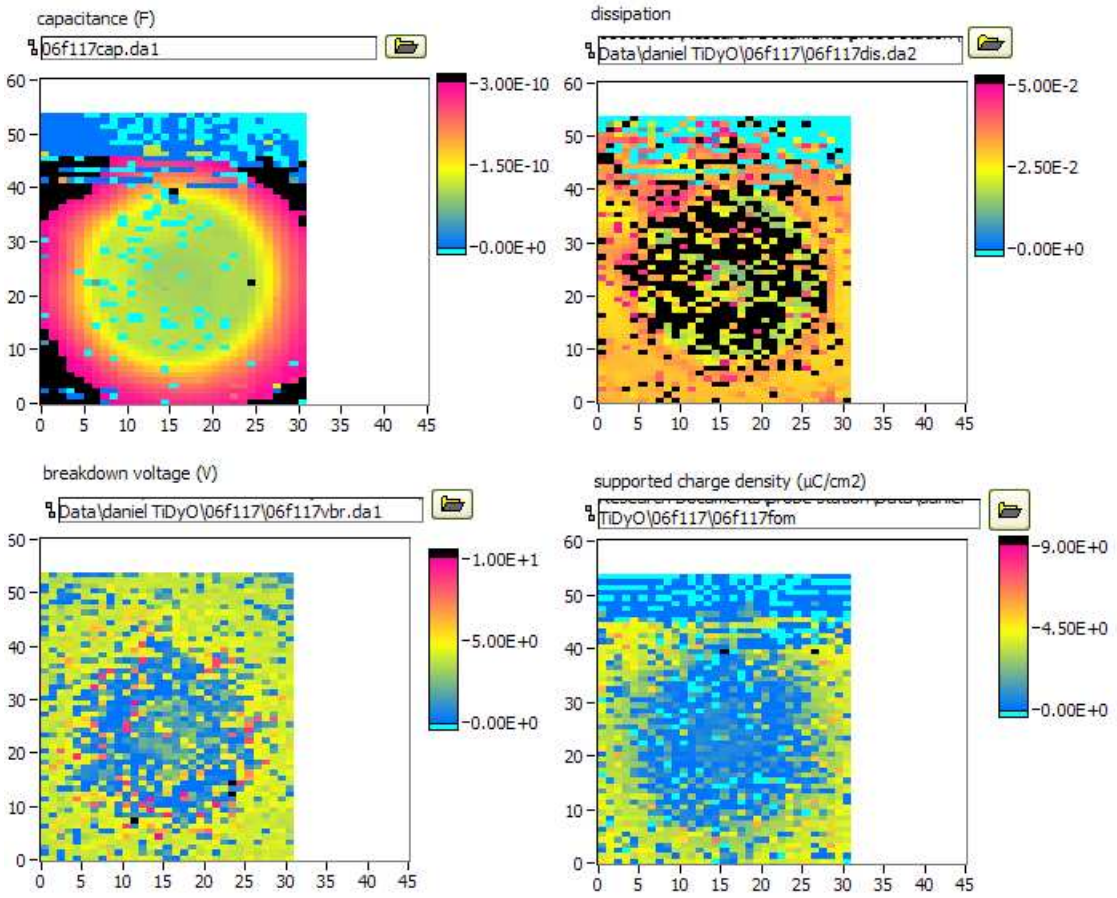

Figure 4.2: Raw dielectric data of on-axis reactively sputtered (Ti, Dy)$_x$O$_y$. Sample 06h117.

The I-V measurements reveal the stronger boundary between the region directly in front of the target and that slightly off-axis. Nearly all of the capacitors within the target region are shorts, with breakdown voltages < 1 V. Outside the target region, V_{br} increases to ~5 V and then slightly decreases radially. The areal charge density is calculated by CV_{br}/A and carries over the shape of the V_{br} map.

The bombardment energy of oxygen ions and ejected target particles is strongly related to the DC self-bias developed on the target. The target DC

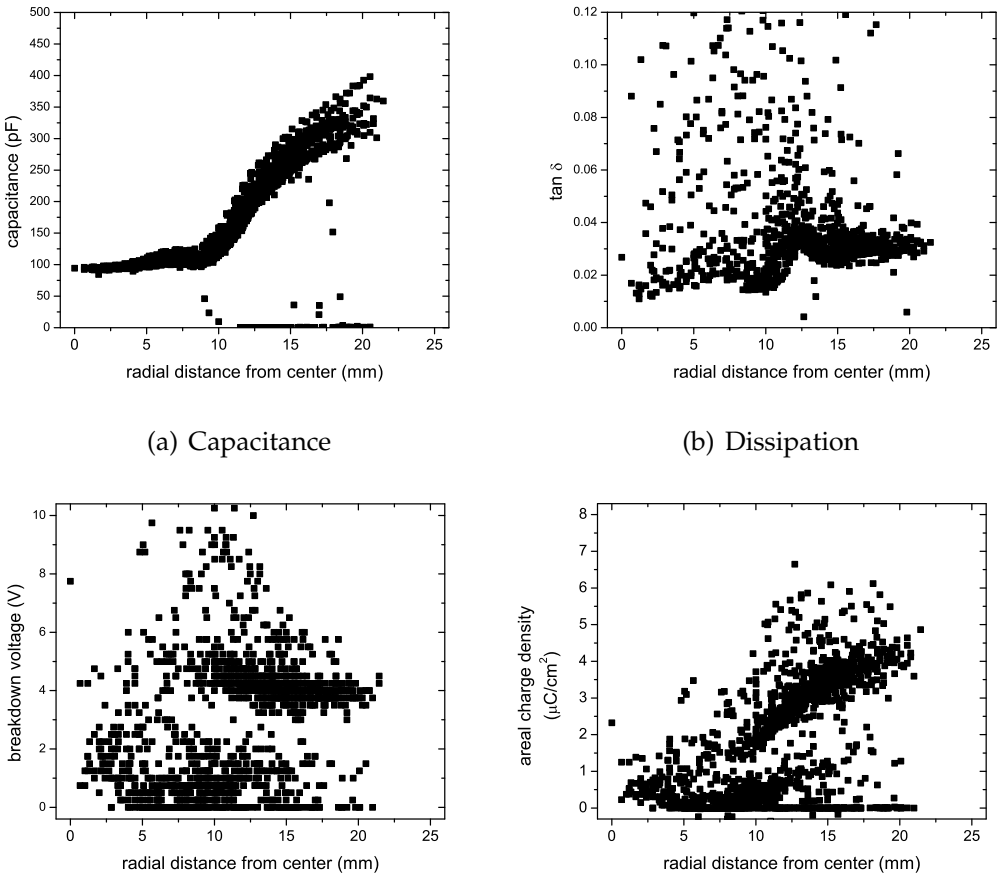

(a) Capacitance

(b) Dissipation

(c) Breakdown voltage

(d) Supported charge density

Figure 4.3: Dielectric properties of on-axis reactively sputtered $(Ti, Dy)_xO_y$. Sample 06f117.

voltage is itself a response to the greater inertia of argon ions than electrons at radio frequencies (13.56 MHz). Argon (Ar^+) ions are accelerated across the electric field and bombard the target with somewhat less energy than $eV_{\text{dc bias}}$. With some probability, they eject tantalum or TaO dimers with further decreased energy, $eV_{\text{dc bias}} - E_{\text{binding}}$, with a distribution in both energy and angle. These species bombard the substrate. Ar^+ ions are also reflected from the target with a distribution of momentum but are decelerated by the sheath field and con-

tribute little to the bombardment of the growing film. Neutral argon reflected from the target are not decelerated and bombard the substrate with some energy.

Undoubtedly, the plentiful negatively charged oxygen species (O_2^- and O^{2-}) contribute the majority of bombardment of the growing film. These oxygen ions are accelerated away from the target in the electric field and bombard the substrate [69]. Inelastic collisions with other particles along the path decrease the energy of bombardment; the number of inelastic collisions is proportional to the sputtering pressure. For the depositions given in Table 4.1, electric fields are ~100 V cm^{-1}, and thermal mean free paths are 1.7 mm at 30 mT and 1 cm at 5 mT. Energetic mean free paths are longer, and for sputtered species that leave the target with ≥5 eV, the mean free path is comparable to the size of the chamber [33].

The films deposited in Fenris have very high DC biases, implying highly energetic bombardment. We have found that similar choice of sputter deposition parameters in Hercules result in lower DC biases, with a DC bias of -320 V corresponding to a target power of 100 W rf, a sputtering pressure of 30 mT, and a substrate to target distance of 2.5 cm. There are many differences, however, between Fenris and Hercules. Sputtering pressure in Hercules is measured on a thermocouple gauge, rather than the Baratron gauge in Fenris, which likely leads to a more accurate pressure measurement in Fenris. Also, Hercules is a much smaller chamber than Fenris, and the proximity of the grounded chamber walls likely affect the electric fields and sputtering plasmas. For example, the gas pressure required to initiate a plasma with 100 W rf target power in Hercules is >120 mT, while in Fenris a gas pressure of 30 mT is sufficient.

As we discuss further, (Ti, Dy)$_x$O$_y$, specifically (Ti, Dy)$_x$O$_y$ on platinum base electrodes, may be particularly susceptible to damage, but many oxide films deposited on-axis on platinum substrates result in high quality dielectrics. Reactively sputtered $Zr_{0.2}Sn_{0.2}Ti_{0.6}O_2$ and Ta_2O_5, as well as thermally oxidized (Ti, Dy)$_x$O$_y$, behave well on these noble base electrodes.

4.3 Additional considerations in reactive sputtering

The films in the previous section were prepared in Fenris on 3″ wafers. In addition to enabling a controlled comparison of the effects of sputter deposition parameters, these films were also deposited on large enough substrates to consider the depositions at angles slightly offset from the sputter gun axis.

In this section, we consider (Ti, Dy)$_x$O$_y$ films prepared by on-axis reactive sputter deposition in Hercules. In general, the substrates used for these depositions were oriented directly on-axis with respect to the sputtering target and had an area too small to evaluate regions of the film deposited at a large oblique angle. Instead, in this section, we consider the effect of sputter parameters on the elemental composition of the film. We also evaluate dielectric measurements of films deposited on different base electrodes.

4.3.1 Dysprosium content and the dielectric constant

The study by van Dover [24] suggests that a small substitution of 5-15 atomic % of a rare earth can decrease the leakage current through titanium dioxide. The dielectric constant of pure Dy_2O_3 is 13, however [54]. The substi-

tution of the rare earth cation, then, should depress the dielectric constant of the pure titanium dioxide, with its dielectric constant of 35 to 90. In Figure 4.4, we present the dielectric constant of various dysprosium substitutions in titanium dioxide, including the known pyrochlore compound $Dy_2Ti_2O_7$ with ε_r = 24.1 at 1 kHz [54]. To our knowledge, there is no data on the other known compound, Dy_2TiO_5. In this material system, the decrease in dielectric constant is rapid with increasing dysprosium content and may be even more depressed in the present study.

One cause for variation within the measured dielectric constants in this system is the hygroscopy of rare earth oxides. Moisture absorption is observed in La_2O_3 and depresses the dielectric constant given the increased molar volume of the hydroxide over the oxide [70].

4.3.2 Elemental composition and re-sputtering

Deposition from an alloy target raises the question of film composition. The sputtering target is an alloy with elemental composition 80:20 Ti:Dy. Rutherford backscattering (RBS) analysis of the composition of the deposited film reveals an oxide material that is consistently Ti-poor compared to the target composition. RBS is not sufficiently sensitive to light elements such as oxygen to make any quantitative conclusions about the extent of oxidation. Given the sputtering gases of 20% O_2 in argon and the insulating nature of the film, the film is assumed to be fully oxidized. A small amount of argon (~1%) is also incorporated into the film at a level is comparable to that typically found in Ar-sputtered films [38]. Table 4.3 gives the cation compositions of films for several Ti-Dy and

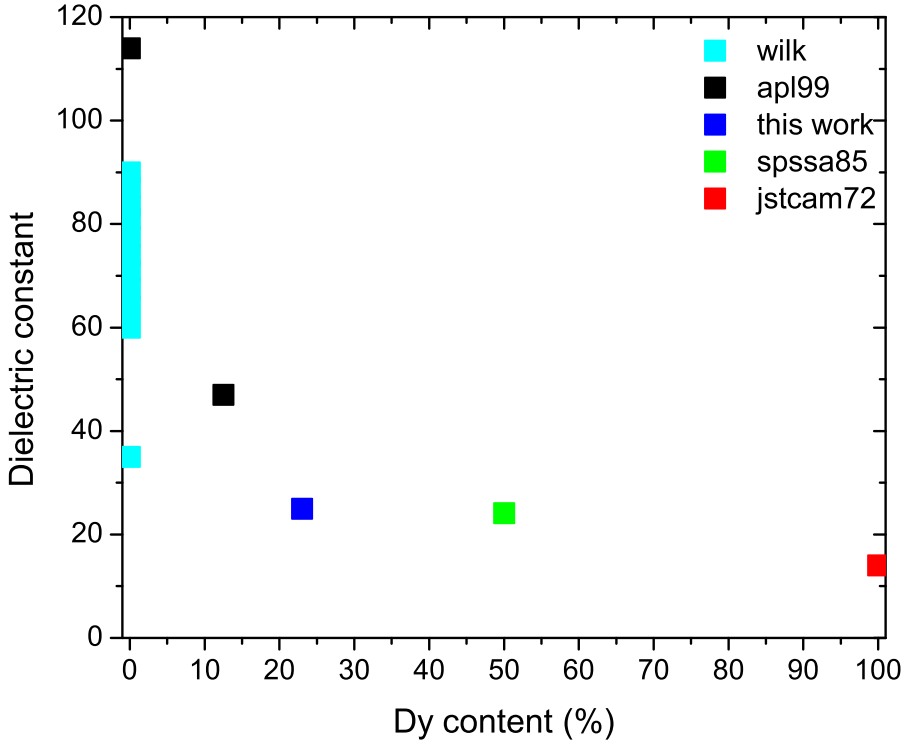

Figure 4.4: A comparison of dielectric constants of (Ti, Dy)$_x$O$_y$ for different Dy contents. Reference [24] is given as 'apl99', and Reference [6] as 'wilk'. Others are from a survey of research compiled by Shannon [54].

Zr-Sn-Ti oxide depositions.

The difference in composition between the target metals and cations in the oxide is remarkable, since sputter deposited films from alloy targets are widely assumed to have the same composition as the target material. This assumption stems from a steady-state analysis. We consider an alloy target of elements A and B, with A having a much larger cross-section to sputtering than B [33]. We may expect that a film deposited from such a target would be A-rich, compared

Table 4.3: RBS analysis for the composition of films reactively sputtered from an alloy target, powered to 100 W rf.

Material / Sample	Substrate-target distance [cm]	Sputtering pressure [mT]	Target composition	Film composition
Ti:Dy 06h94	2.5	5	80:20	73:27
Ti:Dy 06h12	2.5	30	80:20	77:23
Ti:Dy 06h95	7.5	30	80:20	69:31
Ti:Zr:Sn 05h01	2.5	7	60:20:20	65:18:16
Ti:Zr:Sn 05h01	5	7	60:20:20	56:18:25

to the target composition. After a certain sputtering time, however, the sputtering surface of the target is depleted in A, resulting in a decrease in the sputtering rate of A compared to B. In steady state, the sputtering rate of A is comparable to that of the target composition. This is not an equilibrium state, but since diffusion from the target bulk to the target surface is slow at room temperature, we conclude that a stable non-bulk surface composition is formed and yet that the composition of sputtered material is the same as the bulk target composition.

We note, however, that this analysis does not require that the composition of the film is the same as the composition of the alloy target, only that the composition of the material sputtered off the target is the same as the composition of the alloy target. The distinction stems from two additional considerations. First, one element may be scattered more easily in the sputtering gas, such that the arrival rates at the substrate are different than the sputtering rates leaving the target. Secondly, one element may be more easily resputtered off the substrate after arrival.

With these two considerations in mind, we evaluate the cation compositions of the films in Table 4.3. Consider Samples 06h12 and 06h95. At comparable sputtering pressures (30 mT) and greater substrate to target distances (2.5 cm and 7.5 cm, respectively), films are increasingly Ti-poor compared to the target composition. A similar trend is found with increasing substrate-target spacing in Ti:Zr:Sn samples; however, in this material system, composition on the more closely spaced substrate is titanium-rich compared to the sputter target. Sputtered Ni-Ti films from alloy targets are often found to be Ti-poor; this is attributed to titanium's more spatially disperse flux in sputtering and to differences in oxide formation [71]. Greater substrate to target distances can aggravate the depletion of titanium due to a disperse titanium flux.

The difference in composition between the dysprosium-substituted titanium oxides at short substrate to target distances bear further investigation. We find that the film deposited with a high sputtering pressure has a greater titanium concentration than the film deposited with a low sputtering pressure. Intuitively, it would seem that high sputtering pressure would have the same effect as increased substrate to target distance, since both increase the number of scattering events between leaving the target and arriving at the substrate.

There are two possible explanations here. The first is simply that the RBS composition analysis was performed off-center to the sputter fluence. Ho *et al.* have demonstrated that the disperse angular distribution of titanium can result in a 5-8 % off-stoichiometry in NiTi sputtered from an alloy target [72]; the elemental composition by RBS ranged from 5 % titanium-poor to 8 % titanium-rich with increasing off-set angle (0-70°) from the target normal.

An alternative explanation is that the titanium is resputtered at a greater

rate than dysprosium at these low pressures. Heat of sublimation can be used as an indicator of the surface binding energy and hence of the ease of sputtering [73]. Titanium has a higher heat of sublimation (4.8 eV/atom) than dysprosium (3.0 eV/atom) [53], indicating that dysprosium is the easier to the two to resputter from the substrate. Titanium scarcity at low sputtering pressures can therefore not be attributed to the preferential resputtering of titanium from the substrate.

The elemental composition of the sputtered film can strongly affect the dielectric properties and is strongly dependent on the distance from the target and sputtering pressures. As we have seen, however, distance from the target and sputtering pressures also strongly affect the deposition rate and arrival of other energetic species. The coupling of these effects with elemental composition as well must be taken into account in the interpretations of dielectric properties of a sputtered film.

4.3.3 Nitrogen substitution in (Ti, Dy)$_x$O$_y$

In addition to dysprosium substitution for titanium, we have substituted nitrogen for the oxygen to form a (Ti,Dy)$_x$O$_y$N$_z$. Recent developments in silicon oxide for gate dielectric applications has focused on silicon oxynitride, SiO$_x$N$_y$. The benefit of switching to silicon oxynitride can largely be attributed to its greater dielectric constant. The leakage current through the oxynitride is less than the leakage through silicon dioxide of the same areal capacitance; however, since leakage current through a gate dielectric is dominated by Fowler Nordheim tunneling, the decrease in leakage can be explained by the lower tunneling

probability through the thicker oxynitride [6, 14]. There have additionally been studies suggesting that low concentrations of nitrogen at the SiO_xN_y-Si interface improve device performance by decreasing the carrier effective mass [14].

Taking the cue from silicon dioxide research, researchers in alternative gate dielectrics have also pursued nitrogen substitution as a way to increase dielectric constant and improve interfaces with silicon. Hafnium oxynitride has demonstrated lower leakage currents and lower equivalent oxide thickness (EOT) than unsubstituted HfO_2 of the same physical thickness [74]. ('EOT' is commonly used by silicon device researchers to compare high κ dielectrics to SiO_2; it refers to the thickness of SiO_2 which would lead to same areal capacitance [9].) Additionally, it is suggested that Si-N bonds at the interface and Hf-N bonds in the bulk interfere with oxygen diffusion through the film [74] and that nitrogen incorporation increases the crystallization temperature and decreases surface roughness after annealing [75].

To deposit Ti-Dy oxynitride, the sputtering gas flow rates were changed to a 4:1:1 ratio of $Ar:O_2:N_2$. This deposition is compared to a similar deposition of Ti-Dy oxide in which the flow rates were 4:1 $Ar:O_2$. The sputtering gas total pressure for both depositions was 30 mT, while the target power was 100 W. Total deposition time was two minutes.

Given the difference in argon partial pressures, the deposition rates are not assumed to be equal for this films. Without thickness measurements, we may not interpret dielectric constant or electric fields and instead limit ourselves to reporting capacitances and leakage currents at a specified areal charge density on the electrodes, defined by $Q/A = CV/A$. The capacitance and dissipation factor of the Ti-Dy oxide are ~220 pF and ~0.017, respectively, while the Ti-

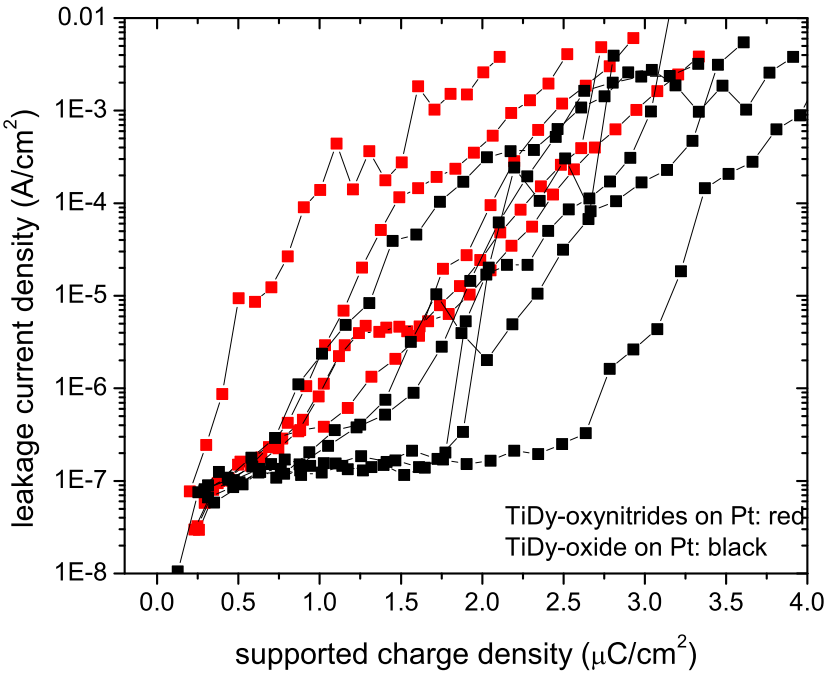

Figure 4.5: Leakage current density versus supported charge density from representative capacitors of $(Ti,Dy)_xO_y$ [Run 06h106] and $(Ti,Dy)_xO_yN_z$ [Run 06h081]

Dy oxynitride has a capacitance of ~184 pF and dissipation factor of ~0.025. In Figure 4.5, we plot the leakage current versus areal charge density for four representative capacitors of Ti-Dy oxide and Ti-Dy oxynitride. The increased leakage in the oxynitride is pronounced.

We consider the increase in leakage current by considering the effect of nitrogen on the band gap of the dielectric material. For many group III or IV elements, the nitride has a smaller band gap than the oxide. The electronic band gap of SiO_2 is 8.9 eV, while the band gap of Si_3N_4 is 5.3 eV [15]. Similarly, while aluminum oxide has E_g = 8.8 eV, its nitride has E_g ~6.2 eV [76]. There is lim-

ited published data on band gaps of rare-earth- substituted titanium oxide or nitride, but we gain insight by comparing TiO_2 (dielectric or wide-band gap semiconductor with E_g=3.0 to 3.2 eV) to TiN, which is a metal with no appreciable band gap. TiN, in fact, is used as a metal gate for high-κ dielectrics in nMOS transistors [77]. Nitrogen substitution in TiO_2, therefore, increases leakage due to increasing the density of midgap states, facilitating hopping conductivities. A similar effect might be expected in our Dy-substituted TiO_2.

While the increase in leakage current itself is undesirable, it confirms that introducing nitrogen into the sputtering gas results in nitrogen incorporation in the film. The amount of nitrogen actually incorporated into the film is unknown, and few techniques distinguish between these similar and relatively light-weight elements. (Auger electron spectroscopy may be a possibility as in Ref. [75].)

4.3.4 Choice of base electrode materials

To clarify the effects of the base electrode on the performance of the capacitor, we performed identical depositions of $(Ti, Dy)_xO_y$ on three different base electrodes: evaporated platinum on an evaporated chromium sticking layer, evaporated nickel on an evaporated chromium sticking layer, and sputtered titanium nitride prepared in an IC fabrication facility at Bell Labs. The oxide was deposited in Hercules at 100 W RF gun power, 20% oxygen in argon sputter ambient at 30 mTorr, on substrates held 2.5 cm from the on-axis Angstrom sputter gun. The thickness of the film in each case is 38 nm, with a deposition rate of 3.2 /s. In Figure 4.6, we plot the leakage current versus electric field for

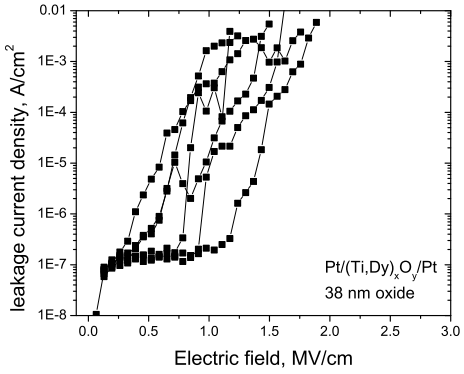

(a) Pt/(Ti,Dy)$_x$O$_y$/Pt

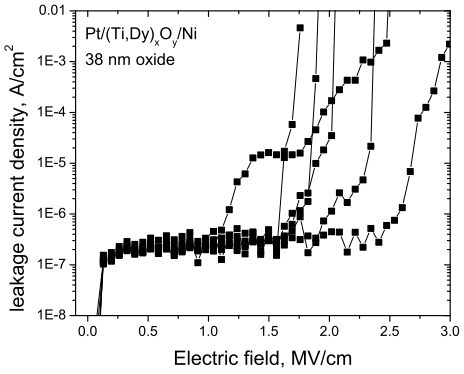

(b) Pt/(Ti,Dy)$_x$O$_y$/Ni

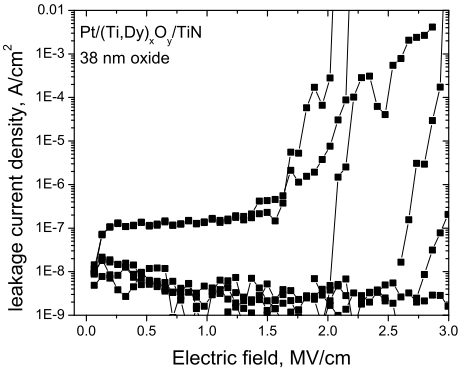

(c) Pt/(Ti,Dy)$_x$O$_y$/TiN

Figure 4.6: Leakage current density versus electric field of reactively sputtered (Ti,Dy)$_x$O$_y$ on different electrodes: (a) 300 evaporated platinum on 300 evaporated chromium, (b) 300 evaporated nickel on 300 evaporated chromium, (c) sputtered TiN on silicon. Sample 06h106 on Pt, 06h086 on Ni, and 06h030 on TiN.

representative capacitors of (Ti, Dy)$_x$O$_y$ films deposited on TiN, Ni, and Pt base electrodes. For all three, the top electrode is platinum evaporated through a shadow mask; this top electrode is biased negatively during the voltage sweep, such that electrons are injected from the top electrode. The electric field is calculated by normalizing the applied voltage to the 38 nm of deposited oxide.

Table 4.4: Capacitance measurements for reactively sputtered samples of $Ti_{0.77}Dy_{0.23}O_{1.9}$ on different base electrodes

Sample	Base electrode	Capacitance (pF)	Dissipation	Effective dielectric constant
06h106	Pt	184	0.022	25
06h030	TiN	162	0.008	22
06h086	Ni	222	0.034	30
06h119	Ni, 150°C	215	0.015	29

While most capacitors reveal a current density of about 10^{-7} A cm^{-2} at low electric fields, the increase in leakage current with electric field is markedly different on each base electrode. Compared to capacitors with two platinum electrodes, capacitors formed on nickel or TiN maintain low leakage to higher voltages, but also suffer harder breakdowns, during which the current increases rapidly with little increase in applied voltage.

We also note that the capacitances for these nominally identical oxide depositions are different, with the highest capacitance value (by 37 %) found for the sample deposited on nickel. In Table 4.4, we give the raw capacitance and dissipation values for these three nominally identical depositions on the three base electrode materials. Effective dielectric constants are calculated by assuming that the measured capacitance is due entirely to an oxide thickness of 38 nm for all depositions. The measured capacitance, however, is due not only to the nominally identical (Ti, Dy)$_x$O$_y$ layers but also to any capacitances in series with the (Ti, Dy)$_x$O$_y$. An interfacial, adventitious oxide between the target oxide and an electrode is a likely contributor to series capacitances.

The total capacitance measured for a series materials stack, C_{measured}, is given by

$$\frac{1}{C_{\text{measured}}} = \frac{1}{C_{\text{interfacial}}} + \frac{1}{C_{\text{TiDyO}}} \tag{4.1}$$

in which $C_{\text{interfacial}}$ and C_{TiDyO} represent the capacitances of the interfacial and $(\text{Ti,Dy})_x\text{O}_y$ layers, respectively. Interfacial layers, therefore, always decrease the measured capacitance from that of the capacitance inherent to the $(\text{Ti,Dy})_x\text{O}_y$ layer. (A parallel capacitance, in contrast, increases the measured capacitance above that of the $(\text{Ti,Dy})_x\text{O}_y$.)

The measured capacitances in Table 4.4 are surprising since we expected that oxide depositions on the platinum electrode were least likely to induce an interfacial layer, compared to depositions on Ni or TiN. For this reason, we expect capacitors prepared on the noble platinum base electrodes to have the highest capacitance. Instead, we find that the highest capacitances are observed for the capacitors prepared on nickel base electrodes.

If we assume that the capacitance measured in the $\text{Pt}/(\text{Ti,Dy})_x\text{O}_y/\text{Ni}$ capacitors are due exclusively to the thickness of $(\text{Ti,Dy})_x\text{O}_y$, i.e. C_{TiDyO}=222 pF, then we may calculate the necessary series capacitance of an interfacial layer on the other base electrodes. The capacitance of the interfacial layer in $\text{Pt}/(\text{Ti,Dy})_x\text{O}_y/\text{Pt}$ capacitors is 1075 pF, or when normalized to the area of the top electrode, 34 $\text{fF}/\mu\text{m}^2$. This capacitance could be caused, for example, by a 1 nm thick layer of $\varepsilon_r = 3.9$. Li *et. al.* have demonstrated that up to 2.5 nm of PtO_2 with refractive constants $n = 1.85$ and $k = 3.4$ can form on thin film platinum exposed to an oxygen plasma [78], such that an interfacial layer of 1075 pF can be explained by the formation of PtO_2 in the Ar/O_2 plasma. To our knowledge, there is no published data on the dielectric constant of PtO_2 at

these frequencies; the optical data reported by Li *et. al.* give an optical dielectric constant $n^2 \sim 3.4$.

For the Pt/(Ti,Dy)$_x$O$_y$/TiN capacitors, the interfacial capacitance is 599 pF, or 19 fF/μm^2, which could be explained, for example, by material of thickness 1 nm and $\varepsilon_r = 2$ or thickness 20 nm and $\varepsilon_r = 43$. Oxidation of 50 nm sputtered TiN has been demonstrated during anneals in molecular oxygen at 650 °C [79]. As we have seen, the dielectric constant of TiO_2 can range from 30 to 110, such that we might imagine that the interfacial capacitance layer is due to tens of nanometers of relatively high dielectric constant TiO_2.

The high thickness of the suggested interfacial layer in the Pt/(Ti,Dy)$_x$O$_y$/TiN capacitors has a profoundly different effect on leakage currents than a ~1 nm interfacial layer in the Pt/(Ti,Dy)$_x$O$_y$/Pt capacitors. The voltage drop across each layer is related to the capacitance of the layer. In the simple bilayer structure we imagine here, the voltage drop across the interfacial layer, $V_{\text{interfacial}}$, is given by

$$V_{\text{interfacial}} = V_{\text{applied}} \frac{C_{\text{TiDyO}}}{C_{\text{TiDyO}} + C_{\text{interfacial}}} \tag{4.2}$$

in which V_{applied} is the applied voltage. In the case of Pt/(Ti,Dy)$_x$O$_y$/TiN capacitors, 27 % of the applied voltage is dropped across the interfacial layer, and in Pt/(Ti,Dy)$_x$O$_y$/Pt capacitors the interfacial layer drops 17 %. In the case of a nanometer thick interfacial PtO_2 on the platinum base electrodes, 17 % of the applied voltage (0-10 V_{dc}) can induce a significant tunneling current across the interfacial layer to the (Ti,Dy)$_x$O$_y$ film. An insulating interfacial layer of ~20 nm thickness on the TiN electrode, in contrast, may be current limiting for the oxide dielectric stack. The capacitors in Figure 4.6 break down at 8 V. If we assume an interfacial thickness of 20 nm, the electric field across the interfacial layer at breakdown is 1.1 MV/cm, while that across the (Ti,Dy)$_x$O$_y$ is 1.5 MV/cm. It is

possible then that the $(Ti,Dy)_xO_y$ has already broken while the series interfacial layer remains current limiting.

We have assumed in this analysis that there is no interfacial layer when sputtering on a nickel base electrode. While this is a simple assumption that allows us to compare depositions on platinum base electrodes to those on TiN, it is unlikely to be strictly true. An alternative possibility is that the interfacial layer on nickel base electrodes has a higher capacitance than the interfacial layer on either platinum or TiN; therefore it depresses the stack capacitance by a smaller amount. To consider the potential interfacial layers on nickel, we note that NiO has a dielectric constant of 11.9 [80] and is thermodynamically more likely than platinum oxide. Up to 3 nm of NiO may form at a higher capacitance than the 1075 pF inferred on the platinum electrode.

The formation of NiO is suggested in comparing $(Ti,Dy)_xO_y$ sample 06h086 to $(Ti,Dy)_xO_y$ sample 06h119. Both were deposited on a nickel base electrode with identical deposition parameters except that the substrate was intentionally heated to 150 °C during the latter deposition. The raw capacitance for this latter deposition (again in Table 4.4) dropped to 215 pF, and the dissipation to 0.015. While the capacitance of the $(Ti,Dy)_xO_y$ itself does not change at these moderate temperatures (see Section 4.4), we have seen the thickness of an interfacial layer increase with increased substrate temperatures during reactive sputter depositions. (When reactively sputtering $Zr_{0.2}Sn_{0.2}Ti_{0.6}O_2$ on bare silicon, the interfacial SiO_2 thickness increased from 4 nm at 200 °C to 7 nm at 500 °C, as observed in cross-sectional TEM.) The decrease in dissipation is consistent with the lower dissipation observed in depositions on TiN with a (assumed) thicker interfacial layer.

Finally, we note that there is a more definitive method of analyzing the dielectric constant of the $(Ti,Dy)_xO_y$ and the capacitance of the interfacial layer: prepare capacitors of many $(Ti,Dy)_xO_y$ thicknesses. We can then exploit the relationship among capacitance, dielectric constant, and film thicknesses for series capacitors, namely:

$$\frac{C_{\text{measured}}}{A} = \frac{\varepsilon_1}{t_1} + \frac{\varepsilon_2}{t_2} \tag{4.3}$$

in which ε_i and t_i are the dielectric constant and thickness, respectively, of the ith layers of the dielectric stack. Plotting C_{measured}/A versus $1/t_{\text{TiDyO}}$ gives both the dielectric constant of the $(Ti,Dy)_xO_y$ layer (the slope) and the areal capacitance of the interfacial layer (intercept as the $(Ti,Dy)_xO_y$ layer thickness becomes large). This experiment has not been performed to date.

The base electrode is additionally a factor in gauging the damage done by oxygen bombardment in reactive sputtering. We see in the reactive sputtering of $(Ti,Dy)_xO_y$ samples in Hercules that samples with platinum base electrodes can have less than 60 % yield due to shorted capacitors found in the region of the film directly on-axis to the sputtering gun. Though many fewer depositions were prepared on TiN or nickel films, the shorted capacitors on these films do not demonstrate the same spatial distribution of bad capacitors. Oxide films deposited on TiN base electrodes have comparable yield (~65 %); however, bad capacitors are distributed throughout the sample. Samples deposited on nickel base electrodes, as in Figure 4.16 (supported areal charge density versus cumulative probability), have a yield of ~90 %. We may interpret these results to conclude that a thin interfacial oxide layer, while contributing to a decreased stack capacitance, is important to increasing yield and quality.

Other workers have found similar results in forming metal-insulator-metal

capacitors. HfO_2 formed by ALD exhibits a lower reliability and lower effective dielectric constant when deposited on platinum than on iridium or ruthenium, two metals whose oxides are also conductors [81]. Similarly, deposition of the ferroelectric $Pb(Zr,Ti)O_3$ on oxidized platinum is found to improve resistance to fatigue over deposition on pure platinum [82].

We have argued that chemical interactions (namely, the growth of an interfacial layer) may occur between the sputtered oxide and the underlying base metal, affecting evaluation of the target oxide's dielectric properties. The structure of the oxide itself, however, may be affected by the surface structure of the metal film. In Figure 4.7, we evaluate the roughness of the base electrode candidates: evaporated Pt/Cr, evaporated Ni/Cr, and sputtered TiN. The root-mean-squared roughness for these films are found to be 0.605 nm, 0.676 nm, and 0.839 nm, respectively. Despite differences in the structure of the films' surfaces, the roughnesses are very similar and relatively low; therefore, roughness of the base electrode prior to oxide deposition does not appear to be a contributing factor to the differences in leakage currents. We note, however, that the force measurements are taken over a sample size of 1 micron, while the area of the capacitor is 200 microns in diameter. We can say very little, therefore, about the distribution/probability of larger size defects.

We also observe that a roughness of this level may contribute to our inability to sputter reliable capacitors at less than ~10 nm thickness on metallic base electrodes. We also are unable to determine anything about the roughness of the base film after oxide deposition and note that sputtering on high surface energy metals such as Ag or Au is found to affect the metal's structure.

The choice of base electrode material clearly has a strong effect on the eval-

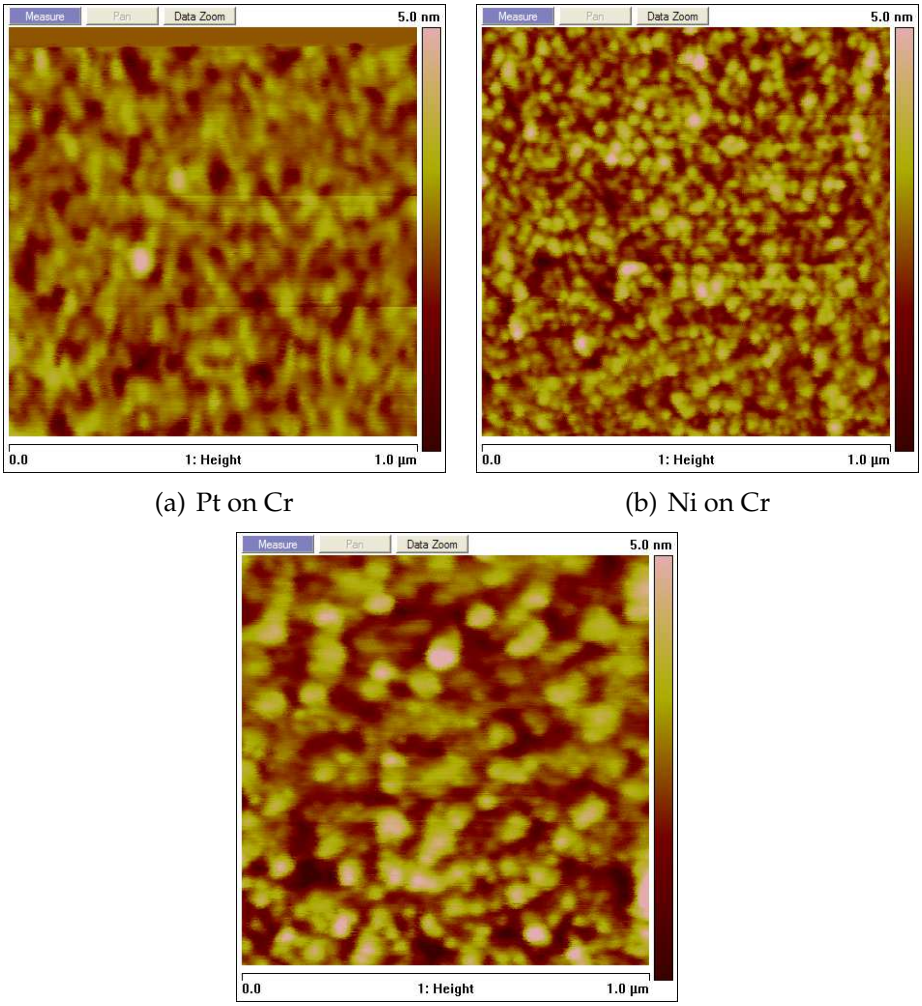

(a) Pt on Cr

(b) Ni on Cr

(c) TiN on Si

Figure 4.7: Atomic force microscopy (AFM) scans of base electrode films: (a) evaporated platinum on evaporated chromium, (b) evaporated nickel on evaporated chromium, (c) sputtered TiN on silicon. Courtesy Maxim Noginov.

uation of an oxide's dielectric properties. While the effect of surface roughness may be insignificant, the kinetics of film growth at the interface of the base metal and the dielectric oxide affect measurements of both the capacitance and the leakage current densities. We have avoided the evaluation of metal-insulator-semiconductor (MIS) capacitor structures because of the perceived ease of evaluating dielectric properties on noble metals such as platinum; we had hoped to avoid the interfacial layer growth which commonly complicates the analysis of dielectrics deposited on silicon. An alternative to consider is a conductive oxide base electrode as in Ref. [81].

4.4 Thermal oxidation: a viable alternative to reactive sputter deposition?

There are several options for creating an oxide thin film by sputtering. One is the reactive RF sputtering of a metallic target in an Ar/O_2 sputter ambient as described throughout this thesis and in the prior section. A related technique is sputtering a ceramic oxide target in an Ar or Ar/O_2 sputter ambient; this technique requires the availability of an appropriate ceramic target which might commonly be brittle and therefore difficult and/or expensive to manufacture. Additionally, the deposition of a dielectric in the presence of oxygen increases the thickness of an adventitious, interfacial layer of low dielectric constant, commonly SiO_2 on silicon. Even after HF removal of native oxides prior to oxide deposition, reactively sputtered oxides from metal and ceramic targets, including HfO_2 [83, 84] and TiO_2 [32, 85], yield an interfacial silicon oxide layer of 2-4 nm. The interfacial layer is attributed to oxidation of the silicon wafer by

active oxygen species (oxygen radicals or oxygen ions) in the sputtering plasma prior to deposition of the high-k film [83, 84, 32]. Minimization of this interfacial oxide, and its associated low serial capacitance, is crucial to maximizing the areal capacitance of the gate dielectric stack.

A common technique to minimize the occurrence of subcutaneous oxide is the sputter deposition of a thin metal film in Ar ambient, followed by *in situ* post-deposition oxidation. Several groups have explored this technique using active oxygen species such as ozone, atomic oxygen, or an oxygen plasma [21, 86, 87]. Heat or ultraviolet radiation increase the kinetics of the oxidation reaction.

In addition to oxidation of a metal film, intermediate techniques are also suggested to minimize interfacial SiO_2. Reoxidation anneals of a suboxide have realized limited success [83, 84, 20]. Deposition of a thin metal film, followed by reactive deposition of the oxide film is a technique that, while viable, requires significant process optimization [88].

In this section, we compare the results of oxides prepared by reactive sputter deposition to those prepared by metal deposition with a post-deposition oxidation anneal. The oxide chosen is $Ti_{0.77}Dy_{0.23}O_{1.9}$.

4.4.1 Reactively sputtered oxide

The $Ti_{0.77}Dy_{0.23}O_{1.9}$ (hereafter, $(Ti,Dy)_xO_y$) film was deposited by RF reactive sputtering from a metallic 2″ target of the composition $Ti_{0.8}Dy_{0.2}$. The power to the target was 100 W (or 4.94 W/cm^2). The sputtering gases were 4:1 Ar:O_2, and

Table 4.5: Reactively sputtered samples of $Ti_{0.77}Dy_{0.23}O_{1.9}$

Sample	Power (W)	Sputter time (s)	Base electrode	Substrate temperature (°C)
06h106	100	1.005	Pt	ambient
06h141	100	120	Pt	200
06h145	100	120	Pt	250
06h144	100	120	Pt	300
06h143	100	120	Pt	365

the total pressure in the chamber was controlled at 30 mTorr by throttling the valve to the turbomolecular pump. Under these conditions, the deposition rate was 3.2 /s. The base pressure in the chamber prior to deposition was 4×10^{-6} Torr.

A list of $Ti_{0.7}Dy_{0.3}O_{1.7}$ samples prepared by reactive RF-sputtering is found in Table 4.5.

A strong indicator of a good quality dielectric is the dispersion with frequency, which may provide insight into the polarization mechanisms active in the oxide dielectric. In Figure 4.8, we plot the dispersion with frequency of the capacitance and loss tangent for a capacitor formed from a reactively sputtered oxide deposited on an unheated substrate. Over the measurement frequency range of 100 Hz to 500 kHz, we see a dispersion in the capacitance of less than 3 %. Since polarization due to electronic and ionic polarizability is active up to 10^{15} Hz and 10^{11} Hz, respectively, the dispersion to 1 MHz must be due to extrinsic effects. We attribute the dispersion from 100 Hz to 500 kHz to a small number of hydroxide ions incorporated in the films during deposition. The

increase in capacitance at 1 MHz is attributed to an artifact in our probing measurement, in particular to the parasitic capacitance of the coaxial cables leading to the LCR meter.

The dispersion in the loss tangent is likewise small at frequencies less than 100 kHz. At greater frequencies, the dissipation increases substantially, an effect that is again attributed to the coaxial cables leading to the LCR meter. (Commercial capacitors of comparable size show no dispersion when measured at the LCR meter's test fixture, but significant dispersion at high frequencies when measured through a similar length of coaxial cables.)

The limited dispersion observed in this reactively sputtered oxide indicates that the polarization mechanisms available in the film are invariant over the frequency range 100 Hz to 1 MHz. Ideally, to test the invariance of dielectric constant over the full operating range of electronic devices, we would make measurements up to 1-30 GHz. Measurements to 1 MHz, however, provide assurance that low frequency defect polarization mechanisms are not active within the film. These additive polarization mechanisms–orientational polarizations and hopping conductivities along dangling bonds, filling and emptying of trap states–may enhance the measured dielectric constant at low frequencies but are often damped out by 1 MHz, as described for specially prepared Ta_2O_5 in Chapter 5.

The polarizability, and hence the dielectric constant, of a metal oxide is highly dependent on the local coordination of the metal cations by oxygen and density of the film. In Chapter 3, we demonstrated how we may vary both of these attributes by varying the substrate temperature during oxide deposition. In Figure 4.9, we plot the dielectric constant and loss tangent, $\tan\delta$, for films

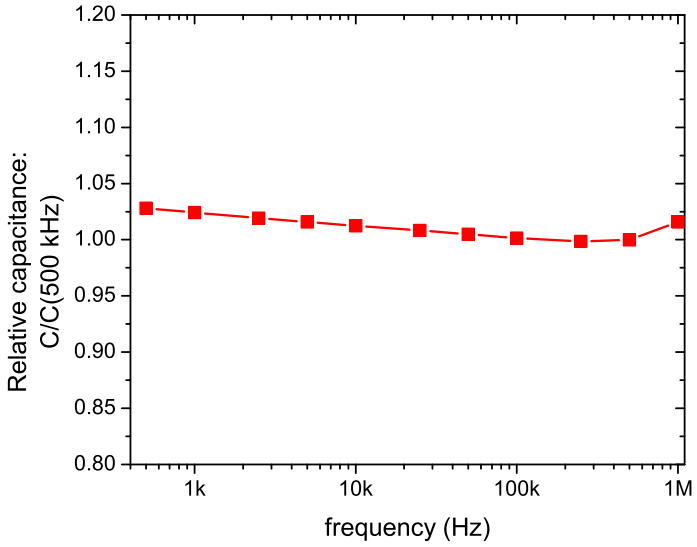

(a) Normalized capacitance

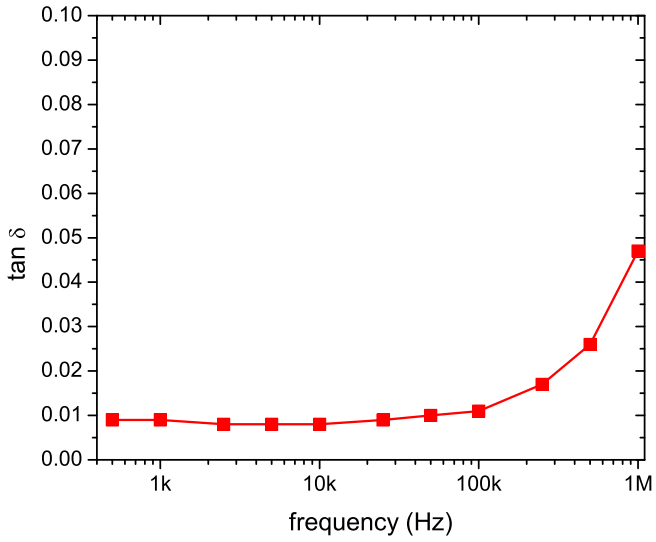

(b) Loss tangent

Figure 4.8: The dispersion of the capacitance and dissipation of reactively sputtered (Ti, Dy)$_x$O$_y$ deposited with no intentional heat to the substrate. The capacitance is normalized to the capacitance at 500 kHz. Sample 06h106.

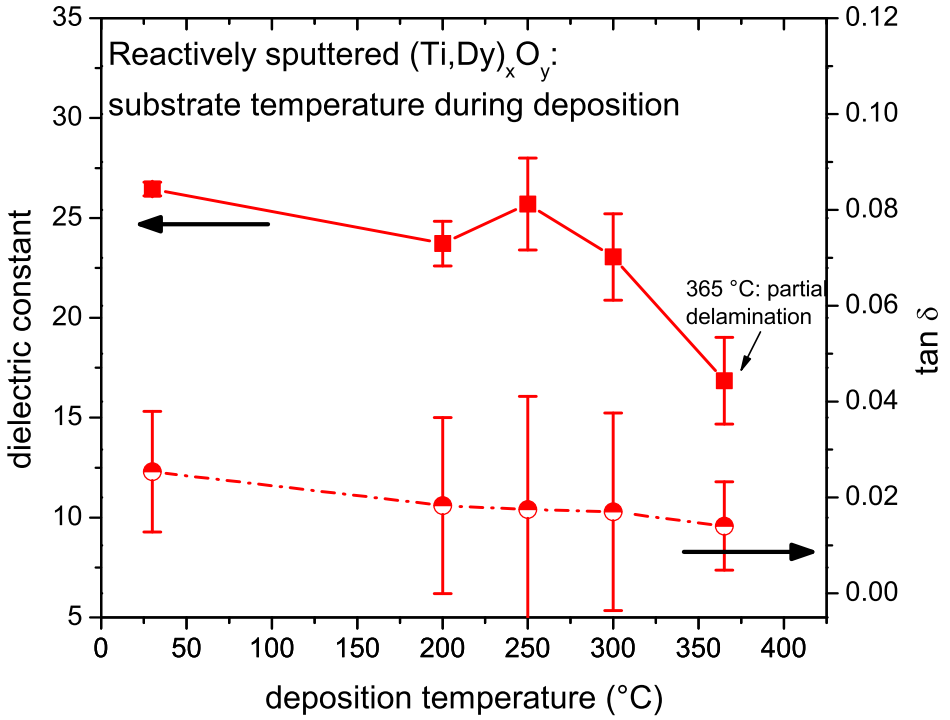

Figure 4.9: The median dielectric constant and loss tangent for reactively sputtered (Ti, Dy)$_x$O$_y$ as a function of the substrate temperature during deposition. All samples were deposited for 2 minutes at 100 W in 30 mTorr sputtering gases, 20% O_2 in Ar. The error bars represent a standard deviation. Samples 06h106, 06h141, 143-145.

deposited on substrates between 25 °C and 365 °C. For substrate temperatures less than 300 °C, the dielectric constant of the film is ε_r ~23-25. At 365 °C, the dielectric constant falls to ~17, suggesting a structural change within the film. Only weak crystalline peaks are observed, however, and may be identified with the platinum electrodes.

The effective dielectric constant drops to 17 when the oxide is deposited on

a substrate heated to 365 °C. The thickest part of the film–subject to the highest deposition rate and bombardment energies–is highly damaged, however, with high dissipation and high leakage currents. On examination of this material under a light microscope, we find delamination of the film to form low aspect ratio bubbles. The bubbling is particularly concentrated in the region of the film most directly in the line of sight of the sputtering fluence during oxide deposition. Images within and away from the line of sight from the film reactively sputtered at 365 °C are given in Figure 4.10.

The formation of bubbles is stress induced and has been observed in the preparation or deposition of thin films at high temperatures [89, 90, 91]. Differences in thermal expansion coefficients among the layered films lead to thermal stress. A similar effect has also been observed in the cleaning of crystalline silicon by argon ion bombardment (~1 keV) [92, 93]. In that case [92], the formation of bubbles was attributed to the argon incorporation in the silicon. The damage (bubble formation) increased dramatically with increased temperature of the silicon during bombardment, since the increase in temperature allows energy for bubble coalescence, resulting in 3-15 nm diameter bubbles at 800 °C.

Reactive sputter depositions on unheated substrates also give rise to damaged regions within the line of sight of the sputter fluence. The damage suggests that the oxide film is subject to atomic peening from high energy oxygen ions and reflected argon atoms; the film, particularly the region on-axis with respect to the sputter source, is under compressive stress. The film delaminates from the platinum electrode during depositions on heated substrates as the stress accumulates beyond a critical value related to the adhesion of the film to the substrate.

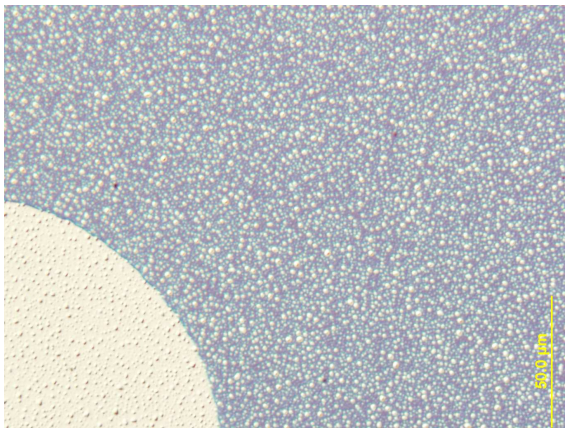

(a) Low magnification

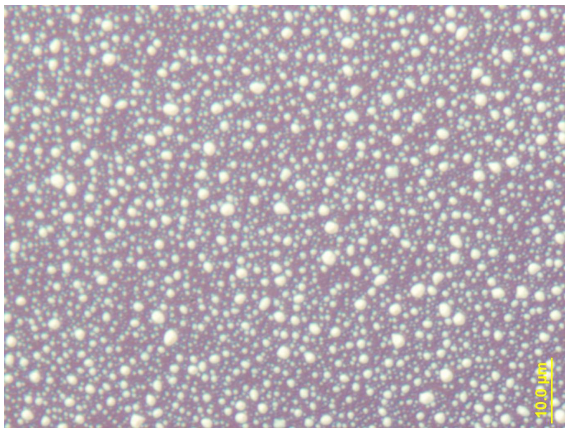

(b) High magnification

(c) Low magnification, off-center with respect to the sputtering fluence.

Figure 4.10: Reactively sputtered (Ti, Dy)$_x$O$_y$ at a substrate temperature of 365°C. The large white circles are the 200 micron diameter platinum electrodes. In part (c), we find no bubbling occurring off the axis of sputter fluence. Run number 06h143.

To a lesser extent, this stress is observed even in films deposited at 250 and 300 °C. Figure 4.11 gives light micrographs of the film deposited at substrate temperatures of 250 and 300 °C. The bubbles in films deposited at lower temperatures are less dense, though comparable in size. At 365 °C, there are enough stress-induced bubbles to affect the quantitative capacitance measurement, such that the dielectric constant is unknown. At lower temperatures, the measured dielectric constant remains high, likely because the capacitance measurements are still sensitive to the properties of the bulk (Ti, Dy)$_x$O$_y$ material.

Unlike the previous study of $Zr_{0.2}Sn_{0.2}Ti_{0.6}O_2$ [52] (Chapter 3), we find no improvement in dielectric properties with increased substrate temperature during reactive sputter depositions. By choosing sputter conditions to realize lower energy bombardment, we may avoid the stress incurred by bombarding argon and oxygen and enjoy a broad processing space (deposition temperatures up to 300+ °C) with negligible change in dielectric constant, ε_r ~25.

4.4.2 Thermal oxidation of a metal film

In this section, we investigate the feasibility of preparing the same oxide dielectric by deposition of the precursor metal alloy film, followed by an *in situ* oxidation anneal at elevated temperature in an atmosphere of molecular oxygen. As for most metals, the mechanism for oxidation of Ti-Dy is expected to depend on the diffusion of oxygen through the oxide to react at the buried oxide-metal interface. Oxygen diffusion is thermally activated (Arrhenius law), and therefore depends exponentially on the temperature of the oxidation anneal and weakly on the time of the anneal.

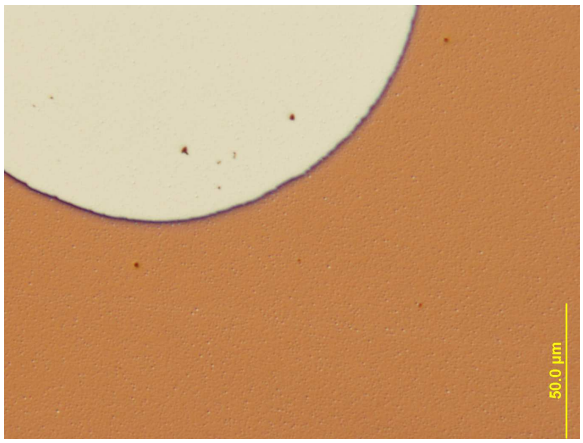

(a) Deposited at 250 °C

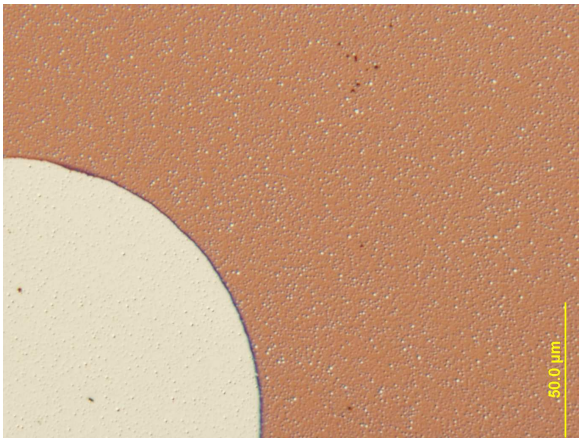

(b) Deposited at 300 °C

Figure 4.11: Reactively sputtered (Ti, Dy)$_x$O$_y$ at a substrate temperature of 250 and 300°. The large white circles are the 200 micron diameter platinum electrodes. Run number 06h145 and 06h144, respectively.

These samples were prepared in Hercules, a small sputtering chamber with a single on-axis sputter gun, on a 2″ resistive substrate heater. Metal films were RF-sputtered for thirty seconds from the metallic 2″ target and an unheated substrate. The power to the gun was 100 W RF, the sputter ambient was 50 sccm of argon at 30 mT, and the substrate was held on-axis with respect to the gun at a distance of 2.5 cm from the sputter target. After deposition, the argon was evac-

uated from the chamber, and the substrate resistively heated to 200 to 500 °C. At the desired temperature, 100 sccm of molecular oxygen at 1 Torr pressure was allowed to flow into the chamber. The oxidation time varied from 20 minutes to one hour. Samples were allowed to cool in vacuum to less than 70°C before being removed from the chamber. The base pressure in the chamber before deposition was 4×10^{-6} Torr.

Other oxygen species such as atomic oxygen, or ozone are much more reactive than O_2 and could be used to avoid the high temperatures necessary in this study. One concern about the high temperature anneals is the possible crystallization of the oxide. $Ti_{0.77}Dy_{0.23}O_{1.9}$ of 120 nm thickness was found to crystallize in a one hour post-deposition anneal in air at 620 °C.

The substrate for this study was evaporated platinum. Since platinum is a noble metal and its oxidation unlikely, we assume that oxidation stops once the sputtered Ti-Dy is fully oxidized. A future area of study for integration in silicon electronics is whether this would be the case for sputtered Ti-Dy on silicon. Over-oxidation of the Ti-Dy will result in oxidation of the silicon below, but there may be an adequate processing window to stop oxidation reliably at the Ti-Dy interface with Si.

A list of $(Ti,Dy)_xO_y$ samples prepared by post-deposition thermal oxidation anneals is found in Table 4.6.

Since oxygen diffusion is a thermally activated process, we anticipate that the extent of oxidation of the films is a strong function of the temperature of the oxidation anneal. In Figure 4.12, we plot the median inferred dielectric constant of oxide films as a function of the temperature of the oxidation anneal. The films

Table 4.6: Post-deposition oxidation samples of $(Ti,Dy)_xO_y$

Sample	Sputter time (s)	Oxidation time (min)	Oxidation temperature (°C)	Thickness (nm)
07h14	30	20	300	62
07h13	30	20	350	62
07h11	30	20	375	62
07h08	30	20	400	62
07h09	30	20	450	62
07h10	30	20	500	62
07h12	30	20	550	62

were sputtered for 30 seconds at 100 W RF power, heated in vacuum to temperature, and finally exposed to 1 Torr molecular oxygen (O_2) for 20 minutes. The median is taken of non-shorted capacitors (100 to 150 capacitors) and measured at 10 kHz, while the error bars represent one standard deviation. Also in Figure 4.12, we plot the loss tangent of the dielectric constant, $\tan\delta = \varepsilon''/\varepsilon'$, for the same samples. At temperatures below 350 °C (not shown), there is insufficient oxidation to form good capacitors. The median dielectric constant is 300, while the loss tangent is 2.8. Very few capacitors were found to be short-circuited in the AC capacitance measurement with V_{ac}=200 mV, though breakdown voltages were < 1 V (electric fields < 0.2 MV/cm).

As the oxidation temperature increases, the measured dielectric constant and the loss tangent both decrease. From 350 °C to 450 °C, the dielectric constant is ~50 or greater, while the loss tangent is ~0.5 –unacceptably high. We attribute these high dielectric constants to incomplete oxidation of the film and speculate

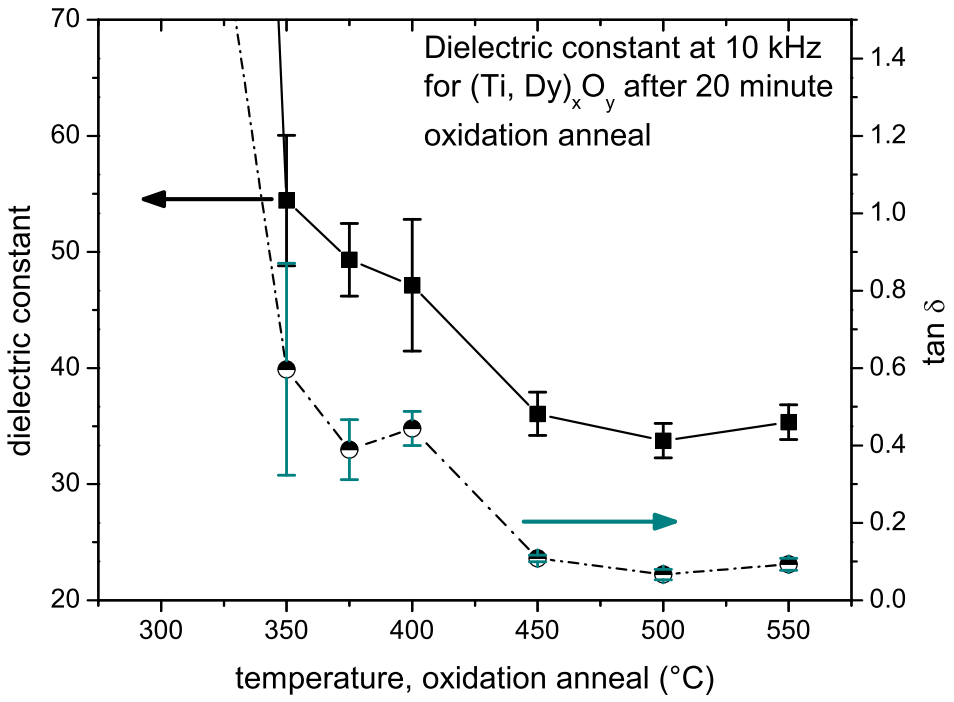

Figure 4.12: The median dielectric constant and loss tangent for thermally oxidized (Ti, Dy)$_x$O$_y$ as a function of the temperature of the oxidation anneal. The anneal time for all samples were 20 minutes. The measurement frequency was 10 kHz. The error bars represent a standard deviation. Samples 07h08-07h14.

that oxygen vacancies can act as polarization or hopping sites.

At temperatures of 450 °C and above, the dielectric constant is ~35, but the loss tangent remains high ~0.1. The dielectric constant and loss tangent no longer decrease with increased temperature of the oxidation anneal, indicating a defect polarization that cannot be healed within the range of anneal temperatures investigated. The dielectric constant is 40 % greater than the dielectric constant of reactively sputtered (Ti,Dy)$_x$O$_y$. As yet, we have not identified a de-

tailed mechanism for this addition to the polarization, but discuss possibilities in the following sections.

We note that the terminology 'dielectric constant' is somewhat of a misnomer when referring to the thermally oxidized films presented here since we are not measuring the polarization of atomic bonds and electron orbitals, but rather additive defect polarization mechanism.

As discussed elsewhere in this thesis, the dispersion of the dielectric measurements can elucidate an enhanced low frequency polarization. In Figure 4.13, we plot the dispersion of the normalized capacitance and loss tangent from 100 Hz to 1 MHz. At each oxidation temperature, the capacitance is normalized to the capacitance at 1 MHz. As expected from the interpretation of partial oxidation for temperatures < 450 °C, there is high dispersion (100s of %) in the polarization; the dispersion decreases with increasing temperature of the oxidation anneal, as expected for an increasingly oxidized film. The dispersion of "fully" oxidized films (those oxidized at 450 °C or greater) is still substantial (>40%), however, and supports the interpretation that there is still an additive defect polarization active.

The variation of the loss tangent with frequency reinforces our interpretation of a transition that occurs between samples oxidized at 400 °C and at 450 °C. While the loss tangent for lower temperature anneals peaks at 5 kHz, the loss tangent for the higher temperature anneals takes place at 1 kHz or less. The peak in the loss tangent is related to the peak in the imaginary (lossy) part of the dielectric constant, ε'', at still lower frequencies; the peak in ε'' defines a characteristic frequency of the polarization mechanism. The two distinct behaviors of the loss tangent with frequency indicate two distinct polarization mechanisms

at play in the two annealing regimes.

In addition to the decreased dielectric constant and loss tangent, increases in oxidation temperature also decrease the number of defects that give rise to shorted capacitors. Figure 4.14 presents maps of raw capacitance data at 10 kHz at increasing temperatures of the oxidation anneal. Shorts or 'bad' capacitors are represented by light blue or black, respectively, and their density is observed to decrease significantly with increasing temperature of the oxidation anneal, indicating that there may be some healing of defects during high temperature annealing.

We note that the characteristic temperatures recorded here are those required for the given metal deposition and the fixed 20 minute anneal time. As the thickness of the deposited metal changes, the oxidation parameters will certainly change. Given the Arrhenius-type activation of oxygen diffusion, oxidation depends most strongly on temperature, $e^{-\Delta H/kT}$, but is likely to depend weakly on oxidation time and film thickness.

Comparison of reactively sputtered (Ti,Dy)$_x$O$_y$ to thermally oxidized (Ti,Dy)$_x$O$_y$

In Figure 4.15, we compare the leakage current density in a reactively sputtered film deposited on an unheated substrate with that in a thermally oxidized film. While the breakdown fields are very comparable, the leakage current behavior at lower fields is noticeably different. Above 1 MV/cm, there is significantly higher leakage through the thermally oxidized sample. The current density is sublogarithmic, and its functional form is very well fit by either a

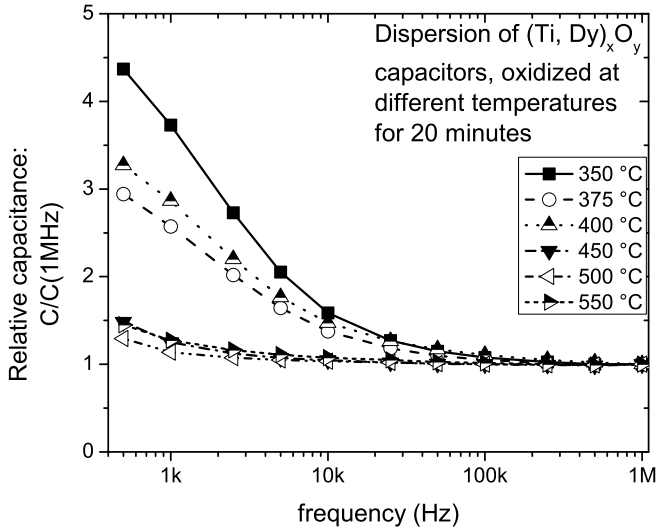

(a) Normalized capacitance

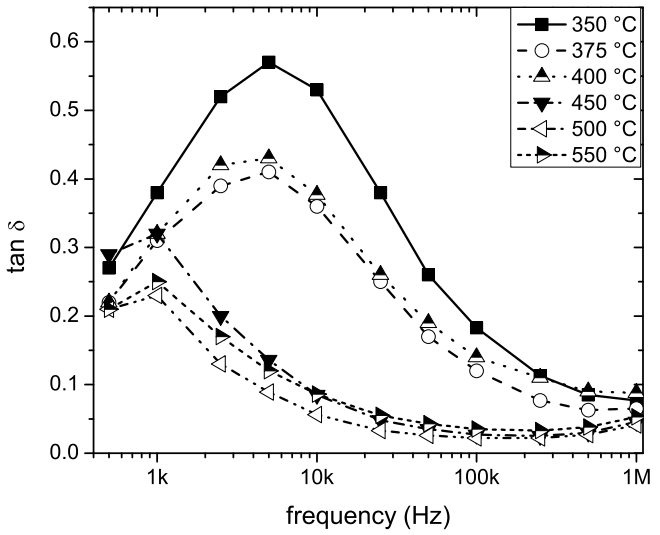

(b) Loss tangent

Figure 4.13: Dispersion of capacitance and dissipation measurements in thermally oxidized TiDyO. Samples 07h08-07h14.

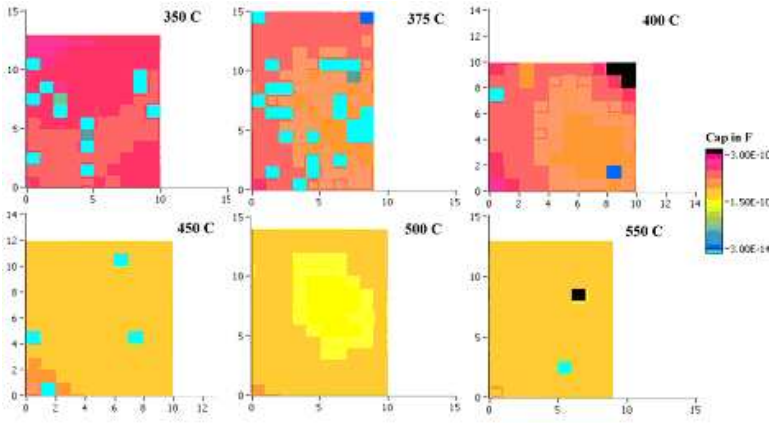

Figure 4.14: Annealing out shorts. Courtesy John A. Hevey [56]

Schottky or Frenkel-Poole leakage model. With identical platinum electrodes on reactively sputtered and thermally oxidized samples, there is little justification for choosing the Schottky model in which leakage current is limited by emission at an electrode. Frenkel-Poole leakage currents, however, are mediated by defect states throughout the oxide, which we have argued are substantially different in density and type in thermally oxidized films than reactively sputtered films. We suggest that some of the defect states that contribute to the AC polarization mechanism indicated in capacitance measurements may also contribute to a small DC leakage current at moderate electric fields.

To complete the comparison between the reactively sputtered oxide and the thermally oxidized one, we compare the distribution of supported areal charge density $Q_{\max}/A = CV_{\text{br}}/A$. Figure 4.16 shows the cumulative probability of maximum areal charge density for capacitors formed by thermal oxidation at temperatures of 450, 500, and 500 °C and reactively sputtering on platinum and nickel base electrodes. We notice that the reactively sputtered on nickel and thermally oxidized $(\text{Ti,Dy})_x\text{O}_y$ have very comparable maximum areal charge den-

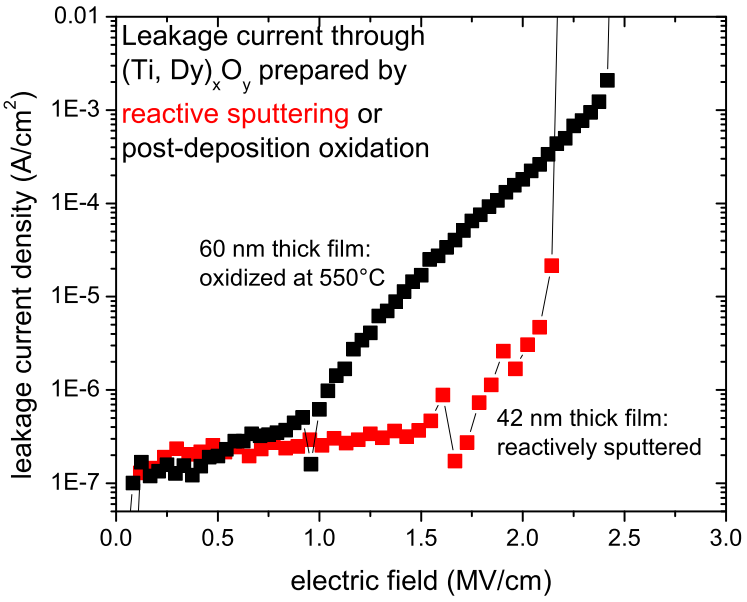

Figure 4.15: Leakage current density versus nominal field for reactively sputtered and thermally oxidized $(Ti,Dy)_xO_y$

sities at the 90th percentile, while at the 50th percentile, the thermally oxidized $(Ti,Dy)_xO_y$ is higher by ~30%, an enhancement comparable to the enhancement in the dielectric constant. Strikingly, the platinum base electrode does not support nearly as high quality dielectric as the nickel base electrode. Forty percent of the capacitors measured on the platinum base electrode were shorts; the bulk of the remainder supported areal charge densities of 2.5-4 $\mu C/cm^2$.

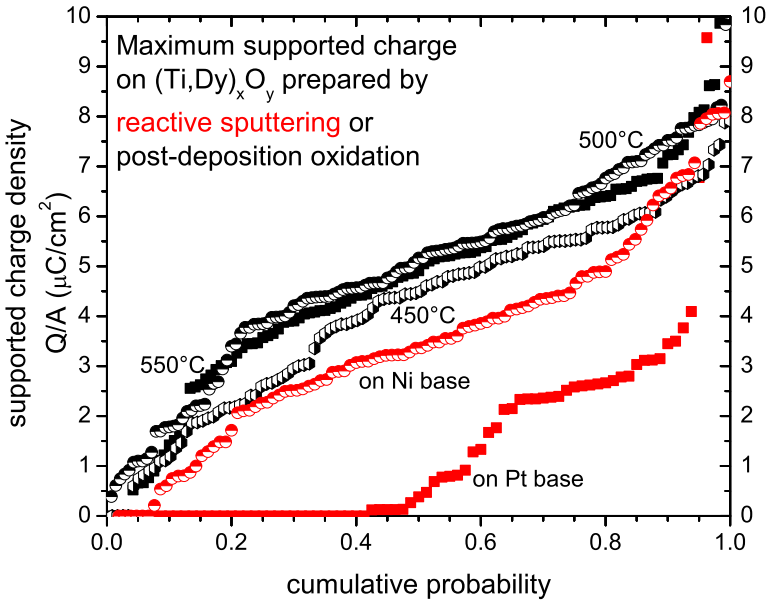

Figure 4.16: The maximum areal charge density, $Q_{\max}/A = CV_{\mathrm{br}}/A$, for reactively sputtered and thermally oxidized $(Ti,Dy)_xO_y$

Defect polarization in high temperature (T>450 °C) thermally oxidized $(Ti,Dy)_xO_y$

There are a few possibilities for the additive polarization mechanism observed in oxidized $(Ti,Dy)_xO_y$ formed with annealing temperatures >450 °C.

Defect polarizations are possible at or within inhomogeneities in dielectric materials, as charge carriers find hopping sites along unsatisfied bonds [48]. A potential inhomogeneity in these films is due to phase segregation during annealing. Though titanium and dysprosium form two compound oxides, Dy_2TiO_5 and $Dy_2Ti_2O_7$, these compounds have a composition far different from that of our deposited metal cations: 77:23 Ti:Dy, and phase segregation on crys-

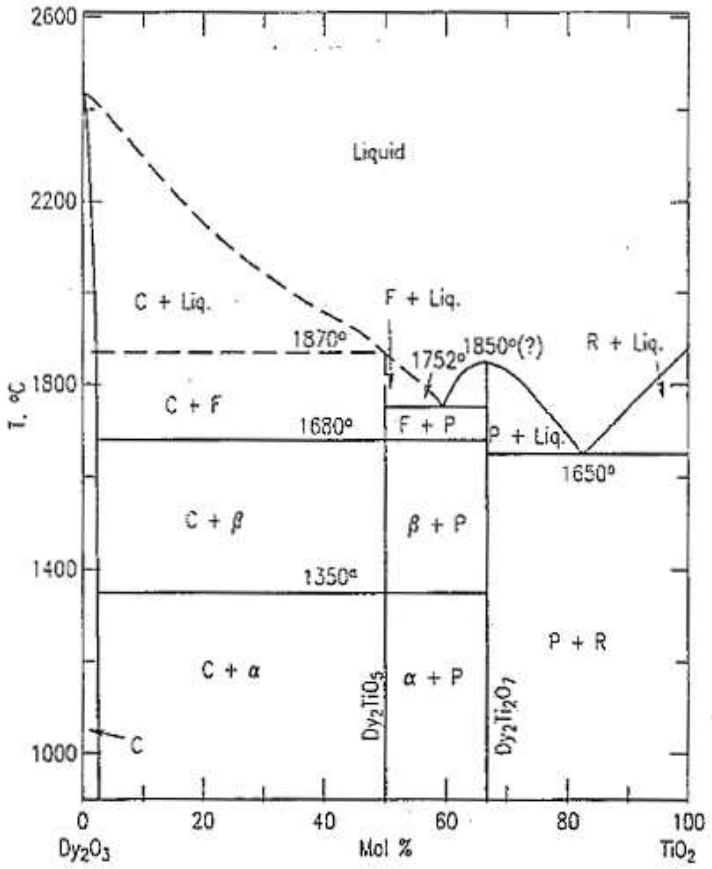

Figure 4.17: Bulk equilibrium phase diagram for TiO_2-Dy_2O_3. From Reference [94]

tallization is possible, presumably into some combination of TiO_2 and $Dy_2Ti_2O_7$. Figure 4.17 is a reproduction of the bulk equilibrium TiO_2-Dy_2O_3 phase diagram.

In the thermally oxidized samples, metal deposition occurs at room temperature, yielding an intimately mixed metal which is then heated in vacuum to the desired temperature over 30 minutes to an hour. In addition to oxide immiscibility, therefore, we must additionally consider metal immiscibility. The titanium-dysprosium phase diagram from Reference [94] is reproduced in Fig-

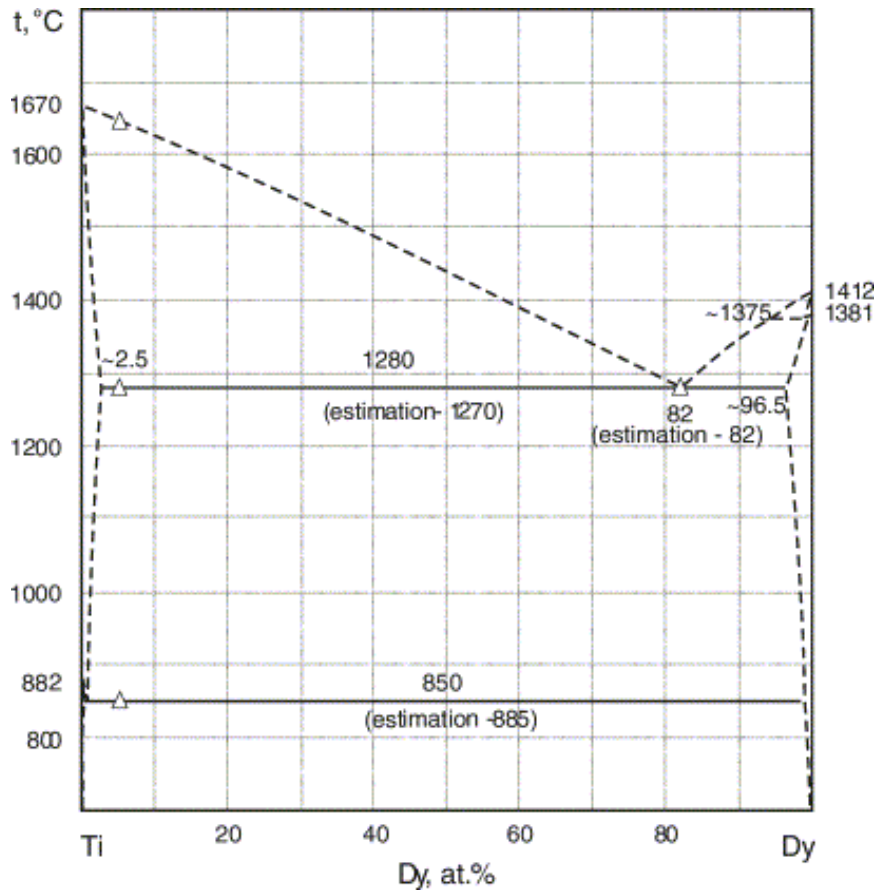

Figure 4.18: Phase diagram for Titanium-Dysprosium. From Reference [94]

ure 4.18 and reveals almost complete solid insolubility at all temperatures.

Phase segregation of the oxides or the metals may occur, then, at annealing temperatures of sufficient thermal energy for significant diffusion; this requires a homologous temperature $T/T_m > 0.5$ - 0.7. Melting temperatures and homologous temperatures at 500 °C are given for the metals and metal oxides in Table 4.7, and we find that the homologous temperatures are too low for significant bulk diffusion and crystal growth to occur.

Analysis of x-ray diffraction on the sample thermally oxidized at 550 °C is

Table 4.7: Melting temperatures and homologous temperatures at 500 °C of Ti and Dy metals, and their own and mixed oxides

Material	Melting temperature (°C)	Homologous temperature, T/T_m at T = 500 °C
Ti	1668	0.392
Dy	1407	0.460
70:30 Ti:Dy	1540	0.460
TiO_2 (anatase)	transforms to rutile	
TiO_2 (rutile)	1843	0.365
Dy_2O_3	2408	0.288
Dy_2TiO_5	1870	0.361
$Dy_2Ti_2O_5$	1850	0.364

complicated by diffraction off the platinum electrodes (60 nm total thickness); however, broad rutile TiO_2 (pdf 21-1276) peaks are observed, as well as another unidentified phase. In a separate experiment to probe possible metal segregation prior to oxidation, we deposited the Ti-Dy metal alloy on bare silicon and anneal at 500 °C in vacuum (sample 08h08). In this case, however, $TiSi_2$ (pdf 35-0785) and $DySi_2$ (pdf 50-0746) are the predominant phases formed.

Oxide phase segregation can be additionally investigated on reactively sputtered $(Ti,Dy)_xO_y$. Crystallization in reactively sputtered $(Ti,Dy)_xO_y$ is observed after one hour anneals in air at 850 °C (sample 05h63) and 950 °C (sample 05h61). Two crystal phases are formed: rutile TiO_2 (pdf 21-1276) and the pyrochlore phase $Dy_2Ti_2O_7$ (pdf 17-0453). No dielectric measurements were made on these samples since they were sputtered on bare silicon. Crystallization was not ob-

served in the film reactively sputtered on a substrate at 365 °C.

We note that crystallization itself does not lead to an additive polarization mechanism. In Chapter 3, we considered reactively sputtered $Zr_{0.2}Sn_{0.2}Ti_{0.6}O_2$ on substrates heated to 500 °C. The loss tangents in polycrystalline samples remained low <0.02 and comparable to that of the amorphous phase. Rather, an additive polarization is observed when crystallization is accompanied by phase segregation and the introduction of inhomogeneities at phase boundaries.

Finally, the polarization we observe in dielectric measurements changes very little between anneals at 450 and 550 °C. Polarization due to crystal growth and the accompanying phase segregation, however, should increase with increasing temperature, since both are strong functions of temperature. We conclude that though small crystallites form in the $(Ti,Dy)_xO_y$ and possibly in the metal alloy prior to oxidation, they are not the main source of the additive polarization observed in thermally oxidized $(Ti,Dy)_xO_y$.

Another likely source of inhomogeneities in the oxide film is the structure of the metal film on deposition. Depositions of metal thin films often suffer from atomic shadowing and the resultant columnar growth structures; in between and surrounding the metal columns are voids or boundaries of low density. Depending on the relative density of the oxides and the metals, the oxidation process may fill in these voids and eliminate the low density inhomogeneities (and the associated diffusion or drift of charge carriers), or it may aggravate the effect. We know very little about the non-equilibrium as-deposited metal/metal oxide film, and a cross-sectional HRTEM study could shed light on this possibility. However, we may make a limited analysis by assuming the equilibrium densities for each constituent material.

Table 4.8: Equilibrium densities of Ti and Dy metals, and their own and mixed oxides. The mixed oxides are less common; results given here are calculated from x-ray diffraction results *a*: PDF 40-0874, cubic; *b*: PDF 34-1445, hexagonal; *c*: PDF 20-1025, orthorhombic; *d*: PDF 17-0453, cubic.

Material	Density (g/cm^3)	Molar density (mol metal/cm^3)
Ti	4.507	0.941
TiO_2 (anatase)	3.880	0.486
TiO_2 (rutile)	4.230	0.529
Dy	8.551	0.528
Dy_2O_3	7.800	0.419
Dy_2TiO_5	7.22^a, 5.598^b, 1.721^c	0.048^a, 0.037^b, 0.011^c
$Dy_2Ti_2O_7$	6.856^d	0.051^d

The densities of Ti, Dy, and their oxides and mixed oxides, in equilibrium, crystalline form are shown in Table 4.8. The density of Ti atoms in the metallic Ti is much higher than in the unary oxide, implying that oxidation can compensate for a low density metal and bring the film closer to its theoretical full density. A fully dense metal film will be put in compression by oxidation. This is true in a more limited sense for dysprosium, since the density of Dy atoms in the metal is only slightly higher than in the oxide.

4.5 Conclusions

In this chapter, we have discussed many of the deposition and processing controls available in sputter deposition of dielectric oxides in the specific context of $(Ti,Dy)_xO_y$. We find that dysprosium substituted TiO_2 is a high quality dielectric when prepared by reactive sputtering with $\varepsilon_r = 25$ and low leakage and low dispersion with frequency. The reactive sputtering process must be optimized for the desired elemental composition and density while controlling the intrinsic stress and damage done by energetic arriving species. The base electrode metal or semiconductor must also be chosen with care for good adhesion to the oxide and minimal induced serial parasitic capacitance.

We investigated the preparation of the same material by *in situ* thermal oxidation of the deposited metal. Full oxidation of a 62 nm film occurs after an oxidation anneal at temperatures > 450 °C in 1 Torr molecular oxygen, though lower thermal budgets may be possible for thinner metal films. $(Ti,Dy)_xO_y$ prepared here using thermal oxidation suffers from an additive defect polarization, which manifests itself in high dispersion of the dielectric constant with frequency, substantial loss tangents, and increased leakage currents at moderate electric fields. These defects must be eliminated prior to integration of thermally oxidized $(Ti,Dy)_xO_y$ in device structures.

CHAPTER 5

EFFECT OF ION BOMBARDMENT IN ON-AXIS AND 90° OFF-AXIS REACTIVE SPUTTER DEPOSITIONS (TANTALUM OXIDE)

This chapter is adapted from S. C. Barron, M. M. Noginov, D. Werder, L. F. Scheenmeyer, and R. B. van Dover: "Dielectric response and ion bombardment in oblique sputtering of the thin film oxide dielectric Ta_2O_5," to appear.

Maxim Noginov contributed to the work reported in this chapter.

In Chapter 6, we describe a survey of composition space using combinatorial samples prepared by deposition from 90° off-axis sputter sources. To demonstrate the validity of this deposition technique for preparing high quality dielectric oxides, we undertook the following investigation of the dielectric response of the model oxide dielectric Ta_2O_5, prepared by 90° off-axis reactive sputtering.

5.1 Abstract

We describe the deposition of insulating tantalum oxide thin films using 90° off-axis reactive sputtering which allows us to explore the growth of oxides under conditions of low ion bombardment. Films of Ta_2O_5 prepared using off-axis sputtering have low frequency dielectric constants as high as ε ~300 when deposited on an unbiased substrate. The loss tangent is high, $\tan\delta > 0.5$, and has a pronounced frequency dependence. Deposition of the film off-axis with sufficient applied rf bias to the substrate (negative bias > -70 V) recovers the on-axis properties typical of Ta_2O_5, e.g. ε ~22 and $\tan\delta \sim 0.02$. The recovery of normal dielectric behavior is attributed to the ion bombardment of the growing

film under substrate bias, similar to on-axis depositions but absent from the unbiased off-axis films. We suggest that insufficiently bombarded films develop a Maxwell-Wagner type polarization along columnar voids. The void structure and the associated dielectric response vary with distance from the sputtering source due to variations in ion density and angle from the sputtering source. A similar dielectric response is observed in depositions on on-axis substrates as a function of angle from the center of the sputtering target. Our results suggest that ion bombardment is necessary for good quality sputtered dielectric films but that a controlled Ar^+ flux is essentially equivalent to the uncontrolled O_2-/O^{2-} flux of on-axis reactive sputtering.

5.2 Introduction

Sputtering is an important technique for the commercial and research deposition of high quality metal oxide thin films. In manufacturing environments, film uniformity is assured by employing sputtering targets much larger than the substrates and elaborate automated substrate rotations. For laboratory research in which targets are typically comparable to or smaller than the size of the substrate, however, film uniformity can become an issue, especially for short substrate to target distances.

Similar effects may be seen in films deposited from oblique sources, in which the substrate is positioned parallel to the sputter gun's central axis. Such sputtering geometries are used extensively in laboratory settings to create a gradient in chemical composition in oxide films by employing several off-axis sputter guns [30, 95]. The present study highlights the film quality of dielectric oxides

deposited from oblique sources in comparison to the quality of films produced by deposition in the normal geometry, both directly under the target and at an angle offset from the sputter gun's central axis.

One feature that distinguishes depositions from oblique sources from normal depositions is the decreased bombardment of the substrate with energetic species. In reactive radio frequency (rf) sputtering on a substrate normal to the sputter gun axis, bombarding species include target atoms, neutral argon atoms reflected from the target, and especially O_2^-/O^{2-} ions accelerated in the electric field. On an off-axis substrate, bombardment by all these species is decreased. Applying an electrical bias to the substrate has been found to increase bombardment by Ar^+ ions [96].

Sputtering of dielectrics is an important research laboratory technique for the investigation of new candidate dielectric materials. Van Dover et al. pioneered off-axis reactive sputtering of composition spread searches for advanced dielectrics [97] and identified $Zr_{0.2}Sn_{0.2}Ti_{0.6}O_2$ as a candidate dielectric supporting record areal charge density [62]. Magnetron sputtering of an ultrathin metal film and in-situ oxidation using an active oxygen species (ozone, atomic oxygen, e.g.) has been demonstrated by several groups to yield high quality dielectric oxides for integrated circuit technologies [20, 21, 86, 98]. Oxide dielectric films can also be deposited by sputtering from a ceramic oxide target [99, 100, 101], though anomalously high dielectric constants for well known materials such as Ta_2O_5 have been attributed to quenched-in vacancies at high sputtering pressures [101].

Several studies [60] have employed substrate biasing to increase ion bombardment of the film in on-axis depositions. Recent investigations [31, 102]

have applied substrate biasing specifically to dielectric oxides prepared by on-axis sputtering; they find that low levels of bombardment improve the dielectric properties of sputtered oxide films, largely by increasing the density, and thereby, the dielectric constant of the film. At higher levels, bombardment may damage the film. Densification due to substrate biasing is also observed in oblique angle deposition of metal films [95].

In this paper, we investigate the effects of substrate bias on dielectric measurements of Ta_2O_5 sputter-deposited from an oblique source. We find a defect-mediated polarization mechanism that masks the intrinsic Ta_2O_5 dielectric properties and demonstrate the use of substrate biasing to recover the intrinsic properties. For this study, we chose a well-behaved and well-characterized oxide dielectric: Ta_2O_5. It is profitable to understand these mechanisms in a model system such as Ta_2O_5 so that they may be recognized and eliminated in the characterization of less well-understood dielectrics.

5.3 Experimental Methods

Tantalum oxide films were deposited by reactive RF sputtering from a metallic Ta target using a U. S. Gun 2-inch diameter magnetron sputter gun. In this deposition process, the metallic target self-biases negatively due to the greater mobility of electrons compared to Ar^+ ions at radio frequencies [33]. In the resulting electric field, positively charged argon ions are accelerated toward the target and sputter tantalum atoms and TaO dimers, while negatively charged oxygen ions are accelerated away from the target. Additionally, neutral argon is reflected off the target. As pictured in Figure 5.1, there is uncontrolled reflected

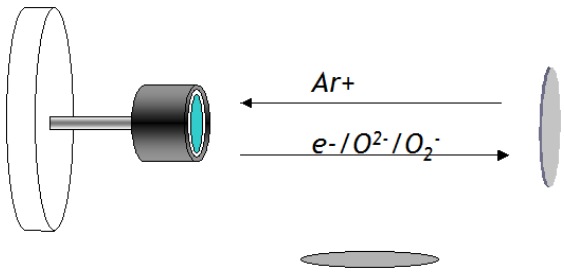

Figure 5.1: Schematic of uncontrolled electron and oxygen ion bombardment of an on-axis substrate and lack of bombardment on the 90° off-axis substrate.

Ar and O_2-/O^{2-} ion bombardment of the substrate within the target's line of sight ("on-axis substrate") and much less bombardment off the central gun axis ("off-axis substrates"). In this paper, we report primarily on films deposited on 90° off-axis substrates; to achieve this geometry, the substrate plane is oriented parallel to the axis of the gun and offset 33 mm below the center of the target. The closest edge of the substrate is about 17 mm from the plane of the sputter target.

For off-axis depositions, a relatively high sputtering pressure of 30 mT (typically 20% O_2 in Ar) ensures effective thermalization of the oxygen ions and Ta and TaO dimers ejected from the target. The sputter gun was operated under power control at 100 W rf, yielding a deposition rate of 0.6 to 1.2 /s (Sample 07f91-2). The films are 30 to 80 nm thick. Prior to deposition, the system was turbo-pumped to 4×10^{-6} Torr base pressure.

During some depositions, an RF bias was applied through a matching network and blocking capacitor to the substrate holder during growth, using an independent power supply to increase ion bombardment of the substrate. In response, the substrate self-biases negatively, in an analogous manner to the

target self-bias. The substrate self-bias results in argon ion (Ar^+) bombardment, similar again to the sputtering mechanism of the target. However, this is not a self-sustaining process due to the lack of magnetic support of the plasma above the substrate, and so it is emphasized that the extra bombardment depends on the presence of Ar^+ ions created in the plasma associated with the target.

The power to substrate is deliberately limited to twenty percent of the power applied to the target, in this case, 5-20 Watt (corresponding to measured dc self-biases of -33 to -110 V). At this power level, there should be little sputtering of the deposited film; instead ion bombardment is expected to densify or even crystallize the film by increasing the surface mobility of arriving species.

In this experiment, the substrate bias is power controlled with a matching network tuned to maximize the dc self-bias voltage. It is worth noting that ion bombardment depends on both the flux of ions (current) and the dc voltage across which the ions are accelerated. The ion flux increases with the square root of the substrate bias voltage [38]. The effects of ion bombardment, therefore, diminish rapidly at low bias voltages. Additionally, increases in bias voltage result in increases in both the ion flux and the average ion energy, such that these effects are not independently investigated by this technique [103].

The dc self-bias was about -33 V at 5 W, -51 V at 10 W, and -70 V at 15 W, though these values depend on the specific values of the reactances in the rf power impedance matching circuit.

We also note that voltages in excess of the sputter threshold (typically 10 eV; for Ar^+ sputtering Ta, 30 eV) may lead to resputtering of the film. This possibility is still under investigation and is further discussed in Section 5.6.1 and in the

case of co-sputtered binary TaO_x-GeO_x films in Chapter 6.

The substrate temperature may also increase with ion bombardment during deposition, but we find that the temperature increase is limited to 10-20 degrees above the substrate's initial (ambient) temperature. This temperature increase is insufficient to change the film microstructure or nanostructure.

For comparison, films were also deposited on unbiased substrates oriented perpendicular to the gun axis (i.e. "on-axis"). These substrates were three inches in diameter and positioned 5 cm in front of a 2-inch target; the target power was 75 W rf in a 10 mT sputtering gas of 20% O_2 in Ar. The sputtering parameters were chosen to give a similar deposition rate (0.8-1 /s) to the off-axis deposited films. Dielectric properties were evaluated in regions of the film that ranged from directly on-axis to as much as 35° off-axis.

It is important to note that oxygen ion bombardment in on-axis depositions is not independently controlled; rather it depends on the other deposition parameters: sputtering gas pressure, oxygen partial pressure, distance between the target and the substrate, and power to the target. By contrast, in our configuration for 90° off-axis deposition, argon ion bombardment can be independently tuned by the rf bias power applied to the substrate. The main effect of the bias is to increase Ar^+ ion bombardment; that is, the arrival rate of Ta or TaO from the target and the oxygen content of the film are not affected by the bias.

We characterize the dielectric properties using a metal-insulator-metal (MIM) capacitor structure. Fabrication of the alternative metal-oxide-semiconductor structure on silicon in the presence of active oxygen would incorporate an adventitious interfacial SiO_2 that would complicate evaluation of

Ta_2O_5 dielectric properties [32, 83, 84]. Our experiments on MIM capacitors, in contrast, focus on the effect of different processing parameters on the Ta_2O_5 film morphology. Substrates were pre-coated with an evaporated platinum or sputtered TiN base electrodes before oxide deposition. Top electrodes of platinum or silver were evaporated through a 0.2 mm shadow mask to complete the parallel plate MIM capacitors.

An LCR meter (HP 4284) and commercial probe station were used to evaluate capacitance and loss tangent at 100 mV_{ac} over 40 Hz-1 MHz. A natural thickness and deposition rate gradient is found along the length of the sample, courtesy of the geometry of the off-axis deposition system. The thickness of the dielectric was mapped using a reflectometer, and confirmed at selected points by spectroscopic ellipsometry. Void structure was elucidated with bright field transmission electron microscopy, and the surface roughness is evaluated by tapping mode atomic force microscopy.

5.4 Results and Discussion

5.4.1 Dielectric response: off-axis deposition

The evaluation of a dielectric material relies in part on an accurate measurement of its dielectric constant. For most metal oxides, the intrinsic polarizabilities (ionic and electronic) lead to a dielectric constant ε ~10 to 30 which is frequency independent up to 1 THz [54]. For high quality amorphous Ta_2O_5 films, $\varepsilon \sim \varepsilon' \sim$ 22-26 [104]. Additional polarization mechanisms and interfacial effects can also contribute to the observed dielectric constant and can mask the intrin-

sic material properties one hopes to evaluate. Dispersion (the dependence of on frequency) is a useful diagnostic measurement that can provide information about the polarization mechanisms active in a dielectric. Any dispersion in the dielectric constant in the 40 Hz to 1 MHz range is undesirable for most applications and generally due to a nonstandard or defect polarization mechanism. The raw measured electrical quantities are the capacitance and the dissipation. From capacitance and an optical measurement of thickness, we calculate the dielectric constant, ε'. The dissipation factor, or loss tangent, is the ratio of the imaginary (lossy) part of the dielectric constant to the real part: $\tan\delta = \varepsilon''/\varepsilon'$. Dissipations above ~0.05, e.g., are inconsistent with a high quality thin film dielectric.

In Figure 5.2, we plot the dispersion of the dielectric constant and dissipation factor across from 40 Hz to 1 MHz for samples deposited off axis with and without substrate bias. This data is taken from representative $Pt/Ta_2O_5/Pt$ capacitors prepared on regions of the film at 25 mm from the plane of the sputtering target during deposition. At this distance, the measured dielectric constant of the off-axis films deposited with a 5-15 W bias is ~22. The dissipation factor for these samples is low, $\tan\delta \sim 0.02$. The frequency dependence over the range of 40 Hz to 1 MHz is negligible; the small variation in observed loss and capacitance is attributed to experimental artifacts associated with parasitic reactances in the leads of the probing system. These values are in agreement with literature values for conventional (e.g., on-axis sputtered or CVD) Ta_2O_5.

In contrast, the films deposited without substrate bias have a highly dispersive behavior: the dielectric constant at 40 Hz is 330 and the loss tangent is very high, $\tan\delta > 1.0$, and both decrease rapidly with increasing frequency. At the highest frequencies, the dielectric constant approaches that of the biased Ta_2O_5,

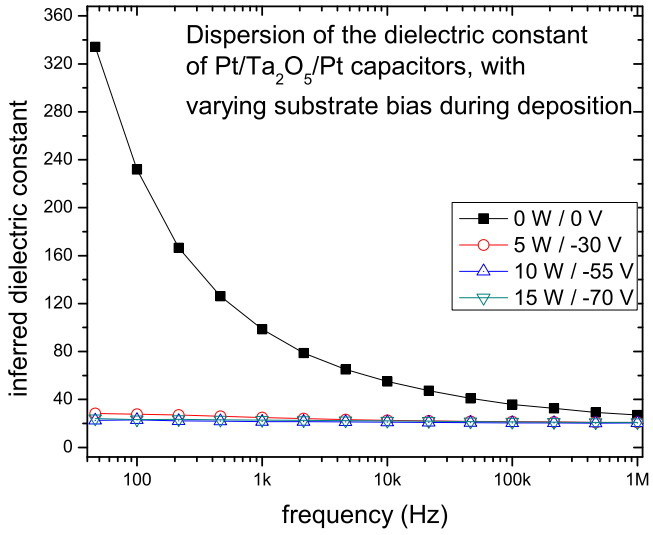

(a) Dielectric constant

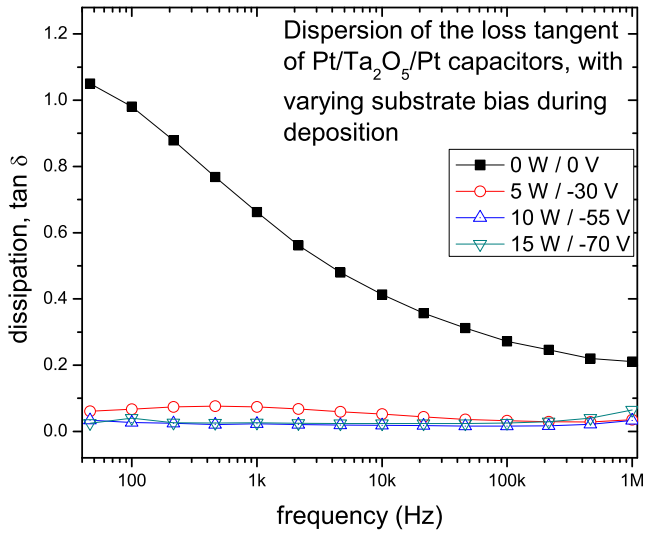

(b) Loss tangent

Figure 5.2: Dielectric response of Ta_2O_5 capacitors deposited off-axis with varying substrate biases. (a) Dielectric constant. (b) Loss tangent. These capacitors lie 25 mm from the target plane and are 55 nm thick. Samples 08f28 5 W; 07f131 10 W; 07f133 15 W. 07f135 0 W.

indicating the low frequency polarization response is frozen out at ~1 MHz such that the only contribution to the material's response is that of the electronic and ionic polarizabilities noted earlier.

5.4.2 Material structure: off-axis depositions

To elucidate the structural basis for the observed low frequency, lossy polarization in films grown under conditions of very low bombardment, we performed cross-sectional and plan view TEM. The TEM micrographs in Figure 5.3(no bias) reveal the presence of voids in the off-axis film without bias that are absent in an off-axis biased film. The cross-sectional image suggests that the voids are columnar and oriented parallel to the growth direction. Their depth is estimated to be 10 nm and their width 2.5 nm.

Figure 5.3(bias) shows TEM micrographs of a film deposited off-axis with a 10 W (-51 V) substrate bias. These reveal a dense amorphous film with no discernable voids. The TEM images in Figures 5.3(no bias) and 5.3(bias) were obtained from samples deposited on 90° off-axis substrates from the region of the substrate that was at a distance of 27 mm from the plane of the sputtering target during deposition.

We associate the low frequency polarization observed in Figure 5.2, therefore, with the void structure in insufficiently bombarded films, while bombarded films, which have no voids, demonstrate the expected dielectric properties of intrinsic Ta_2O_5.

Columnar voids are not unexpected in an off-axis deposition. The occur-

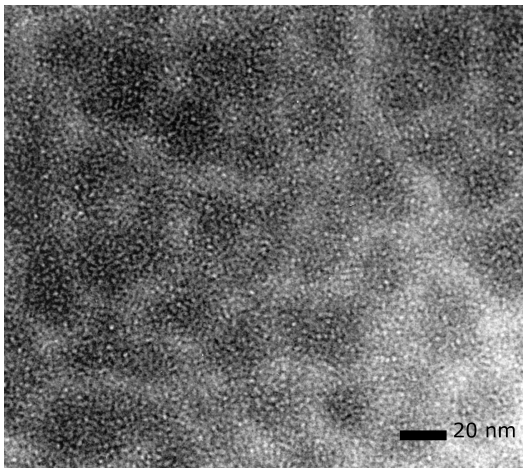

(a) Plane view TEM of biased film

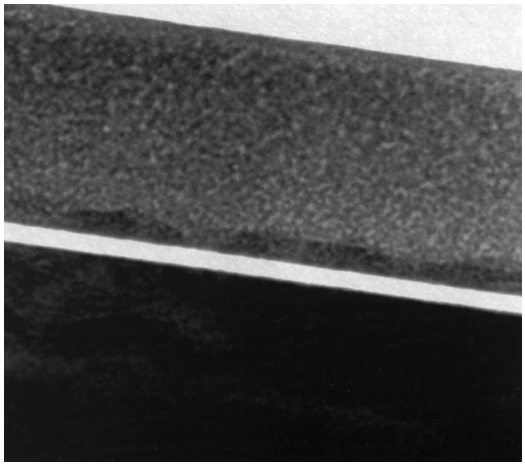

(b) Cross sectional TEM of biased film

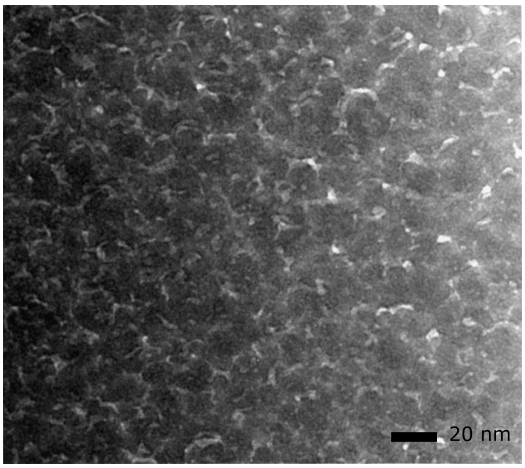

(c) Plane view TEM of unbiased film

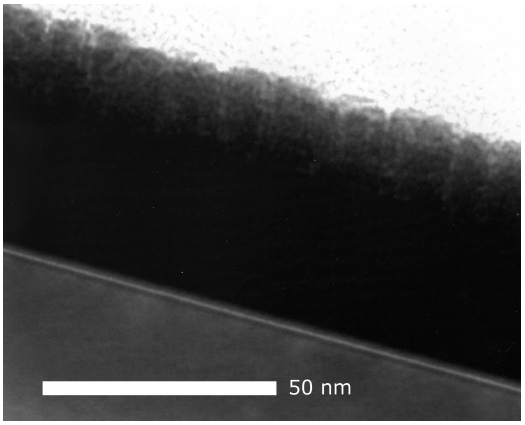

(d) Cross sectional TEM of unbiased film

Figure 5.3: TEM images of Ta_2O_5 deposited off-axis, with a substrate bias of 10 W (-50 V) and without substrate bias. Sample 98f36, 98f38. Courtesy Don Werder, formerly of Bell Labs, currently of Los Alamos National Laboratory.

rence of columnar voids is attributed to a low surface mobility compared to the rate of deposition [105, 106]. They have been reported in depositions from oblique sources with limited surface diffusion [95, 107, 108, 109, 110] and manifest themselves as tensile stresses in the film [106, 111].

5.4.3 Distance from sputtering source: off-axis depositions

The effectiveness of substrate biasing at eliminating the void structure is strongly dependent on the energy and density of ions in the plasma. The plasma is associated with the magnetron sputter gun and therefore varies spatially within the sputtering chamber. Thus, the dielectric response of Figure 5.2 is not constant across the film, but rather varies with distance from the sputtering source. We plot in Figure 5.4, the inferred dielectric constant at several frequencies for $Pt/Ta_2O_5/Pt$ capacitors at increasing distances from the sputtering target; this is done for films with 0, 5, 10, and 15 W substrate biases (0, -33, -50, -70 V substrate voltages).

For capacitors formed with the unbiased Ta_2O_5 (Figure 5.4), dispersion and are high close to the sputter gun, reaching a peak at 2.2 cm from the target. This suggests that there may be some bombardment and densification in the area closest to the target (< 2.2 cm) due to reflected Ar neutrals and O_2-/O^{2-} bombardment. Beyond 2.2 cm, dispersion and low frequency ε remain high but decrease with increasing distance from the sputtering source; at 460 Hz, ε decreases from 140 at 2.2 cm to 60 at 6.5 cm. As stated previously, the high ε and dispersion are attributed to a void-mediated low frequency polarization. We expect the structure of the voids (density, size, e.g.) to change with distance

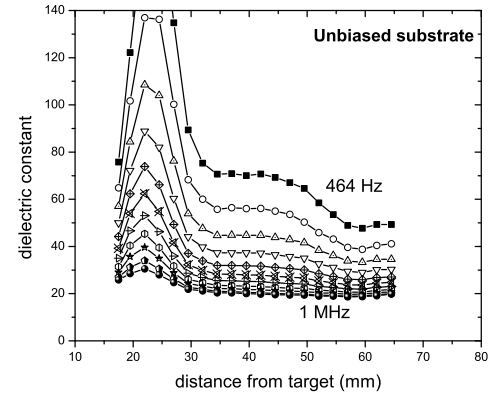

(a) Substrate bias = 0 W

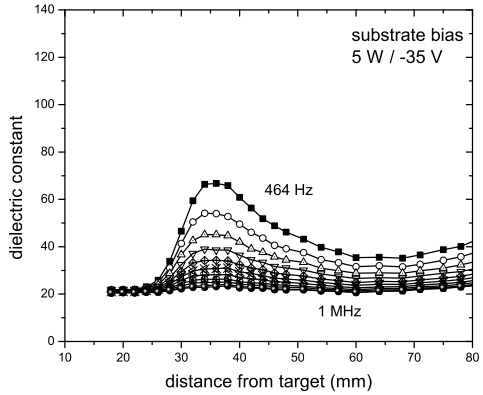

(b) Substrate bias = 5 W / -30 V

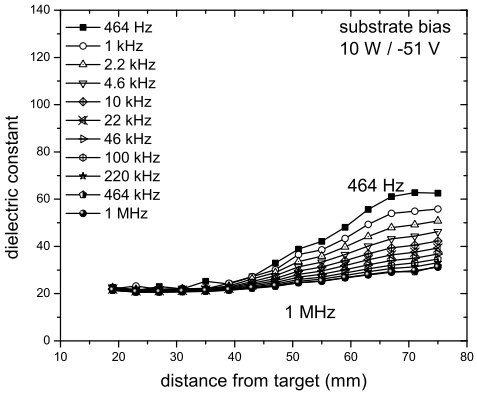

(c) Substrate bias = 10 W / -50 V

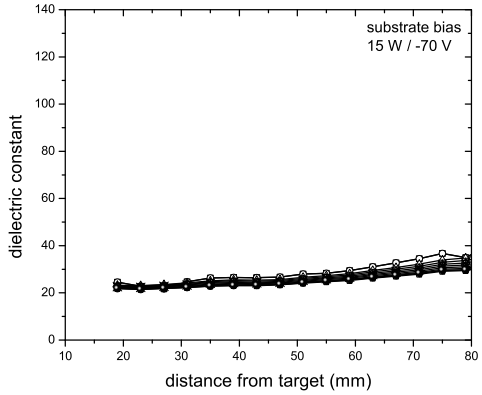

(d) Substrate bias = 15 W / -70 V

Figure 5.4: Inferred dielectric constant at distances from the target for off-axis sputtered Ta_2O_5 at varying measurement frequencies. Oxides were deposited with substrate biases of (a) 0 W, (b) 5 W / -30 V, (c) 10 W / -50 V, (d) 15 W / -70 V. The measurement frequencies are evenly spaced logarithmically at 3/decade from 464 Hz to 1 MHz. Samples 07f135, 08f28, 07f131, 07f133.

from the sputter source, as the deposition rate decreases with increasing distance. Also, increased distance from the plane of the sputter target is associated with a decreased take-off angle from the sputter target, i.e. a more "on-axis" deposition.

At increasing substrate biases, we find an increasingly wide region of 'normal' (ε ~22, nondispersive) behavior close to the gun, as can be seen in Figure 5.4. For example, when Ta_2O_5 is deposited on a substrate with 15 W bias (-70 V bias), even capacitors formed on regions of the film at 7 cm from the target plane demonstrate negligible dispersion in with frequency. However, for biases of only 5 W or 10 W (-30 or -50 V, respectively), dispersion and ε increase with increased distance from the sputtering source, presumably due to the decreased plasma density and the associated density of bombarding ions. At the furthest distances from the sputter target, the dielectric response is very comparable to that of the unbiased films, indicating little to no effective bombardment.

We have observed comparable effects in amorphous SiO_2 and Al_2O_3 sputtered films deposited in the 90° off-axis configuration, and we conclude that the phenomenon is likely to be exhibited by most oxide films deposited under conditions of low ion bombardment.

5.4.4 Dielectric response: on-axis depositions

Deposition from oblique sources is not common, but the effects discussed thus far are equivalent to the edge effects in the widely practiced on-axis depositions. In an on-axis reactive RF sputter deposition, in which the substrate is held parallel to the sputter target, an unbiased substrate is subject to bom-

bardment by Ar neutrals reflected off the target and O^{2-}/O_2- ions accelerated in the electric field. Bombardment decreases with the angle offset from sputter gun axis, ultimately reaching the limit of 90° off-axis, with the effects previously discussed; regions of the film on substrates larger than the target or off-centered from the target may experience decreased bombardment similar to that in off-axis depositions.

In Figure 5.5, therefore, we plot the dielectric constant and the dissipation of films deposited on unbiased on-axis substrates. The properties are plotted at several frequencies as a function of angle from the central gun axis. At less than 0.3 radians (17°) from the central axis, the dielectric properties are 'normal' ($\varepsilon \sim 22$, dissipation~0.02, nondispersive). This is the region on the substrate within the target line of sight and therefore most subject to bombardment by species from the target.

At increasing angle from the sputter gun axis, the signs of low frequency polarization occur-high dispersion and low frequency ε. The furthest angle evaluated in our geometry is 0.57 radians (34°), and the properties at this location resemble those on the off-axis substrate at 5 cm from the target.

The dispersion of ε' and the loss tangent for these slightly angled depositions are plotted in Figure 5.6. Despite the basic similarity, there are some differences between these and the off-axis prepared samples. While the decay in inferred dielectric constant with frequency is similar in films deposited at 90° off-axis and films deposited at 30-34° off-axis, the loss tangents are substantially different. The 30° off-axis samples exhibit a much higher low frequency loss tangent which decays more rapidly with increasing measurement frequency, indicating that the resistive component of the dielectric response is more substantial in

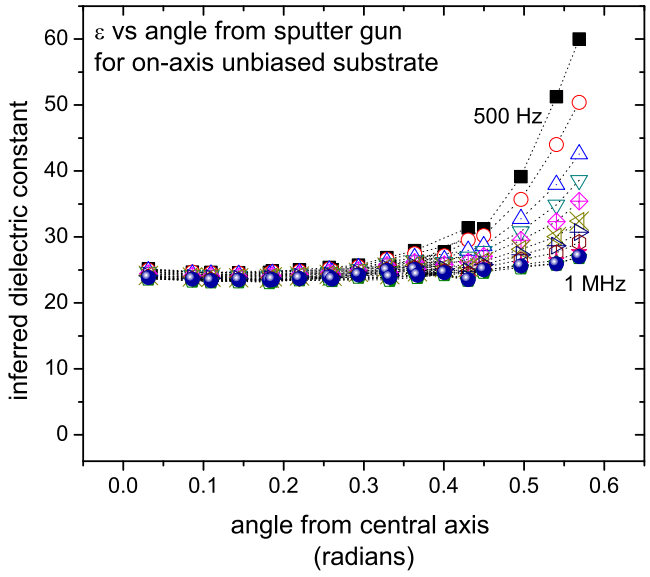

(a) Inferred dielectric constant versus angle from gun axis

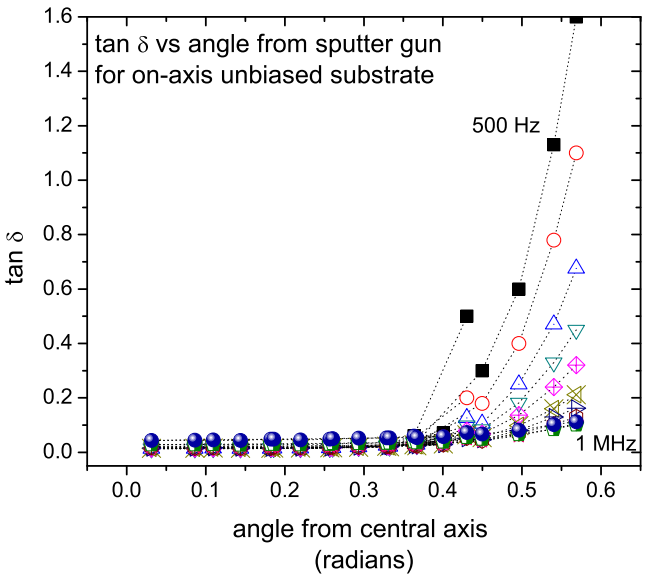

(b) Loss tangent versus angle from gun axis

Figure 5.5: Dielectric response of an on-axis sputtered $Pt/Ta_2O_5/Pt$ capacitor at varying measurement frequencies. Sample 07h33.

these samples.

It is likely that the void structure is different for this deposition orientation and that additional polarization components are significant; however, the similarity of the electronic signature suggests that void-mediated polarizability is also significant in these slightly-angled depositions.

5.4.5 Surface roughness: off-axis and on-axis depositions

The question of how the void structure changes with increasing distance and offset angle from the sputter source is interesting and could be investigated further by a careful TEM study. This might take the form of a systematic study of the correlation between dielectric properties and the void distribution and geometry. AFM images of the surface of the films are an imperfect indicator of bulk structure but suggest that the film morphology has indeed changed.

In Figure 5.7 of the unbiased off-axis deposition, we see that films deposited with limited bombardment have small, equiaxed asperities both close to and 6 cm from the target. For the close trace, we find a root-mean-squared (RMS) roughness and arithmetic roughness of 1.03 nm and 0.806 nm, while further from the target these roughnesses are virtually unchanged, at 1.06 nm and 0.804 nm, respectively. The film in the closer trace is ~70 nm thick, while at 6 cm from the sputter source, the film is 25 nm thick. The small area of the asperities suggests that renucleation events are frequent with limited growth.

We compare this sample to a film of the same thickness sputtered 90° off-axis with 15 W substrate bias. The AFM images of this sample are given in Figure 5.8

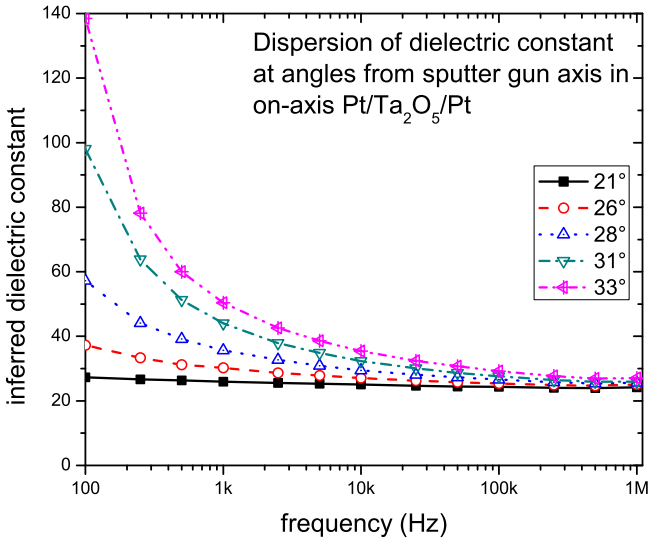

(a) Inferred dielectric constant

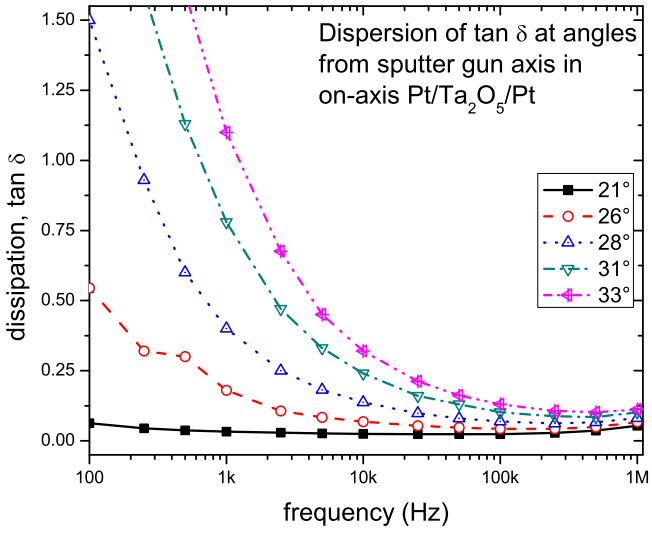

(b) Loss tangent versus angle from gun axis

Figure 5.6: Dispersion with frequency of the dielectric response for an on-axis sputtered $Pt/Ta_2O_5/Pt$ capacitor at varying take-off angles from the target. Sample 07h33.

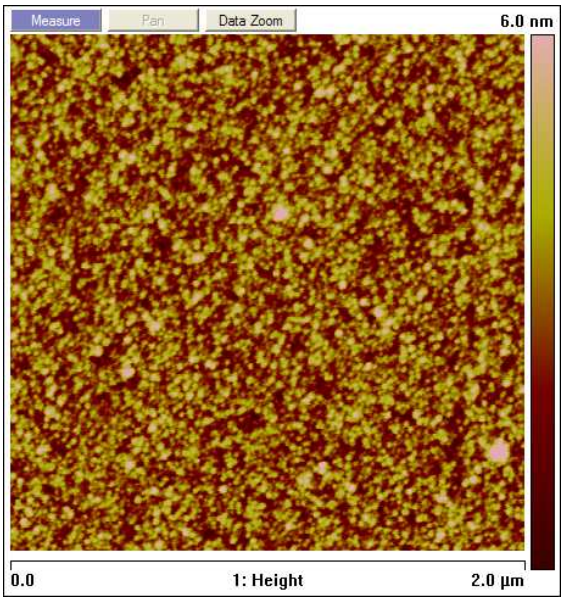

(a) Close to target

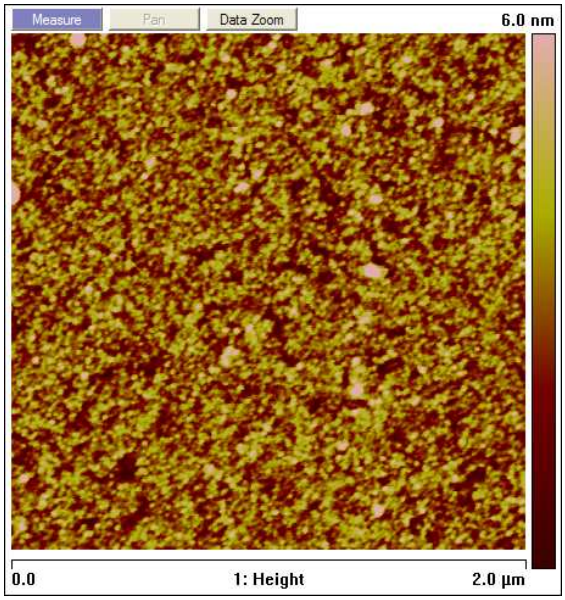

(b) Far from target

Figure 5.7: AFM of off-axis deposited Ta_2O_5 with no bias. Sample 07f135. Courtesy Maxim Noginov [112].

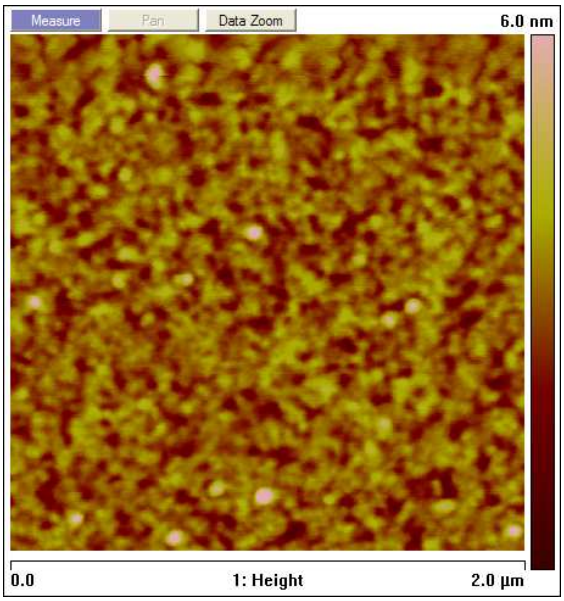

(a) Close to target

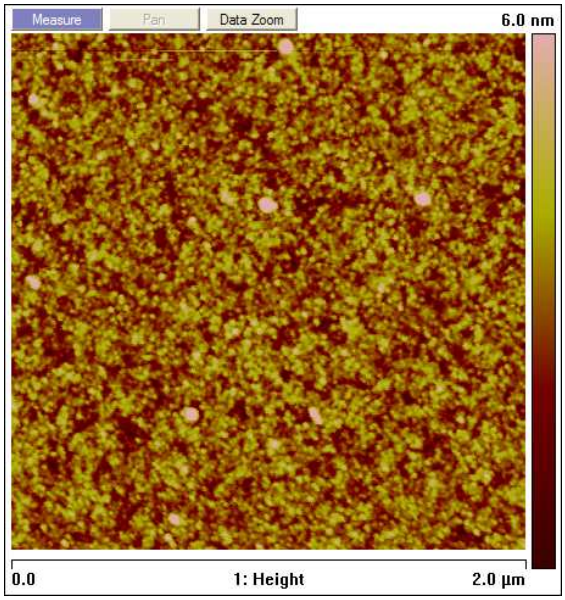

(b) Far from target

Figure 5.8: AFM of off-axis deposited Ta_2O_5 with 15 W bias. Sample 07f133. Courtesy Maxim Noginov [112].

for both close to the target and 6 cm from the target. In this case, the closer region of the film has a markedly different surface structure, with larger and shorter asperities. The RMS and arithmetic roughness for the closer scan are 0.615 nm and 0.462 nm, respectively. For the further scan, the film structure is markedly more similar to the unbiased scans. Asperities have smaller area and are taller, and roughness increases to 0.842 nm and 0.636 nm. The increased roughness at greater distances from the sputtering source suggests that the film structure changes with distance from the source and in particular approaches that of the lightly bombarded film. Changes in surface structure are an imperfect indicator of dielectric properties, however, since these changes are not manifested in an appreciable change in dielectric response, as seen in Figure 5.4.

In regions of the substrates held close to the sputtering target, the difference between the films deposited with and without substrate bias is significant, indicating a substantial change in film structure with ion bombardment. These changes are discernible in the radical change in dielectric properties.

Finally, in Figure 5.9, we give an AFM scan of an on-axis sputtered Ta_2O_5 film of comparable thickness (43 nm). This structure has intermediate character between the lightly bombarded and bombarded 90° off-axis films with asperities of intermediate size and height. RMS and arithmetic roughness are found to be 1.03 nm and 0.779 nm, respectively. On-axis depositions are subject to an uncontrolled bombardment from neutral argon and negatively charged oxygen ions. The intermediate surface roughness of on-axis deposited films compared to biased and unbiased off-axis deposited films indicates that substrate biasing of off-axis substrates can induce a higher bombardment than the uncontrolled bombardment customary of on-axis depositions. This might be due in part to

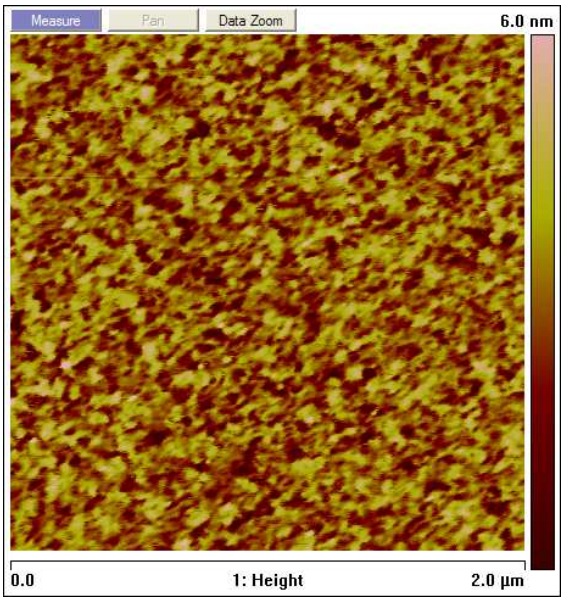

Figure 5.9: AFM of on-axis deposited Ta_2O_5. Sample 07h33. Courtesy Maxim Noginov.

the higher concentration of Ar^+ ions in the plasma than O_2-/O^{2-} ions.

5.4.6 Void-mediated polarization mechanisms: off-axis depositions

We have observed an enhanced and highly dispersive dielectric constant and loss tangent in oxide films deposited in conditions of low ion bombardment and have attributed the behavior to a void-mediated polarization. Finally, we consider the polarization mechanisms at work.

The interior surfaces of voids are comprised of high energy, dangling bonds to which molecules from the atmosphere could adsorb. Adsorbed molecules may themselves exhibit a dipolar (orientational) polarization mode or may pro-

vide a hopping conduction path for charge carriers. Orientational polarization modes are not, in general lossy and thus do not explain the high $\tan\delta$ observed here. Polarization due to hopping along interrupted conducting inhomogeneities in the film is referred to as Maxwell-Wagner polarization; it typically gives rise to a high loss component and responds at frequencies below ~ 100 Hz-100 kHz, depending on the conduction mechanism and details of the conducting/insulating structure [113, 114, 115].

To investigate the environmental sensitivity of these oxides, we prepared capacitors with silver top electrodes, which are permeable to water. $Ag/Ta_2O_5/TiN$ capacitors in which the oxide is deposited 90° off-axis on a biased substrate behave as expected for normal Ta_2O_5.

The $Ag/Ta_2O_5/TiN$ capacitors deposited on unbiased substrates show a strong environmental sensitivity, with the dispersion of the measured dielectric properties varying according to storage environment. Figure 5.10 compares the dielectric response for a capacitor stored in air and in vacuum. After 260 hours in vacuum storage (~4x10^{-6} Torr), the measured dielectric constant falls to ~40, and the dissipation peak shifts to dramatically lower frequencies (< 20 Hz). The enhanced dielectric constant returns within hours in ambient.

These properties are explained by a conduction mechanism mediated by adsorbed water molecules. These adsorbed molecules within the void structure desorb during the vacuum storage, decreasing the availability of charge carriers. Once the film is returned to ambient condition, the water returns, restoring the high polarizability.

Both electronic and protonic conduction have been documented in adsorbed

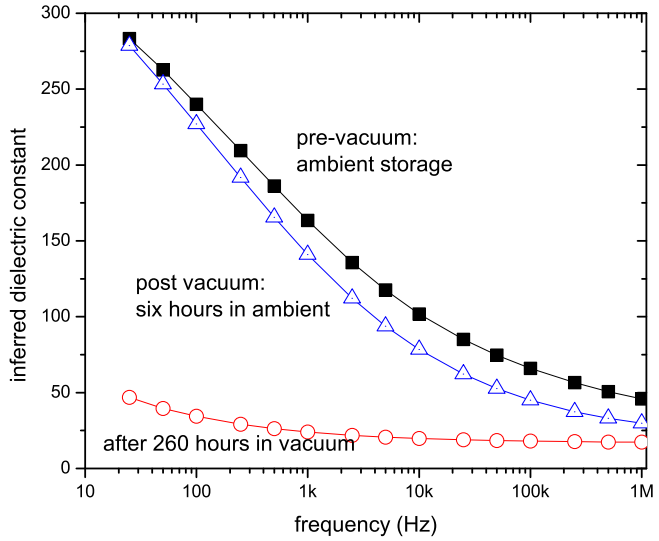

(a) Capacitance

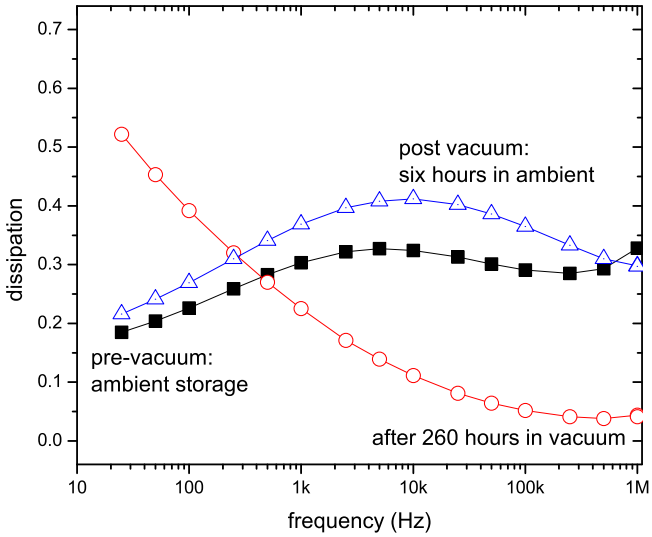

(b) Loss tangent

Figure 5.10: The capacitive response of $Ag/Ta_2O_5/TiN$ capacitors to storage in vacuum. Sample 98f31.

water, the former dominating in the first two adsorption layers and the latter dominating in the more bulk-like layers [116, 117]. Hence desorbing water may also affect the type of charge carriers and their conduction mechanism. A 2.5 nm diameter void, such as those observed in Figure 5.3 in films deposited without substrate bias, can accommodate up to three layers of adsorbed water [118].

The reproducibility of water adsorption and desorption from open porous materials as a function of relative humidity has been exploited by researchers in humidity sensors [114, 115, 119, 120, 121, 117].

The capacitive response to adsorbed moisture has been modeled [115] using R. W. Sillars' extended analysis of Maxwell-Wagner polarization [113]; inhomogeneities in the material are modeled as semiconducting cylinders oriented parallel to the electric field [113].

Following Sillars' extension to the Maxwell-Wagner analysis, we find that the dielectric response given in Figure 5.10 is consistent with an AC conductivity inside the voids of 10^{-6} to 10^{-5} S/m at 10 kHz. A discussion of AC conductivity in the context of Sillars' derivation is found Appendix A.

The measured loss tangent during ambient storage is modeled well for AC conductivities within the voids of $\sigma = \sigma_0 \omega^s$ with s=0.97. Values between 0.6 < s < 1 are consistent with a hopping conduction among localized states [48]. Protonic conductivity along adsorbed water is well described by hopping conduction [122].

Polarization mechanisms are not limited, however, to hopping conduction along the interior of voids. Impurities are also incorporated during deposition and may contribute to the polarizability by exhibiting orientational polariza-

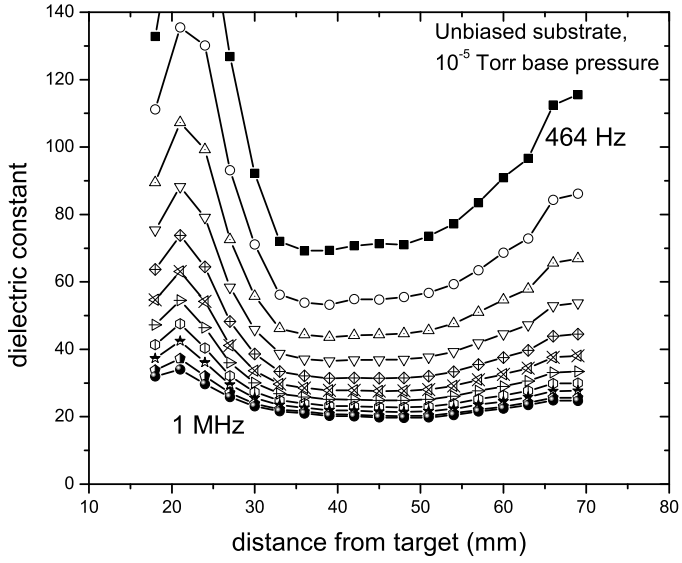

(a) Unbiased deposition with a background pressure of 1.5x10^{-5} Torr

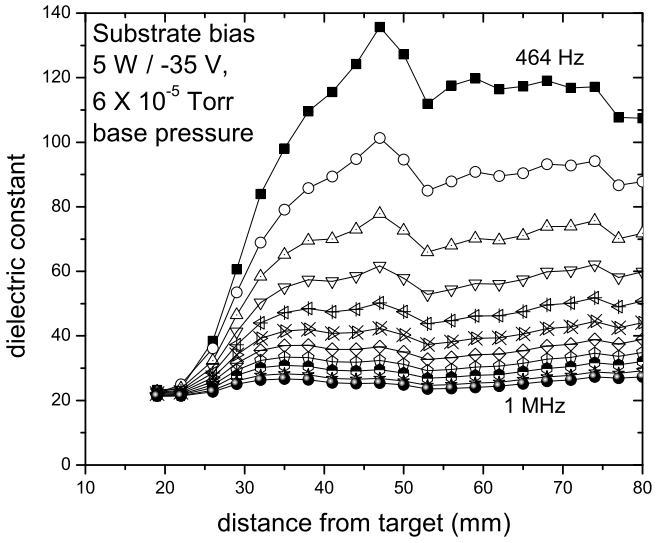

(b) Deposition with 5 W (-35 V) substrate bias with a background pressure of 6x10^{-5} Torr.

Figure 5.11: Inferred dielectric constant at distances from the target for off-axis sputtered Ta_2O_5 at high background pressures. Samples 07f134 and 07f132.

tion modes. In Figure 5.11, we plot the inferred dielectric constant for two $Pt/Ta_2O_5/Pt$ samples deposited with high background pressures prior to deposition as a function of distance from the sputter source. The base pressure in the chamber prior to deposition was somewhat higher than in the other depositions, for which the base pressure was 4×10^{-6} Torr.

Figure 5.11a is from a deposition on an unbiased substrate with a base pressure of 1.5×10^{-5} Torr, while Figure 5.11b is from a deposition on a substrate biased to 5 W (-35 V) with a base pressure of 6×10^{-5} Torr. We compare these results to those in Figure 5.4a and b which are from samples deposited at lower background pressures and find that sputter depositions with high background pressures reveal a further enhancement of the low frequency polarization, particularly at low deposition rates. The high background pressure is presumably dominated by water, suggesting that hydroxyl ions are also incorporated into voids and the film bulk during the deposition and contribute to the low frequency polarization.

The introduction of voids is widely exploited in low-κ dielectrics to lower the dielectric constant by decreasing the density; see, for example, Reference [123]. A closed pore structure is required, however, to prevent the adsorption of ambient moisture, among other concerns [3].

We note that while this nanophased structure of open voids within the oxide is detrimental to the evaluation of the inherent material dielectric properties, similar nano- or micro-void structures have demonstrated applicability in a variety of fields. Voids can result in an anisotropic modulation of the oxide optical constants, an effect that has been exploited to create birefringent polarizers [107], while voids in a tungsten oxide from an oblique sputtering source

have been proposed for Li^+ ion intercalation [108]. Finally, Steele et. al. have fabricated environmental (humidity) sensors based on oxides prepared with a high density of voids using oblique angle depositions. The strong capacitive response of their interdigitated capacitors to humidity changes exploits the adsorption of molecules from the atmosphere in uncapped voided oxides [110].

To enable an accurate evaluation of intrinsic dielectric properties in composition spreads, for example, we require the elimination of the void structure in obliquely deposited films. Substrate biasing is a versatile technique for increasing ion bombardment while maintaining oblique angle deposition from multiple sputter sources, a necessary geometry in the co-deposition of combinatorial libraries of mixed oxide dielectrics.

5.5 Conclusions

We have studied model dielectric Ta_2O_5 films, prepared by on-axis and 90° off-axis reactive RF sputtering, and have found that ion bombardment during oxide deposition is necessary for producing dense films with well-behaved dielectric properties. Without this bombardment, the films are subject to an additive polarization due to the conduction of charge carriers along internal voids. This polarization masks the intrinsic dielectric behavior, complicating the evaluation of candidate dielectric materials.

The controlled Ar^+ ion bombardment induced by substrate biasing during off-axis depositions mimics the uncontrolled O_2-/O^{2-} bombardment of on-axis depositions. Exploiting this technique, the ion bombardment can be controllably increased even above that of the uncontrolled bombardment to on-axis

substrates. The controlled increase in ion bombardment is necessary for evaluations of candidate dielectric materials deposited in an off-axis geometry, such as the co-sputtering of materials used in composition spreads for high-throughput screening [62].

In depositions on on-axis substrates, the uncontrolled ion bombardment enables the deposition of a high quality dielectric on regions of the substrate directly on-axis to the sputter gun. Regions of the film deposited at angles of >25° are subject to an additive polarization mechanism similar to that observed in films deposited off-axis.

The effectiveness of the substrate bias in eliminating voids is found to vary with plasma density (i.e., distance from the sputter source). We have demonstrated that in our vacuum system with sufficient biasing (15 W / -70 V), the dielectric properties of Ta_2O_5 deposited from a single 90° off-axis sputter gun are well-behaved as far as 7 cm from the plane of the sputtering target. When sputtering from multiple sputter guns simultaneously, the plasma density increases and becomes more spatially uniform in the region of the substrate; this may accommodate a decrease in the applied substrate bias.

5.6 Interference among powered electrodes

In this section, we consider another critical assumption made in co-sputtering of several targets: that deposition from a sputter gun is not affected by the proximity to or power applied to the substrate or other sputter guns.

Gregoire *et. al.* [124, 125] have already demonstrated a violation of this non-

interference assumption. Depending on the particular species being deposited, one element may be preferentially resputtered from the growing film by neutral argon atoms reflected off the target of another element. Thus, the deposition profile from an individual sputter source is different from its contribution to the co-sputtered deposition profile. Resputtering during co-sputtering of dielectric oxides is discussed in Chapter 6 for the specific case of co-deposited TaO_x-GeO_x.

5.6.1 Resputtering due substrate biasing

In addition to bombardment by reflected Ar atoms, argon ion bombardment induced by the substrate bias may also cause resputtering of the depositing film. To evaluate the significance of this effect, we deposit two Ta_2O_5 films with and without an applied substrate bias. Both films are deposited from elemental tantalum targets powered to 100 W rf for one hour. In Figure 5.12, we present results from the Woollam spectroscopic ellipsometer. The measured thickness is normalized to the deposition time to plot the deposition rate; we also plot measured refractive index, which scales with the material density, according to the Lorentz-Lorenz equation (Equation 3.3).

We find that the deposition rate on the more heavily bombarded film is less than significantly less than the deposition rate on the unbiased substrate. The decreased thickness may be due to resputtering of the depositing film by the argon ion bombardment induced by the substrate bias. Alternatively, the decreased thickness in the bombarded film may reflect the increase in density.

As expected, we find that the film deposited on a biased substrate has the greater density (higher refractive index), since it lacks the void structure associ-

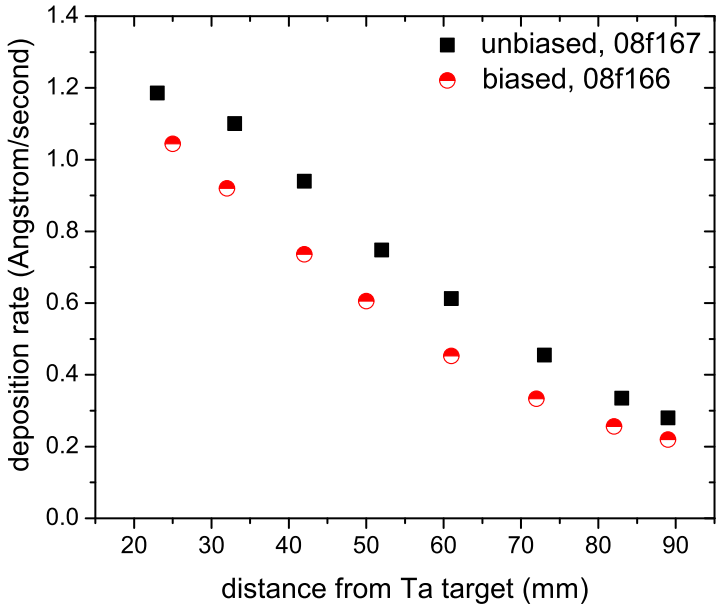

(a) Deposition rate

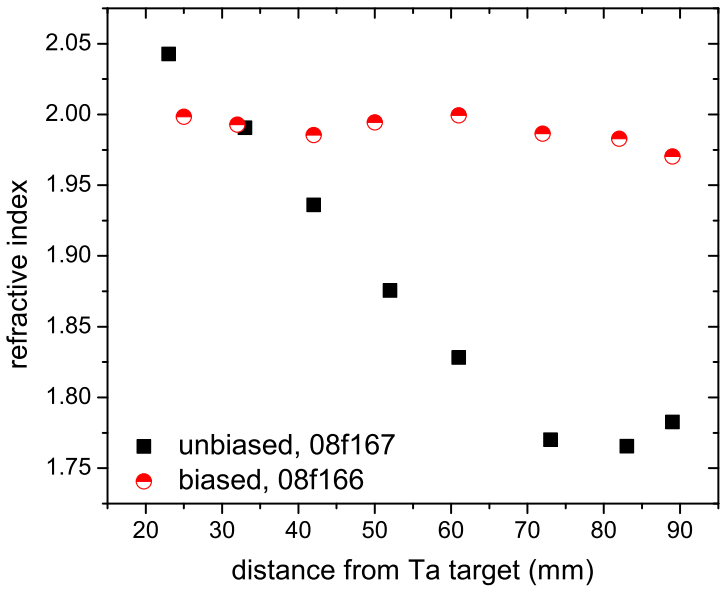

(b) Refractive index

Figure 5.12: Woollam spectroscopy ellipsometry of Ta_2O_5, deposited with and without substrate bias. Sample 08f166 and 08f167.

ated with limited ion bombardment. Moreover, the density (refractive index) of the film on the unbiased substrate decreases with increasing distance from the sputtering source, as the incidental ion bombardment associated with proximity to the plasma source decreases.

The density of films may be found analytically using the Lorentz-Lorenz equation given the electronic polarizability of Ta_2O_5, α_{el}. We calculate the electronic polarizability in the method of Tessman, Khan, and Shockley [126] using the density and refractive index n of fully dense Ta_2O_5:

$$\alpha_{el} = \frac{3V}{4\pi}\frac{n^2-1}{n^2+2} \tag{5.1}$$

in which V is the volume of the Ta_2O_5 and is calculated from the crystal structure. The refractive index is taken to be 2.15 [127, 128] for fully dense Ta_2O_5 with a density of 8.35 g cm^{-3} (hexagonal, PDF 18-1304, 21-1199). This calculation results in an electronic polarizability of 1.15×10^{-23} cm^3.

We use the calculated electronic polarizability from Eqn. 5.1 and the measured refractive indices to calculate the density of the Ta_2O_5 films. The densities are plotted in Figure 5.13. As noted previously, they indicate that, unlike the density of the heavily bombarded film, the density of the film on the unbiased substrate changes significantly with distance from the sputter source during deposition. Rather, it decreases as the density of energetic particles in the plasma decreases with increasing distance from the sputter source. Neither film is fully dense at any distance from the sputtering source. The highest density is 94 % for the film deposited without substrate bias, close to the target; the material deposited at 8 cm from the sputtering source on this film is 77 % dense by these calculations.

To consider the correlation between the bombarded material's increased

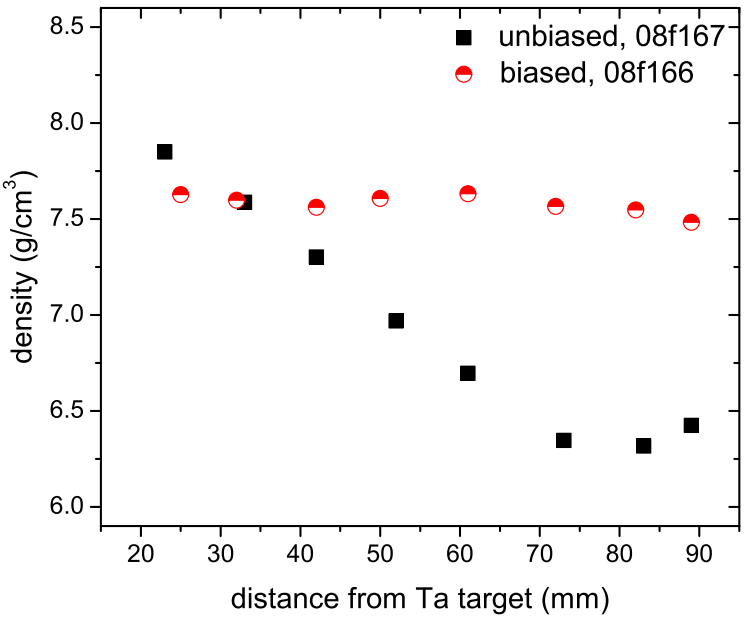

Figure 5.13: Density of Ta_2O_5 films deposited with and without substrate bias. Samples 08f166 and 08f167.

density and its decreased thickness, we calculate the deposition rate in terms of nmol·cm^{-2}s^{-1} and plot the results in Figure 5.14. We find that the molar deposition rates for films deposited with and without substrate bias are very similar at 8 cm from the sputtering target. However, the molar deposition rate closest to the target indicates that this level of substrate bias may resputter as much as 15 % of the material that would have deposited on an unbiased substrate. Again, resputtering is most evident close to the sputtering source because of the high density of energetic particles.

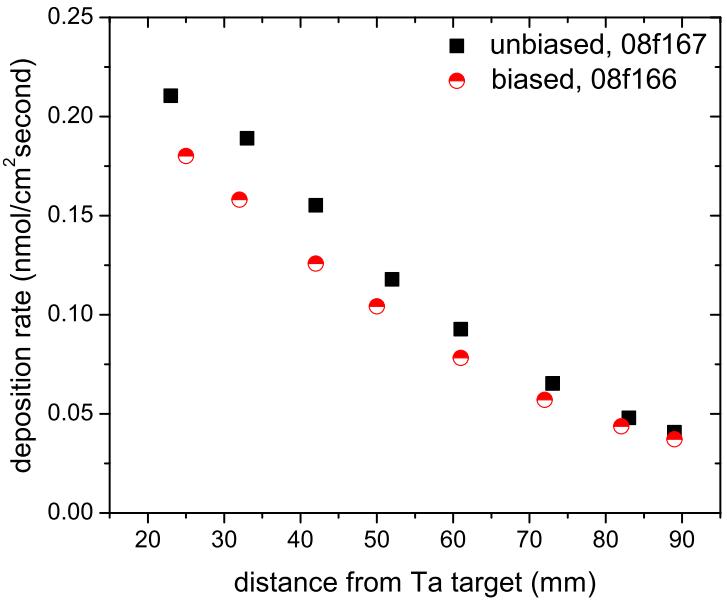

Figure 5.14: Molar deposition rate of Ta_2O_5 films deposited with and without substrate bias. Samples 08f166 and 08f167.

5.6.2 Magnetic field of the sputter source

Another mechanism of interference among the magnetron sputter guns is related to the magnetic field of the guns. Magnetron sputter guns have a strong magnet, the field of which concentrates ions and electrons in the vicinity of the sputter target. Neighboring magnetic fields interact, and in this section, we consider the effect of a nearby 4" diameter sputter gun on the deposition profile for a 2" sputter gun. We note that in contrast to resputtering which depends on the power to the sputter sources, interfering magnetic fields are present even when the source is not powered.

To investigate the effect of a nearby 4" diameter sputter gun, we deposited

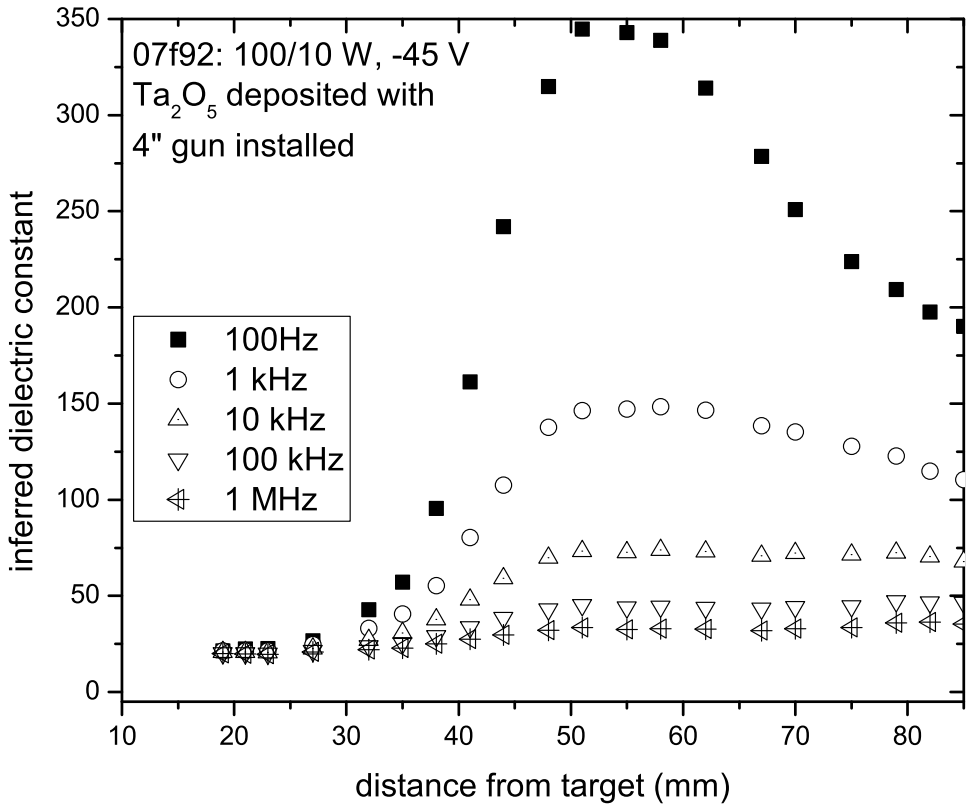

Figure 5.15: The inferred dielectric constant of Ta_2O_5 versus distance from the sputter source at measurement frequencies of 100 Hz to 1 MHz. This oxide film was deposited from a single off-axis 2″ Ta target with a substrate bias of 10 W, but its response differs from that of Figure 5.4 (c) due to the magnetic field of the on-axis 4″ sputter gun. Sample 07f92.

Ta_2O_5 off-axis from a single 2″ Ta source while the 4″ magnetron gun was present but not powered. The substrate was biased with 10 W (-45 V). In Figure 5.15, we plot the inferred dielectric constant versus distance from the Ta target. The dielectric constant is evaluated at each decade from 100 Hz to 1 MHz. We compare this data to that in Figure 5.4c for an identical deposition, save the installation of the 4″ gun. The region of 'normal' behavior (low dispersion, $\varepsilon \sim 23$, low $\tan\delta$) extends only to 3 cm from the target when the larger gun is present, while without the 4″ gun it extends to 4 cm. Additionally, the increase in inferred dielectric constant outside the normal region is higher in the film deposited in the presence of the 4″ magnetron than in the film deposited without. For example, in the region of the films deposited at 7 cm from the sputtering target, the inferred dielectric constant at 1 kHz is 120 for the film deposited in the presence of the 4″ magnetron and 55 in the film deposited without the larger magnetron present.

The large magnetic field of the 4″ gun interferes with the substrate biasing. The field of the larger magnetron apparently changes the plasma configuration so as to decrease the ion density in vicinity of the substrate. The decreased ion density decreases the ion bombardment on the substrate, particularly at long distances from the smaller sputter gun.

5.7 Proof of concept: co-sputtering of Ta_2O_5 from off-axis sources for dielectric material composition spreads

To demonstrate the viability of the off-axis sputtering for exploring composition spreads to identify candidate dielectric materials, we have deposited Ta_2O_5

films from two off-axis tantalum targets. We suggest that if the dielectric properties of Ta_2O_5 remain constant with position across the substrate, any variation seen in properties in a hypothetical A-B-C oxide film is due to the relative ratio of A:B:C (the material composition), and not due to artifacts associated with distance from the sputter source. Deposition from three tantalum targets at 90 ° off-axis would further strengthen this proof of concept.

Additionally, in this section, we consider the effect of elevated substrate temperature. In previous sections, we have demonstrated that enhanced ion bombardment due to substrate biasing densifies the depositing film. Increased substrate temperatures during deposition can have a similar effect, as demonstrated in Chapter 3. Both increase the surface mobility of arriving species.

All of the films presented in this section were reactively sputtered from two facing tantalum sputter targets. The tantalum targets are 112 mm apart from each other. The sputtering gases were 20% oxygen in argon at a total flow rate of 50 sccm and a pressure of 30 mT. The electrodes are evaporated platinum. For each capacitor, we measure the dielectric constant and dissipation at five different frequencies between 100 Hz and 1 MHz.

Since the variation in properties is largely one-dimensional along the line connecting the two sputtering sources, the data is presented as the average of measurements taken at each position along this line, excluding obvious outlier data points associated with shorted capacitors. The abscissa for these plots is the distance from the more highly powered target. Because of the width of the ground shields of each magnetron sputter gun and the length of the substrate holder, capacitors are not formed on the full range (0 to 112 mm) between the targets. Rather, capacitors are measured on regions of the film deposited from

Table 5.1: Deposition parameters for three films, deposited from facing Ta targets

Sample and data figure	Target powers [W]	Substrate power [W] and voltage [V]	Substrate temperature [°C] / base pressure [Torr]
08f38 / Fig. 5.16	100/30	0/0	230 / 1×10^{-5}
08f39 / Fig. 5.17	100/30	20/-75	300 / 1×10^{-5}
08f30 / Fig. 5.18	100/30	15/-95	r.t. / 4×10^{-6}

17 mm to 95 mm from the more highly powered target. (Material deposited at 95 mm from the more highly powered target is at 17 mm from the more weakly powered target.)

High gun power and high substrate bias have the highest efficacy in eliminating voids. In Figures 5.16 and 5.17, we present films deposited on heated substrates (230 °C and 300 °C, respectively) with 100 W power supplied to one tantalum target. The more weakly powered tantalum target was powered to 30 W. We summarize the deposition parameters for the three samples discussed next in Table 5.1.

The unbiased sample, for which data is presented in Figure 5.16, has the characteristic signature observed in depositions from one source on unbiased substrates: high dispersion, high loss factor, enhanced dielectric constant at low frequencies. The scale on the dissipation plot is chosen for ease of comparison to data from biased substrates; the full dataset is presented in the inset. The substrate was not long enough to reveal the properties closest to the more weakly powered target. The deposition rate is much lower at the weakly powered tar-

get, and the plasma density is less at this target. The effects of ion bombardment must therefore be smaller. (While the dc biases to the targets are very similar with -300 V for the 100 W powered target and -250 V for the 30 W powered target, the more weakly powered target has a much lower current (ion bombardment flux).)

We compare this sample to a sample with a similar deposition recipe, except with a substrate bias of 20 W (-75 V). The inferred dielectric constant and dissipation are presented in Figure 5.17. The substrate bias is shown to be effective at eliminating the lossy low frequency polarization observed in Figure 5.16. High frequency dissipation is low <0.05 out to 70 mm from the 100 W target, though dissipation at 100 Hz and 1 kHz increases beyond 40 mm, indicating that some voids or dangling bonds are still present at this bias. The dielectric constant follows a similar trend, with an increase to ~40 at 40 mm from the target. Again, the sample does not extend long enough to reveal the effects associated with proximity to the 30 W powered target.

We note that the increased substrate temperature of these depositions was accompanied by an increase in background pressure to 1×10^{-5} Torr during deposition and that increases in background pressure were observed to increase dispersion in the properties of Ta_2O_5 films deposited from a single 90° off-axis target. The effect is particularly significant at further distances from the sputtering source. We pursue this investigation from dual sources in the next section.

Finally, we compare these samples to a sample with a similar deposition recipe on a biased but unheated substrate. The power to the targets are again 100 W and 30 W, while the substrate is biased to -95 V (15 W). Figure 5.18 is the inferred dielectric constant and dissipation for this sample (08f30). The defect

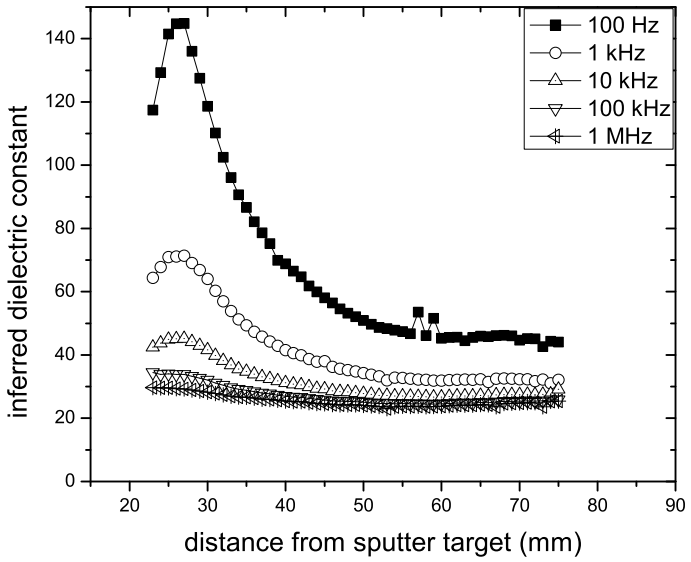

(a) Inferred dielectric constant

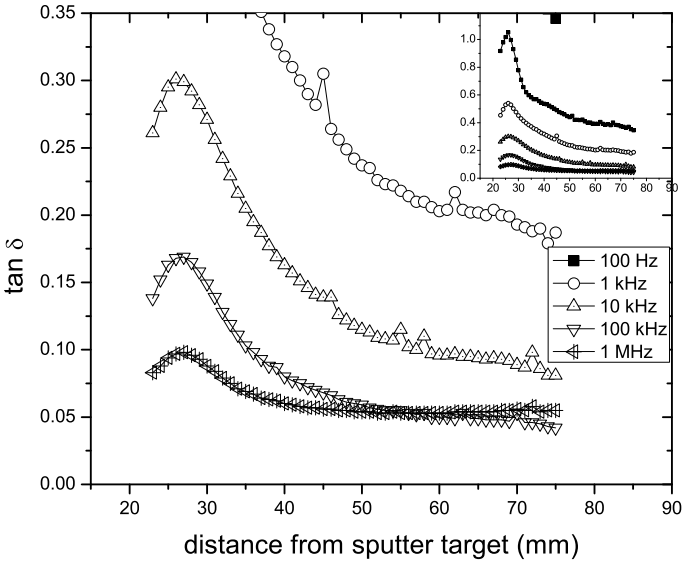

(b) Dissipation

Figure 5.16: Dielectric properties of Ta_2O_5, deposited on a heated, unbiased substrate. The substrate temperature during deposition was 235°C. Sample 08f38.

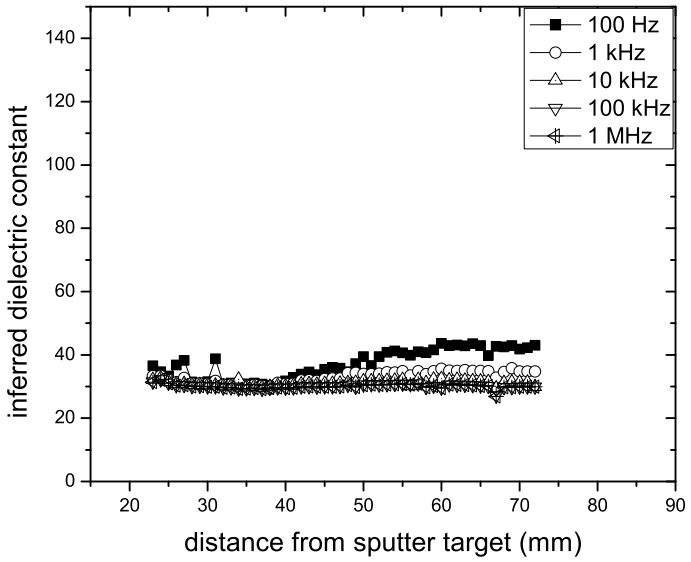

(a) Inferred dielectric constant

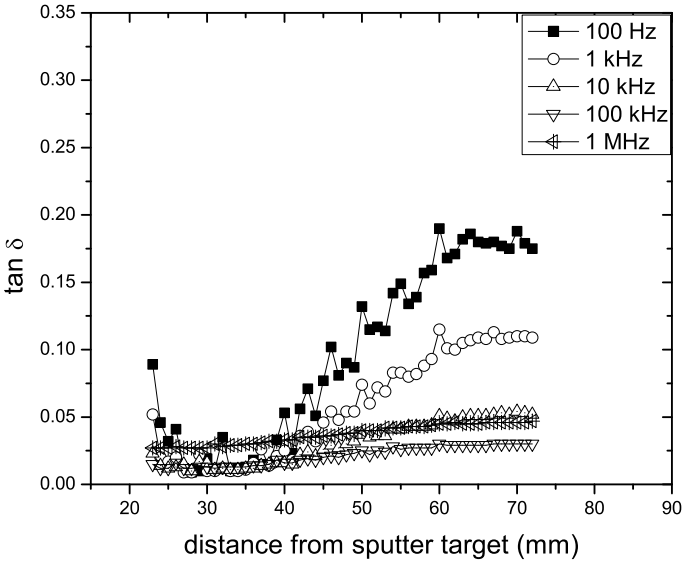

(b) Dissipation

Figure 5.17: Dielectric properties of Ta_2O_5, deposited on a heated, biased substrate. The substrate temperature during deposition was 300°C; the substrate was biased to 20 W rf (-75 V dc). Sample 08f39.

polarization does not significantly increase the dielectric constant until 65 mm from the sputtering target. The dissipation behavior is somewhat surprising with a higher dissipation at 1 kHz than at 100 Hz, but this is also observed for some films deposited from a single Ta target and may indicate a higher characteristic frequency of the polarization. This is the longest of the samples, with the substrate extending to within 25 mm of the more weakly powered sputter source. At this distance, there is still little to no observable effect from the low power source.

In comparing these three films, we see that elevated substrate temperatures to 235 °C are insufficient to eliminate the void-mediated polarization observed in oxide films deposited from 90° off-axis targets. The ion bombardment induced by substrate biasing is critical to void elimination. The increase in homologous temperature from 20 °C to 235 °C is slight, while ion bombardment provides momentum in addition to kinetic energy. We are hesitant to compare the biased samples to each other. It is uncertain whether differences between Sample 08f39 (data in Figure 5.17) and Sample 08f30 (data in Figure 5.18) are predominantly due to run-to-run variations, or 08f30's slightly increased substrate bias, or 08f39's elevated substrate temperature during deposition and the associated increase in background pressure.

Sufficient substrate biasing is required to eliminate void-mediated low frequency polarization through increased ion bombardment. To assure sensitivity to intrinsic material properties across a full 3" (76 mm) wafer, however, we may require highly powered sputter sources, with the associated increase in deposition rates and plasma density. Limiting ourselves to highly powered sputtering sources places limits on the composition space accessible in co-sputtered com-

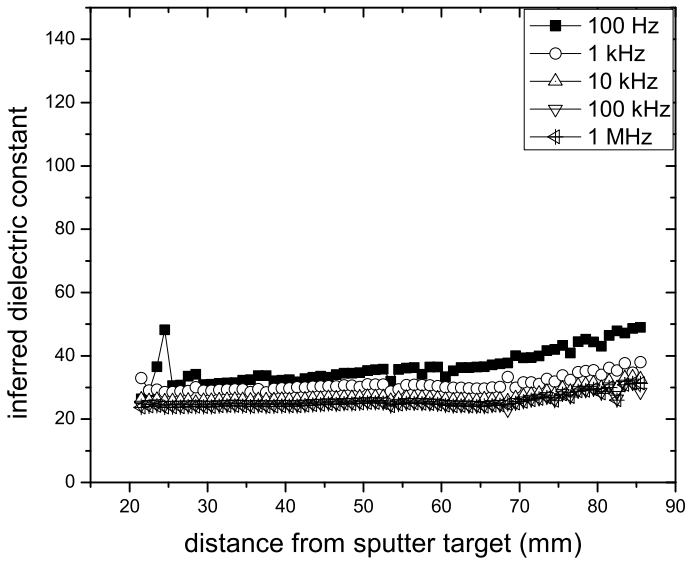

(a) Inferred dielectric constant

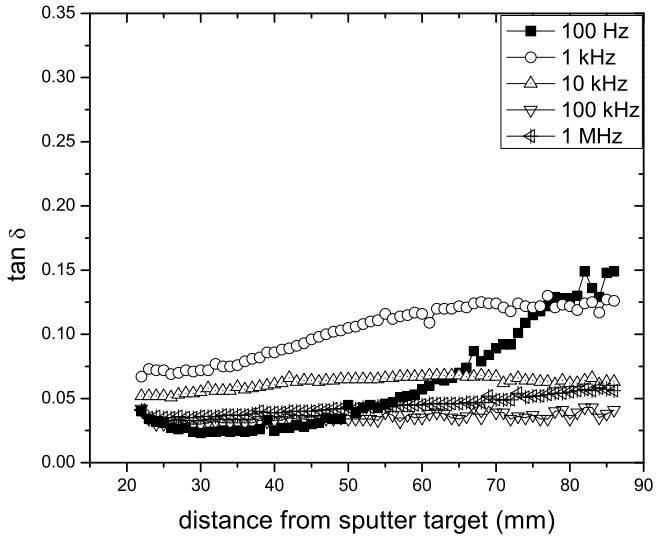

(b) Dissipation

Figure 5.18: Dielectric properties of Ta_2O_5, deposited on a unheated, biased substrate. The substrate was biased to 15 W rf (-95 V dc). Sample 08f30.

Table 5.2: Deposition parameters for two films, deposited from facing Ta targets, on substrates with insufficient bias

Sample and data figure	Target powers [W]	Substrate power [W] and voltage [V]	Substrate temperature [°C] / base pressure [Torr]
07f160 / Fig. 5.19	100/30	10/-20	r.t. / 4×10^{-6}
07f158 / Fig. 5.20	100/30	10/-28	210 / 3×10^{-5}

position spreads, however, since low-level substitutions are less accessible and re-sputtering is a greater concern.

Effect of substrate temperature in insufficiently biased Ta:Ta oxide

Unlike a previous study [129] of the ZrO_2-SnO_2-TiO_2 system, we do not observe a strong change in dielectric properties with the substrate temperature in the present study of Ta_2O_5 co-sputtered films. The effect may be masked, however, by an uncontrolled increase in the background gas pressure during deposition. In this section, we consider two similar samples whose depositions differ intentionally by the substrate temperature and unintentionally by the background gas pressure. Both were deposited on weakly biased substrates. The deposition parameters are given in Table 5.2.

In Figure 5.19, we present the inferred dielectric constant and dissipation of a Ta_2O_5 film, deposited from tantalum sources powered to 100 W and 30 W. The substrate is rf-biased to -25 V (10 W) and was not intentionally heated. Note that the $\tan\delta$ scale in this figure is different from those in the previous section, and

is chosen to match the inset in Figure 5.16. We observe that the substrate bias is quite insufficient to prepare a high quality dielectric oxide. There is very limited suppression of the low frequency polarization close to the highly powered target, but the effect of the applied substrate bias is unknown given the similarity to the dielectric response of a sample deposited on an unbiased substrate (data given in Figure 5.16). Similar to the behavior of samples deposited on unbiased substrates, inferred low frequency dielectric constant decays in regions of the film further from the sputter source during deposition. The dissipation is high, with a low frequency $\tan\delta > 0.2$, and has a significant dispersion with frequency.

We compare this sample to another deposited within a few days, also on a lightly biased substrate using the same recipe, but at an elevated substrate temperature of 210 °C. The dielectric constant and dissipation are given in Figure 5.20. An inset is given in the plot of the dielectric constant to reveal the values at 100 Hz; the scale chosen for the main plot is for comparison with other plots in this section. The low frequency dielectric constant and loss tangent are significantly higher than in the sample deposited without intentional heating.

An additional effect of high temperature is the increase in base pressure before and during deposition. While the depositions with no intentional heating take place in a background vacuum of 4×10^{-6} Torr, this sample was deposited in a vacuum of 3×10^{-5} Torr. The increase in background pressure is attributed to outgassing by the walls of the chamber, which are heated radiatively by the substrate heater. The effect of high background pressure on the film's dielectric properties is similar to that observed when the film is deposited from a single tantalum source with a high background pressure. We note that the composition of the extra gas molecules is likely different in this case than in the previous. The

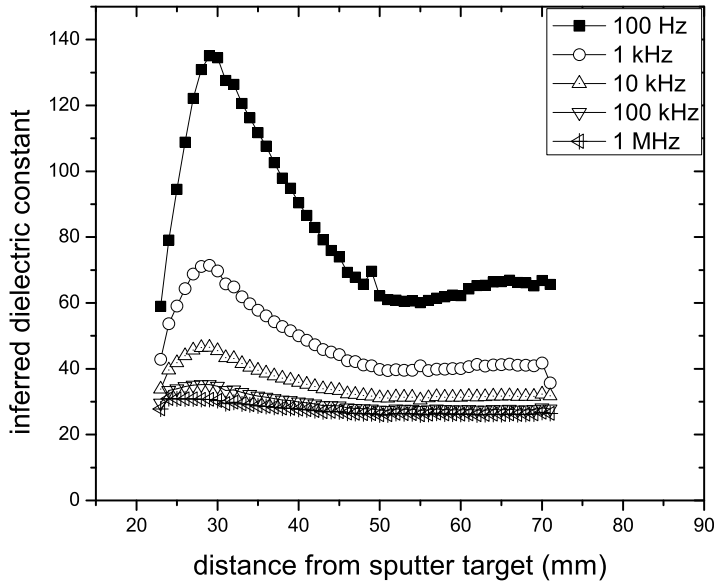

(a) Inferred dielectric constant

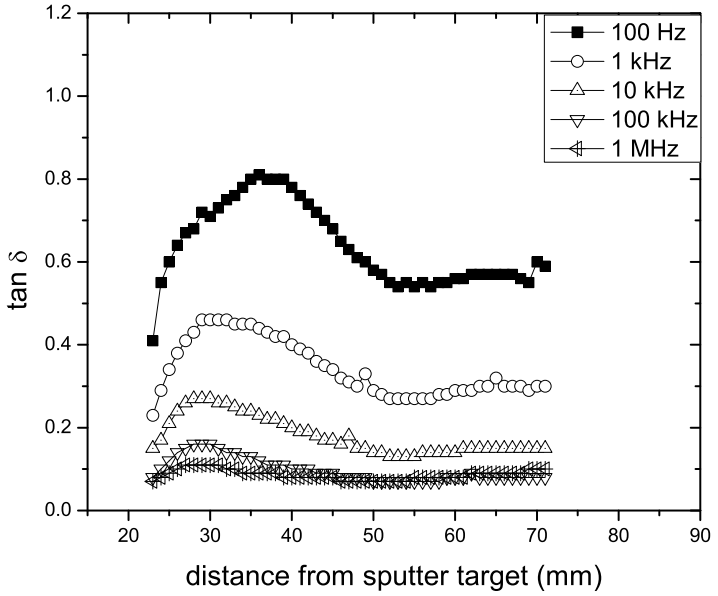

(b) Dissipation

Figure 5.19: Dielectric properties of Ta_2O_5, deposited on an uheated, lightly biased substrate. The substrate was biased to 10 W rf (-20 V dc). Sample 07f160.

background pressure during substrate heating can be attributed to outgassing of the chamber walls, while the background pressure described during single source depositions was due to a small vacuum leak or short pumping time. We suggest outgassing from the chamber walls has a higher moisture content since water adsorbed to surfaces at room temperature while oxygen and nitrogen (the main atmospheric components) have very limited adsorption. A vacuum leak, on the contrary, has a very similar composition to the atmosphere, largely oxygen in nitrogen. The moisture content in the atmosphere during substrate heating likely contributes to the incorporation of hydroxyl groups and other dangling bonds within the film. These, in turn, contribute to the low frequency, lossy polarization observed in films with insufficient substrate bombardment.

We can not elucidate the effect of elevated substrate temperatures in these samples, since any effect is likely overshadowed by the effects of the increased background pressure during deposition.

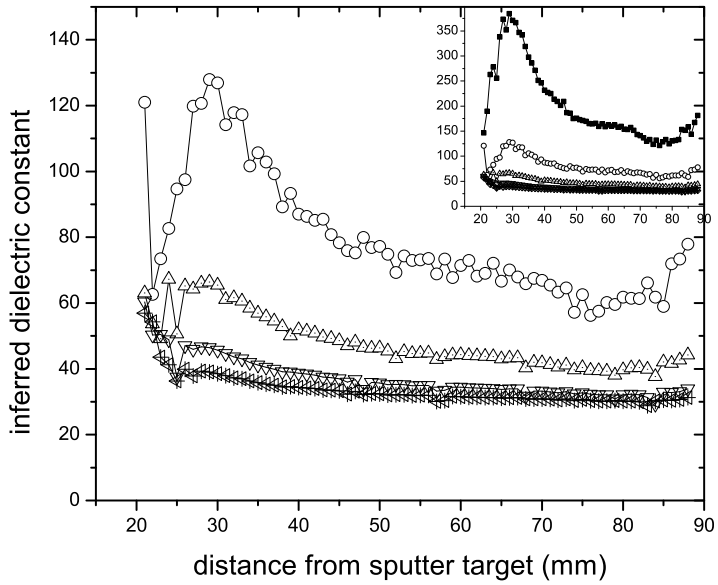

(a) Inferred dielectric constant

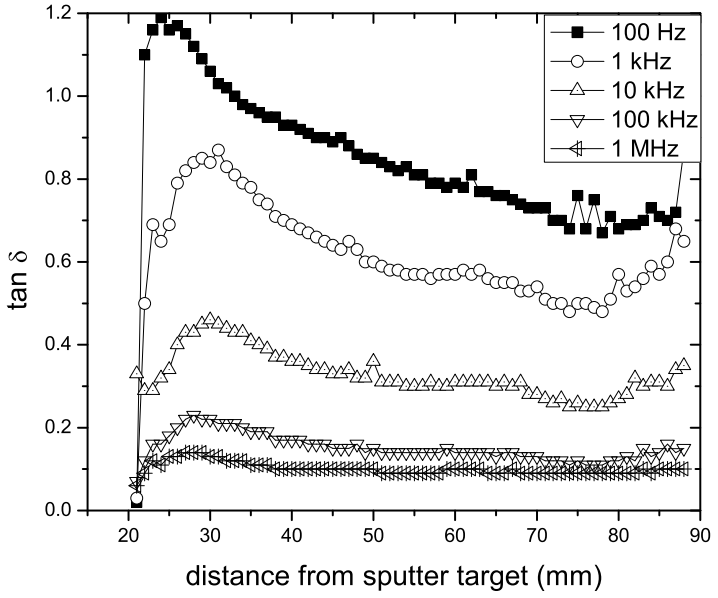

(b) Dissipation

Figure 5.20: Dielectric properties of Ta_2O_5, deposited on a heated, lightly biased substrate. The substrate temperature during deposition was 210°C; the substrate was biased to 10 W rf (-28 V dc). Sample 07f158.

CHAPTER 6

EFFECT OF ELEMENTAL COMPOSITION IN CO-SPUTTERED DIELECTRIC OXIDES

The elemental composition of an oxide dielectric can have a significant effect on the dielectric properties. This observation is often made with respect to the dielectric constant. The dielectric constant of a mixed oxide is often observed to be an intermediate value of its component oxides [6, 13, 130]. The dielectric constant may be high by one metal oxide, but the second or third oxide may also be included due to superior interfacial properties on silicon [22, 17], or a higher band gap [21], or a decreased leakage current [24].

Li *et al.* [22, 23] have studied dielectric properties of thin (<10 nm thick) gate dielectrics in a range of compositions $Hf_xTi_{1-x}O_2$. The oxides are prepared by CVD and evaluated as MIS capacitors. Their results, therefore, are very timely for integration of higher k dielectrics on silicon channels, but sacrifice sensitivity to the oxide's intrinsic dielectric properties, in favor of probing the composition and the thickness of the interfacial layer on silicon channels [22]. While increased titanium content frustrates crystallization in high temperature anneals, it is also found to increase the thickness of the interfacial layer on silicon [22, 23].

Lu and co-workers [17] pursued a careful study of reactively co-sputtered Hf-Ta oxide dielectrics over the full composition range. Substrate were rotated at 20 rpm during deposition to negate the position-dependent variations in composition and deposition conditions; each deposition contained a single composition and was measured in a MIS structure. Their results, therefore, do not have the density of composition information as our composition spread samples and are additionally complicated, as they note, by the intertwined variations in

EOT and in interfacial silicon oxide thickness. They concluded that increased hafnium content minimized the SiO_x interfacial layer, but that the mixed oxide was preferable for low leakage currents and low fixed charge density within the oxide film.

The effects of elemental composition can also be evaluated by a continuous composition gradient across a single sample; this technique exploits the geometry of three sputter sources at 90 ° angles to each other and to the substrate. Results from binary Ta_2O_5-GeO_2 and ternary Ta_2O_5-GeO_2-X (where X represents a third transition metal oxide) gradients are discussed. We additionally reconsider the effects of substrate biasing when depositing films of mixed metal oxide composition.

Maxim Noginov collected much of the electrical data presented in this section and otherwise contributed to the analysis presented here.

6.1 Off-axis co-sputtering methodology to create composition spreads

Combinatorial materials science is predicated on the premise that composition space is more efficiently surveyed by the preparation of a single sample or library representing many elemental compositions. In addition to speeding up the sample preparation, the use of composition spread samples eliminates many sample-to-sample variations. The high density of information available on such a sample necessitates the development of high-throughput evaluation techniques to collect and organize the information. Sample preparation

of composition libraries can range from sequential deposition through physical masks [131] to the continuous gradients observed in depositions from physically separated elemental sources. In our research group, we have thus far employed the latter, using geometrically arranged sputter guns with different targets [30, 132, 133, 134]. In addition to sputtering, composition spreads have been prepared by pulsed laser deposition (PLD) [135], evaporation [136], and liquid mist chemical deposition [137].

In our research group, deposition of composition spreads has recently been documented for oxide films from 90° off-axis sputter guns with elemental [138] and ceramic [139] targets and for metals films from co-axial [140, 141] and slightly angled [142] sputter guns. High-throughput material characterization methods have been developed for for stress in a deposited film [143], for photoluminescence [138, 144], and for catalytic activity for the oxidation of methanol and other fuels [140]. Thus, deposition and characterization techniques within the group are thoroughly reviewed elsewhere. In this section, we briefly review the deposition of oxide films from 90° off-axis sputter guns with elemental targets, highlighting the important specifics for preparing and evaluating dielectric oxides.

There are a number of effects to keep in mind when preparing combinatorial samples and when evaluating their measurements. Of particular concern in evaluating dielectric materials is a low frequency polarization commonly observed in films deposited from an oblique source; this anomalous polarization and recovery of the 'normal' polarization by substrate biasing during deposition is discussed in Chapter 5.

Film thickness and elemental composition

In this section, we describe accurate measurements of film thickness and elemental composition. In particular, we discuss the deposition rate profile from a sputtering target perpendicular to the substrate. A single sputtering target yields a gradient in deposition rate with distance from the sputter source. Multiple co-sputtering sources yield a composite deposition rate; we will compare the composite deposition rate and the sum of individual deposition rates.

We define first the "deposition rate" as an atomic deposition rate, c, with units of atoms·area^{-1}·time^{-1}. We distinguish this from the thickness rate, t, with units of length·time^{-1}. From a single sputtering source, assuming no changes in density with thickness or crystal phase, these two rates are easily related by the density, ρ, [mass·volume^{-1}, or equivalently, mass·area^{-1}·thickness^{-1}] and the molecular weight, MW, [atoms·mass^{-1}], according to

$$c = t \times \rho \times MW. \tag{6.1}$$

For a simple oxide from a single target, therefore, the atomic deposition rate is easily evaluated from known constants and an optical measurement of film thickness. Deviations from full theoretical density are evident in low refractive indices.

The thickness rates are measured optically and fit to the functional form of

$$t = t_o \exp - \frac{\sqrt{(x - x_o)^2 + c(y - y_o)^2}}{d} \tag{6.2}$$

in which t is the thickness rate at a position (x, y) on the sample, (x_o, y_o) is related to the location of the sputter target, d is the decay length along the direction of the gun axis (the x-direction), c is the proportionality of the transverse decay along the y-direction.

Table 6.1: Thickness rates for individual sputter targets. The t_o is given from the closest edge of the substrate to the A or B sputtering target; the closest substrate edge is 17 mm from the target for Guns A and C and 6 mm from the target for Gun B.

Material / Power [W]	Sample number Sputter gun	t_o [nm·min^{-1}]	c_o [nmol·cm^{-2}s^{-1}]	d [mm]
Ta_2O_5 / 70	/ A	5.18	0.16	42.9
Ta_2O_5 / 100	08f09 / A	10.20	0.32	44.1
Ta_2O_5 / 30	/ C	0.21	0.01	31.3
GeO_2 / 30	07f148* / C	0.41	0.03	30.0
TiO_2 / 100	08f49 / B	9.26	0.81	38.2
HfO_2 / 60	08f27 / B	8.12	0.62	34.2
Nb_2O_5 / 80	08f52 / B	7.19	0.33	27.1
Dy_2O_3 / 40	08f53 / B	8.73	0.30	30.3
MoO_3 / 37	/ B	4.30	0.36	27.2

For a number of materials, thickness rates have been measured and the fits appear in Table 6.1. These rates are found to be very reliable within consecutive depositions, but may vary in the following deposition cycle several weeks later. The difference is likely to depend on exact placement of the targets and ground shields with respect to the substrate, the condition of the sputter target, and the exact impedances of the matching networks.

It is important to note that thicknesses are not additive when co-sputtering several targets. That is, we can not simply add the thickness rate profile of material A in sputter gun A to that of material B in sputter gun B to get the total thickness profile of a film of co-sputtered A and B. Rather, the co-sputtered ma-

terial is intimately, or atomically, mixed. We must expect, therefore, that the density and the packing structure of the intimately mixed A-B composite film may be different than the densities of either A or B or any weighted average of the two. This is widely observed in equilibrium structures and has been observed additionally in mixed Hf-Ti oxide thin films, prepared by CVD [22].

Rather than thickness, we make the assumption to first order that atomic deposition rates are additive. That is, we assume that the atomic deposition rate profile of a material A from a sputter gun A is independent of the atomic deposition rate profile of a material B from a sputter gun B. As a corollary, we have that the atomic deposition rate of the co-sputtered film is the sum of the independent atomic deposition rates. (We discuss caveats to this assumption, when we examine Ta-Ge oxide composition spreads in Section 6.2.)

6.2 TaO_x-GeO_x binaries

With the advent of high-k dielectrics and the continued scaling of semiconductor devices, the replacement of the silicon semiconductor channel with germanium is gaining traction [145]. Germanium is a superior semiconductor in terms of its carrier mobility; however, germanium oxide is not a stable dielectric. Rather, GeO_x is water soluble. The high quality and stable interface between silicon and its oxide SiO_2 is clearly the better choice. Since high-k materials are now commonly used instead of silicon oxide, however, the argument loses strength. Channels of SiGe are becoming common, and development in the field was recently review by Reference [146]. Gate stacks of 30 hafnium oxide or ZrO_2 on 11 GeO_xN_y have been demonstrated on germanium nMOSFETs;

the optimized GeO_xN_y layer was not water soluble, though it did dissolve in HF [147]. Gates of amorphous germanium nitride have also been demonstrated on germanium semiconductors; Ge_3N_4 is water insoluble and has a dielectric constant of 9.5 [148, 149]. In the past year, Otani *et al.* [149] have reported on Ta_2O_5/GeN_x gate dielectric stacks with a capacitance equivalent thickness of 4.3 nm and low interface trap density.

The stable germanium nitride gate and germanium oxynitride interfacial layers indicate that small amounts of germanium oxide or nitride in the high-k material may benefit the interface with the germanium semiconductor channel. In this section, we incorporate germanium oxide into a Ta_2O_5 host to examine its effect on dielectric properties and film stability. As in previous sections, we choose to investigate the dielectric bulk properties by examining a MIM structure with noble electrodes, thus neglecting the interfacial properties of these materials with a semiconductor.

6.2.1 Film composition and resputtering

In Ta-Ge oxide binaries, we observe significant discrepancy between composition measurements by wavelength dispersive spectroscopy (WDS) and the compositions expected by an addition of the atomic deposition rates from each gun independently [112]. In Figure 6.1, we present the elemental composition for a TaO_x-GeO_x binary, deposited from facing tantalum and germanium targets on a biased substrate (10 W/5 W/-95 V). The tantalum target is powered to 100 W RF, while the germanium target is powered to 30 W. The targets are separated by 112 mm. The individual deposition rates were determined from reflec-

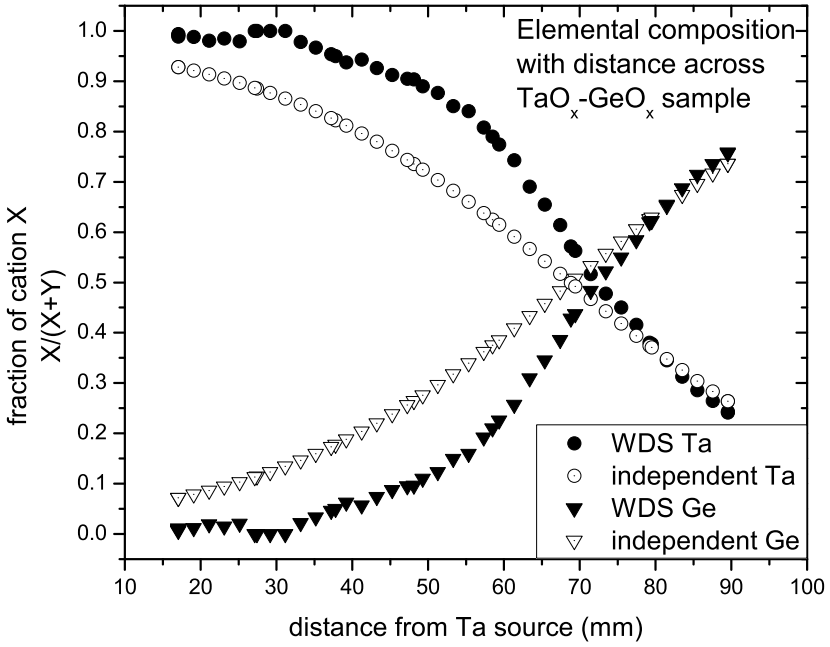

Figure 6.1: Concentration of TaO_x and GeO_x vs. distance from the Ta target (100 W). The substrate is a 3 inch (75 mm) wafer, while the Ge target (30 W) is at 112 mm. Composition is given both by WDS and by the addition of individual deposition rates. WDS sample 08F55; independent Ta_2O_5 optical measurements from 08f09?, GeO_2 from 07F148.

tometry measurements of a thick Ta_2O_5 film deposited on an unbiased substrate (08f09) and of a thick GeO_2 film deposited on a biased substrate (07f148).

The composition closest to the tantalum source is found to be Ge-poor, compared to the compositions expected from an independent deposition assumption. In contrast, close to the germanium source, we find that the composition from WDS is very similar to that expected from two independently acting sources.

These observations are consistent with the resputtering observed by Gregoire, *et al.* [124, 125]. The authors suggest that atoms arrive at the film surface as expected from independent sources, but that the atoms may be resputtered from the film, primarily by neutral argon atoms reflected from the targets. The reflected argon preferentially resputters the more easily sputtered atom (usually the element with the lower heat of sublimation). The resputter coefficients defined by Gregoire *et al.* indicate that while argon reflected off the tantalum target resputters significant quantities of germanium, very little tantalum is resputtered by argon reflected off the germanium target. (From their online resputter calculator [150], $\Gamma_{Ge,Ta} = 0.58$ for the tantalum target powered to 300 V, while $\Gamma_{Ta,Ge} = 0$ for resputtering from argon reflected off a germanium target powered to 200 V. For reference, Γ values are non-negative and generally much less than 1.)

6.2.2 Optical dielectric constants of TaO_x-GeO_x binaries

Resputtering of atoms once deposited on the film raises questions not only of the film composition but also of the film thickness–an important measurement in evaluating dielectric materials. In this section, we also consider both resputtering and densification caused by the argon bombardment induced with an applied substrate bias.

We prepared three samples of binary TaO_x-GeO_x spreads at three different substrate biases; RF power to the tantalum and germanium targets were 100 W and 30 W, respectively. Powers and voltages for the substrate and the tantalum target are given in Table 6.2 for these three and the WDS sample (08f55). To

Table 6.2: Power to the tantalum target and substrate for TaO_y-GeO_y samples used to determine composition, deposition rate, and refractive index

Sample	Ta forward power (W)	Ta DC bias voltage (V)	Substrate forward / reflected power (W)	Substrate DC bias voltage (V)
08f55	100	-320	11/5	-95
08f163	100	-260	0/0	+8
08f164	100	-260	12/2	-70
08f165	100	-260	7/1	-40

ease analysis of the optical measurements, the samples were sputtered directly on bare silicon wafers to a thickness of 300-450 nm in 55 minute depositions. Photographs of the samples are given in Figure 6.2. By visual inspection, we observe that the film deposited on the unbiased substrate is significantly thicker than the films deposited on biased substrates and that thickness–particularly in the region closest to the germanium target during deposition–decreases with increasing substrate bias.

To probe the thickness change more quantitatively and to tease out the related changes in refractive index, we measured the films deposited on the unbiased and more highly biased substrates in the Woollam spectroscopic ellipsometer. Each film was measured at ten different positions on the substrate at wavelengths of light from 300 nm to 1000 nm; six positions were measured at an angle of incidence of 70°, while the remaining four were measured at 65, 70, and 75 °. The results were modeled by a bilayer structure on a silicon wafer: Cauchy layer/1 nm SiO_2/silicon substrate. The fit parameters from the Cauchy layer are the thickness and the A and B parameters of the refractive index in

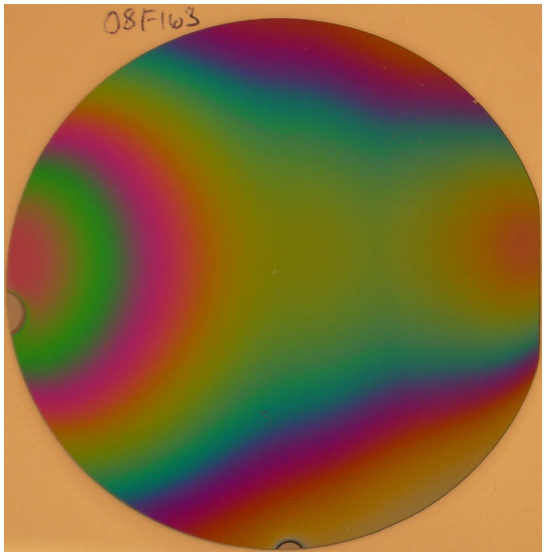

(a) Deposited without substrate bias

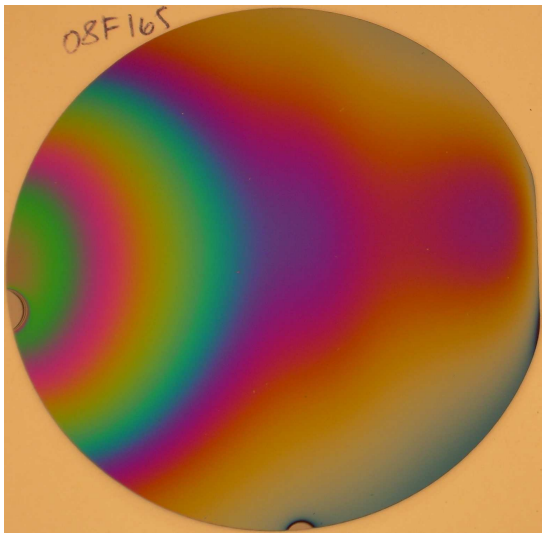

(b) Deposited with light substrate bias (7 W, -40 V dc)

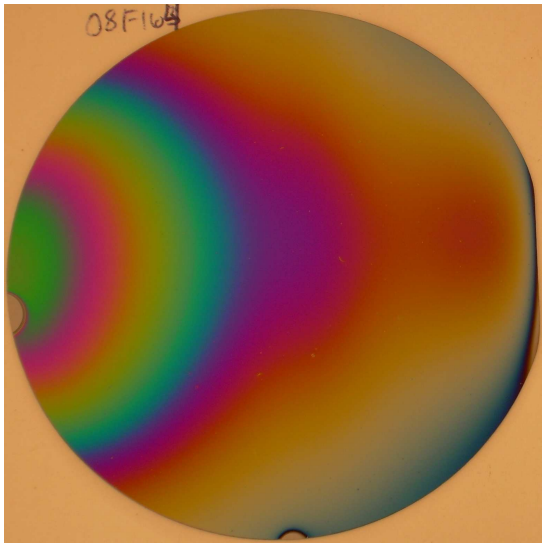

(c) Deposited with substrate bias (12 W, -70 V dc)

Figure 6.2: Binary spreads of TaO_xGeO_x deposited without substrate bias and with light and heavy substrate biases. In each image, the tantalum source was to the left, the germanium to the right; each wafer is 3" in diameter. Samples 08f163, 08f165, and 08f164, respectively.

the Cauchy relationship (Equation 3.1 in Chapter 3). As we did in Chapter 3, we take the A value as the refractive index at long wavelengths, far from any adsorption edge.

In Figure 6.3, we plot the refractive index and deposition rate of the film as a function of distance from the tantalum source. We find that the film deposited without substrate bias has a higher deposition rate and lower refractive index. The deviation in deposition rate between films deposited with and without substrate bias is particularly dramatic on the nominally germanium-rich region, but is measurable even on the region of the film closest to the tantalum source during deposition.

It would be interesting to investigate the difference in composition between these two films at different regions of the film. Such a measurement would shed light on the relative resputter rates due to the argon bombardment induced with the substrate bias. Unfortunately, these samples are not directly comparable to the film used for WDS composition analysis, since the tantalum target used for these depositions is not the same as that used in Sample 08f55 for WDS–notice the difference in DC self biases on the tantalum targets in Table 6.2. The response of the substrate to biasing has also changed, with a lower fraction of RF power reflected and a lower induced bias voltage for a given power.

We gain some insight into the elemental composition by comparing the indices of refraction. As we have discussed in Chapter 3, the optical index of refraction depends on both the density of the material and its elemental composition by measuring the polarizability of electrons clouds at the frequencies of visible light. As such, the square of the refractive index is the optical dielectric constant, $\varepsilon_r \sim n^2$. The refractive index of dense Ta_2O_5 is found to be 2.10-2.15 at

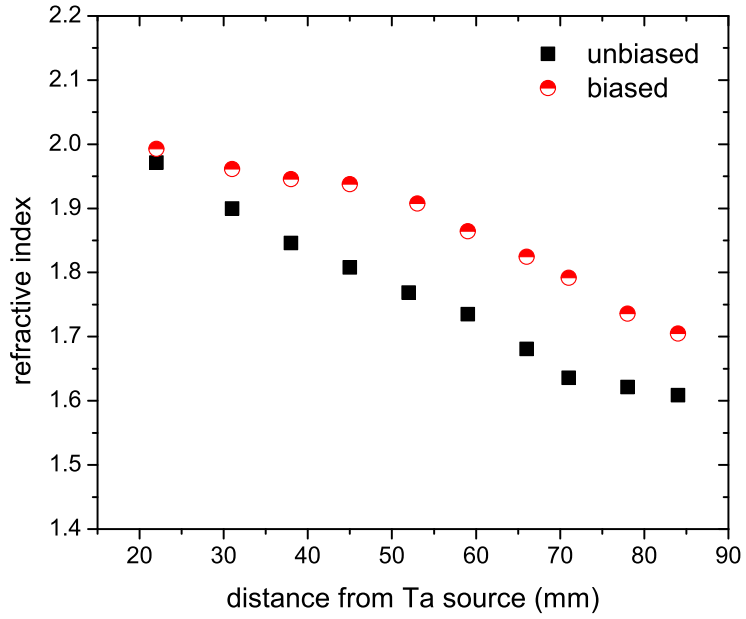

(a) Refractive index

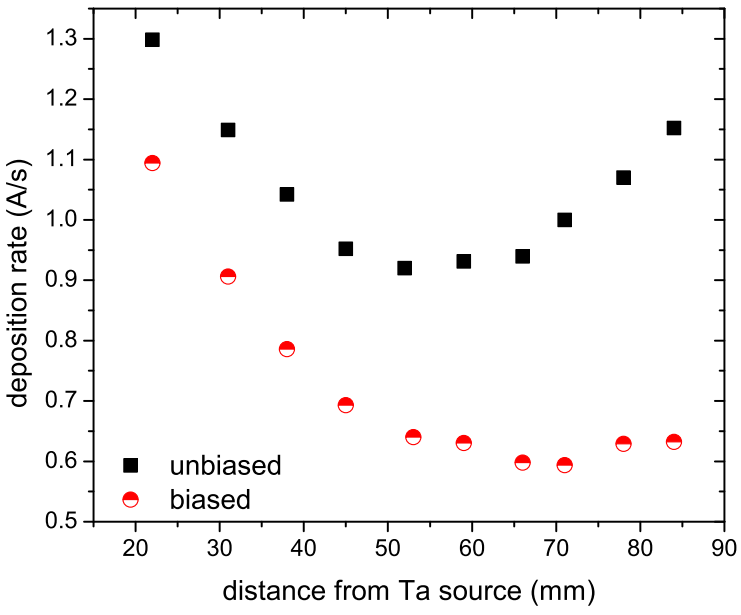

(b) Deposition rate

Figure 6.3: Refractive index and deposition rate of binary spreads of TaO_x-GeO_x. Sample 08f163, 08f164.

wavelengths of light greater than 500 nm [151]. In contrast, the refractive index of a sputtered thin film of GeO_2 is 1.6 at λ = 546 nm [152], indicating a lower polarization density of electrons. We expect a decrease in refractive index with increasing germanium content (increasing distance from the tantalum source); this is observed for films deposited on both biased and unbiased substrates. While both films have a refractive index of ~1.97 in the most tantalum-rich region, however, the refractive index of the film deposited without substrate bias decreases further and more rapidly with increasing distance from the tantalum source. The decrease in refractive index is attributed to greater incorporation of GeO_2 on unbiased substrates. The film deposited on the biased substrate is subject to greater argon ion bombardment and a resulting loss of GeO_2 due to resputtering. The loss of GeO_2 is also observed in the decreased thickness of the film deposited with substrate bias.

We conclude that resputtering is possible from the argon bombardment induced with the substrate bias. While resputtering due to argon reflected from the sputtering targets is more significant close to the tantalum target, however, resputtering due to bombarding argon accelerated in the substrate bias field is significant throughout the film and causes significant loss of film thickness close to the germanium target.

The results here indicate that thickness and composition must be measured for each binary or ternary co-deposition and in general can not be known by assuming deposition profiles from independent sources. Also, because of difficulties in performing WDS and ellipsometry on thin oxide films deposited on their base electrodes, we suggest that a similar film with a thickness of several 100s nm be deposited on a bare silicon wafer with an applied substrate bias.

These films have not been prepared for the films for which dielectric measurements are presented in this chapter; the neglect requires us to make assumptions about film thickness and composition that could be avoided by measuring a similar film.

6.2.3 Electronic dielectric constants of TaO_x-GeO_x binaries

While the refractive index is sensitive to only to the electronic polarizability and molecular density, the dielectric constant at the operating frequency of devices (10^3-10^9 Hz) is sensitive to the polarization of both electrons and ions, as well as the density. In this section, we calculate the dielectric constant as a function of composition in TaO_x-GeO_x binary composition spreads.

Figure 6.4 gives the dielectric constant and loss tangent at each frequency decade from 100 Hz to 1 MHz for capacitors on a TaO_x-GeO_x binary composition spread deposited on a biased substrate. Power to the tantalum and germanium targets are 100 W RF and 30 W RF, respectively, while the substrate is biased to 20 W/11 W/-100 V.

The dielectric constant is calculated from the measured capacitance and an assumed thickness. The thickness is taken from the sum of measured deposition rates from the same independent sources used in Figure 6.1. The GeO_2 deposition rate was measured by reflectometry on a thick film on silicon, deposited with an 10 W (-95 V dc) substrate bias (Sample 07f148); as such, the deposition rate takes into account resputtering due to bombarding argon in the bias field, but neglects resputtering close to the tantalum target due to reflected neutral argon. The tantalum deposition rate is measured by reflectometry of thin films

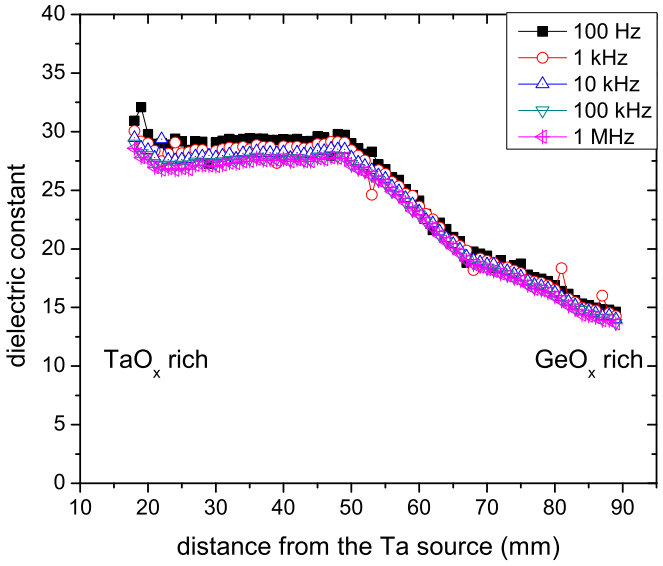

(a) Dielectric constant

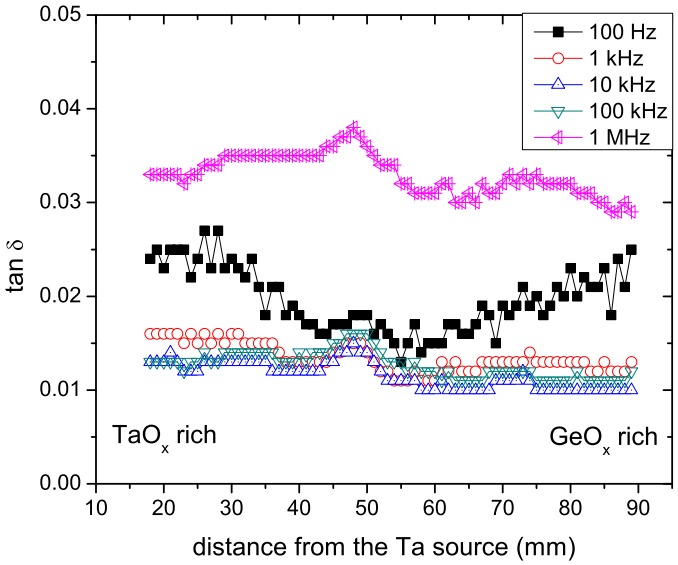

(b) Dissipation

Figure 6.4: Dielectric constant and loss tangent for binary spread of TaO_x-GeO_x as a function of distance from the tantalum source. Sample 08f45.

deposited without substrate bias (Sample 08f09). The last assumption is that the deposition rates in terms of thickness per time add directly. This assumption is not strictly true; as we have noted, atomic deposition rates add (in the absence of reflected argon resputtering). However, the sum of thickness deposition rates is likely only to overestimate the thickness, since the density of a mixture–particularly of a mixture of two different sized atoms such as tantalum and germanium–is likely higher than the constituent oxides. Thus all of our assumptions overestimate the film thickness, leading to a corresponding overestimation of the dielectric constant.

In Figure 6.4, we find that the dielectric constant decreases with increasing distance from the plane of the tantalum target, approaching the dielectric constant of Ta_2O_5, $\varepsilon_r \sim 25$, in regions of the film deposited close to the tantalum source and that of GeO_2, $\varepsilon_r \sim 8$, in regions of the film deposited close to the germanium source. The decrease in dielectric constant is not linear with distance, but then neither is elemental composition. The loss tangent is low, ≤ 0.035, with limited dispersion with frequency. It decreases slightly with increasing distance from the tantalum sputter target.

Figure 6.5 replots the dielectric constant and loss tangent from Figure 6.4 versus the germanium content measured by WDS on Sample 08f55, prepared with similar deposition parameters. In plotting the dielectric constant, we also give a linear interpolation between the dielectric constants of its end members, Ta_2O_5 and GeO_2. We see that the linear interpolation is a good fit from 35% to 85% germanium, but that at lower germanium contents, the dielectric constant is enhanced above the linear interpolation. We also see a plateau in dielectric constant extending to 12% Ge, followed by a linear decrease to 35% Ge. Beyond

35%, a more gradual linear decrease in dielectric constant occurs, according to the linear interpolation of end members.

Understanding the two regions of dielectric constant at <35% Ge requires further investigation. We notice that because of significant Ge resputtering close to the tantalum target, a substantial fraction of the ε_r = 26 plateau on the plot versus position (Figure 6.4) collapses down to the pure Ta_2O_5 axis when dielectric constant is plotted versus germanium content (Figure 6.5). Variations in resputtering could lead to variations in thickness or composition that may account for an enhancement of the dielectric constant above that expected; however, these effects are unlikely to change abruptly, as the dielectric constant does at twelve and 35%.

A plateau in dielectric constant even with an impurity concentration of twelve percent is not unheard of. Li *et al.* [22] observed a saturation of the dielectric constant in their HfO_2-TiO_2 mixed dielectrics at >62%Hf to ε_r = 23, the dielectric constant of HfO_2. We suggest, however, that the plateau requires coordination of opposing effects, for example, a simultaneous increase in molar density and decrease in polarizability due to the substitution of less polarizable but smaller germanium atoms in a tantalum oxide matrix.

A potential source of abrupt changes in dielectric constant with composition is formation of a crystalline phase. We performed x-ray diffraction on the WDS sample (08f55) at three different positions on the film and found no evidence of crystallization. A related possibility is a change in local coordination that does not manifest itself in crystallization (long range coordination) without intentional heating of the substrate. This type of structure can be probed by Raman, FTIR, or soft x-ray absorption techniques, such as XANES or EXAFS.

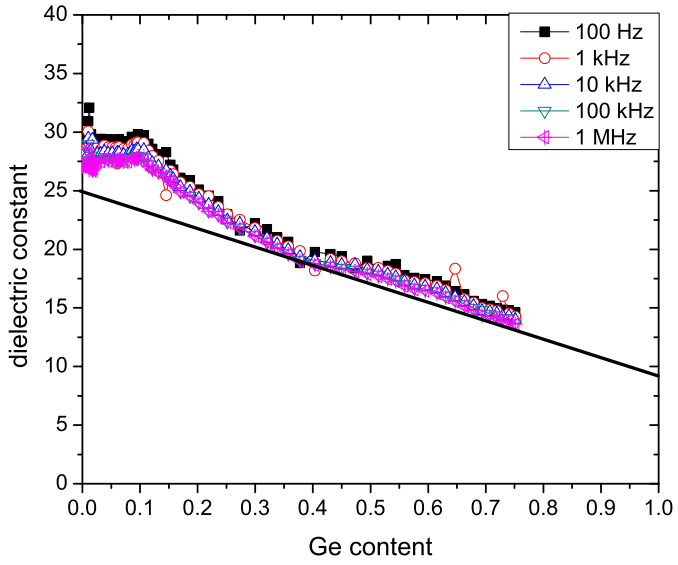

(a) Dielectric constant

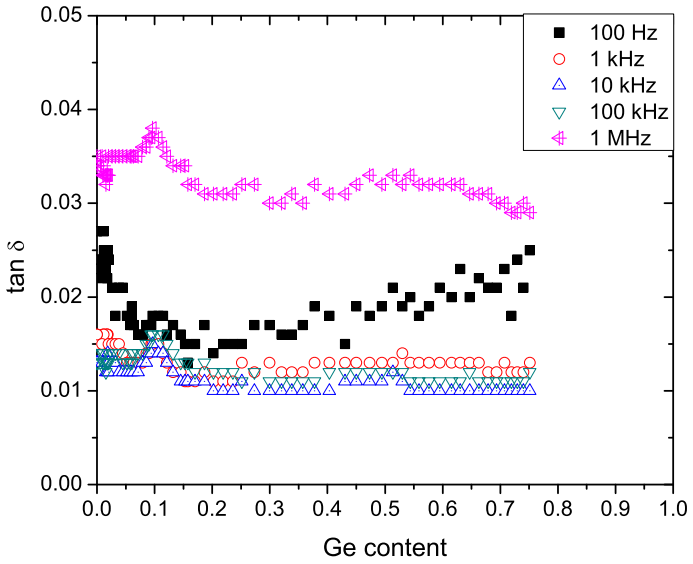

(b) Dissipation

Figure 6.5: Dielectric constant and loss tangent for binary spread of TaO_x-GeO_x as a function of Ge content. The black line in (a) is a linear interpolation from the dielectric constant of pure Ta_2O_5 to that of pure GeO_2. Sample 08f45.

6.2.4 Solubility of Ge-containing oxides

A significant drawback in using germanium channels is that germanium oxide is water soluble and therefore may not be robust under common etching or cleaning techniques. We tested the stability of our TaO_x-GeO_x binaries by immersing a sample in water. The samples chosen had the same composition as that in Figure 6.1. Both were deposited on a base electrode of evaporated platinum on a chromium sticking layer and had platinum top electrodes. The samples were submerged in (initially) deionized water for one hour at room temperature. No dissolution was observed in either sample.

Additionally, one of the samples was remeasured for capacitance and dissipation after the water bath. We find no change in the dielectric results, as shown in Figure 6.6. Remarkably, the material is as much as 75% germanium oxide, but is stabilized by the tantalum oxide. To within the resolution of this test, there is no detrimental dissolution of material. Remeasuring the composition by WDS would be a more thorough demonstration of this claim, but the samples such as these that are prepared for electrical measurements are not sufficiently thick for straightforward WDS analysis. The tantalum Mα peak at 1.71 keV overlaps with the Kα silicon peak (1.74 keV), such that these elements are not easily resolved for films thin enough that the electron beam penetrates the silicon.

To assure ourselves that germanium oxide is in fact water soluble, a pure germanium oxide film deposited on a platinum/chromium base electrode was also subjected to the same test. The film (07f148) had a thickness gradient of 250 nm to 30 nm and dissolved entirely within 10 seconds.

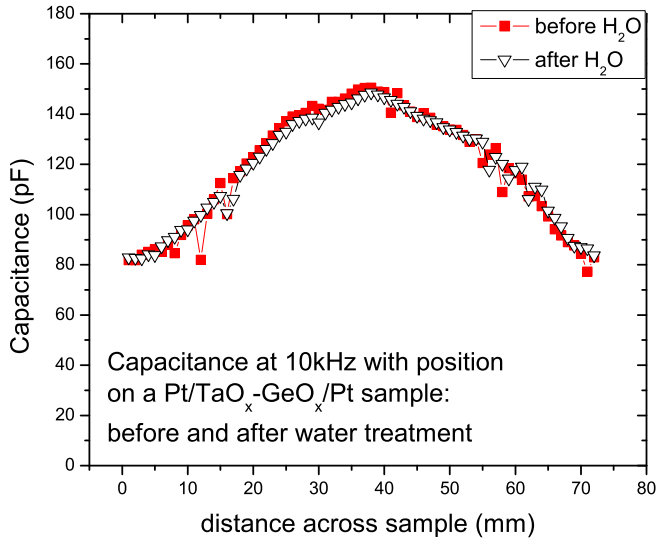

(a) Capacitance at 10kHz

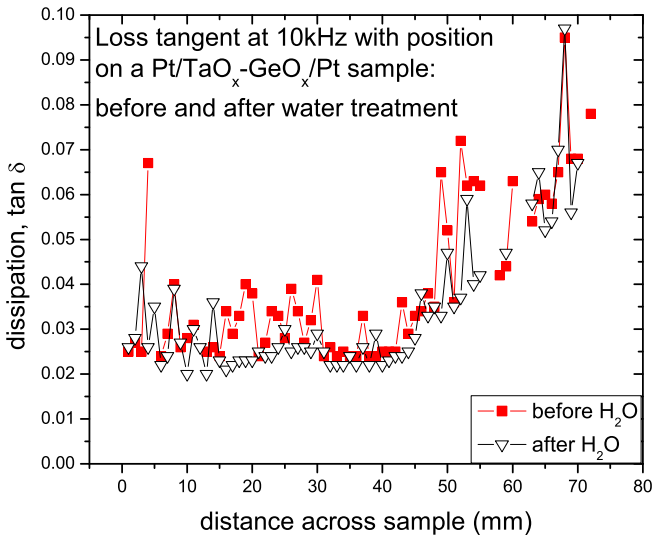

(b) Loss tangent at 10kHz

Figure 6.6: Column average of (a) capacitance and (b) dissipation measurements before and after a 1 hour immersion in water. The capacitors are Pt/Ta_2O_5-GeO_2/Pt composition spreads. Sample 08f43.

6.3 Conclusions and analysis of co-sputtered oxides

Co-sputtering of elemental oxides has the potential to enable rapid exploration of composition space in the search for candidate dielectric materials. The analysis of co-sputtered films, however, is complicated by the resputtering potential of the material system under investigation. Resputtering, like sputtering, occurs due to bombarding argon species. These species may be either Ar^0 atoms reflected off a sputtering target or Ar^+ ions accelerated in the electric field of the substrate bias. Materials systems that contain an easily sputtered element such as germanium are particularly susceptible to resputtering by both argon species. Sputtering from targets such as tantalum that strongly reflect argon atoms make a materials system additionally sensitive to resputtering by reflected argon.

We have found that resputtering is an important factor in co-sputtered TaO_x-GeO_x. Since the effect of resputtering varies strongly with plasma density within the chamber, its effect on the elemental composition with position is not easily modeled. Instead elemental composition must be measured for each set of deposition conditions. In contrast, elemental composition with position can be evaluated theoretically in materials systems whose constituent elements are not easily resputtered by addition of independent deposition rates.

CHAPTER 7

SUMMARY AND FUTURE OUTLOOK

Throughout this dissertation, we have found that the properties of thin film oxides, like all materials, are highly process dependent. In the specific case of this work, we have investigated the dielectric properties of sputter deposited thin film oxides. The dielectric properties of greatest interest were the dielectric constant, dispersion, and leakage current behavior. We have demonstrated that these properties are closely coupled to the material density, the structure and density of inhomogeneities, and the inclusion of intentional and adventitious impurities. The sputter processing parameters that effect these structures and their associated dielectric responses include temperature; sputter geometry, including the orientation and spacing of sputter targets with respect to the substrate; bombardment of the growing film by energetic and/or charged species; sputtering gases and pressures; choice of base electrode materials.

In particular, we have found that the complex dielectric oxide $Zr_{0.2}Sn_{0.2}Ti_{0.6}O_2$ exhibits a higher dielectric constant ($\varepsilon_r \sim 55$) when deposited at substrate temperatures of 150 to 250 °C than at lower or higher substrate temperatures. Remarkably, the high dielectric constant material remains x-ray amorphous and does not exhibit an increase in density as probed by optical refractive index. Future investigations on this material could include a probe of local coordination, e.g. Raman spectroscopy, FTIR, or XAFS.

We have prepared a high quality dielectric $Ti_{0.77}Dy_{0.23}O_{1.85}$ by reactive sputter deposition in an Ar/O_2 atmosphere on unheated substrates. The material has a $\varepsilon_r \sim 25$, low dissipation, low leakage currents, and low dispersion of the dielectric constant with measurement frequency. In this material system, we

find that dielectric properties are sensitive to the choice of base electrode metals and to damage caused by the bombardment of energetic species during reactive sputtering. Future and continuing work may include the integration of the reactively sputtered material in silicon devices.

Preparation of the same dielectric $Ti_{0.77}Dy_{0.23}O_{1.85}$ by *in situ* thermal oxidation of a sputtered metal film results in an oxide that is subject to an additive defect polarization mechanism. This polarization mechanism warrants further analysis, since it must be eliminated before thermally oxidized $Ti_{0.77}Dy_{0.23}O_{1.85}$ can be integrated into any useful application. Also, identifying the defect polarization mechanism in $Ti_{0.77}Dy_{0.23}O_{1.85}$ may lead to insights into what materials systems are promising candidates for preparation by post-deposition thermal oxidation.

The effects of ion bombardment are analyzed in some detail in the final two chapters. We compared the dielectric constant, particularly at low frequencies, of Ta_2O_5 deposited on an on-axis substrate to that deposited on off-axis substrate. While the former substrate is subject to uncontrolled bombardment by electrons and negatively charged oxygen ions, the latter experiences very little bombardment. We find that Ar^+ ion bombardment can be controllably increased in the off-axis substrate with the application of an RF bias and the negative self-bias DC voltage developed. Induced ion bombardment is critical to depositing high quality dielectrics from oblique sources. Without it, films develop a void structure in which hopping conduction along adsorbed water molecules contribute to a low frequency loss polarization mechanism that masks the intrinsic dielectric properties of the oxide.

We implemented this substrate bias during co-sputtering of TaO_x-GeO_x binaries. The variation of dielectric constant with composition has three regions of behavior. The dielectric constant of the most germanium rich material, 35% to 85% cation germanium, follows a linear interpolation from the dielectric constant of GeO_2 to Ta_2O_5. At lower germanium contents, however, the dielectric constant is enhanced over the linear interpolation; at less than twelve cation percent germanium, the dielectric constant is that of Ta_2O_5 and decreases linearly from 12% to 35%. Analyzing the bonding structure and density associated with the plateau in dielectric constant at low germanium content is an important further investigation.

Resputtering is found to be a significant effect in co-sputtered and substrate biased films. We have demonstrated that resputtering of the material off the deposited film is effected both by neutral argon reflected off a powered sputtering target and by Ar^+ ion bombardment accelerated in the field of the substrate bias. The extent of these effects depends strongly on the sputtering yield and argon reflection of the constituent elements.

APPENDIX A

DERIVATION OF AC CONDUCTIVITY IN POROUS OXIDES, USING SILLARS' MODEL

Maxwell-Wagner polarization refers to the observed polarization due to interrupted conducting inhomogeneities within an insulator. In particular, Maxwell considered inhomogeneities oriented parallel to the electrodes, while Wagner considers spherical inhomogeneities. In 1937, R. W. Sillars [113] published an analysis of Maxwell-Wagner polarization in the case of spheriodal inhomogeneities aligned along the electric field axis with the goal of more accurately finding the magnitude and frequency of the maximum dissipation. In this appendix, we apply Sillars' analysis to the nanoporous structure of insufficiently bombarded Ta_2O_5, deposited from a 90° off-axis sputter target, as discussed in Chapter 5.

Sillars imagined a geometry of spheriodal semi-conducting inclusions in an insulator. The inclusions are assumed to have an axis of length a aligned with the electric field and two equal axes of length b perpendicular to the field. His analysis is consistent with his own experimental results on the capacitance and loss of a suspension of water droplets in an insulating wax.

More recently, Khanna and Nahar [115] have applied Sillars' analysis to thick film humidity sensors based on anodized alumina. Anodized alumina is characterized by long, thin pores with well-defined size and connectivity to the environment (see, e.g., Ref. [153]). In the case of humidity sensors, the semiconducting inclusion is in the form of adsorbed or liquid water within the pores. To find the volume fraction of water in the pores, we consider first the Kelvin

radius:

$$r_k = \frac{2\gamma M_w}{\rho RT \log(P_s/P)} \tag{A.1}$$

in which γ is the surface tension of water (= 72.75 dyn cm^{-1}), M_w and ρ are its molecular weight and density, respectively, and P and P_s are the vapor pressure of water at ambient and at saturation, respectively [120]. The ratio P/P_s is also known as the relative humidity. Capillary condensation occurs in pores with radii smaller than the Kelvin radius; condensed water is subject to electrolytic conduction.

The pore diameter for our lightly bombarded Ta_2O_5 films is estimated to be 2.5 nm. For this r_k, capillary condensation is expected at relative humidities greater than 65%. Comparable relative humidities are possible in ambient, but not in the vacuum storage. Chemisorbed and physisorbed layers are likely at all humidity levels, and a pore of 2.5 nm diameter can accommodate up to three monolayers of adsorbed water [118]. Conduction in adsorbed layers is via proton conduction in the Grotthus mechanism [121] or H_3O^+ conduction [122]. The conductivity within the "semi-conducting" pores depends strongly on the humidity, since the amount of water in the pores controls the type and concentration of charge carriers.

To capture the structure of the semi-conducting inclusions, Sillars defined a parameter l_a, related to the eccentricity e:

$$l_a = 4\pi(\frac{1}{e^2} - 1)(\frac{1}{2e}\ln(\frac{1+e}{1-e}) - 1) \tag{A.2}$$

with e given by

$$e = \sqrt{1 - \frac{b^2}{a^2}}. \tag{A.3}$$

We note that these expressions for the structures of inclusions are dimensionless; they describe only the shape of the inclusion, not size. For the pores discussed

in Chapter 5, we have $a = 10$ nm and $b = 2.5$ nm, such that $e = 0.968$ and $l_a = 0.9476$. For simplicity and parallelism with Sillars' treatment, we define a parameter $n = 4\pi/l_a$; in this case, $n = 13.3$. Note that for a sphere, $n = 3$; for $n < 3$, the unique axis a aligned along the electric field is shorter than the equal axes, b.

The inhomogeneous dielectric is modeled as an insulating matrix of dielectric constant ε_1' with spheroidal inclusions of dielectric constant ε_2' and conductivity σ_2. The imaginary part of the inclusions' dielectric constant is defined by the conductivity, $\varepsilon_2'' = 4\pi\sigma_2/\omega$, in which ω is the frequency of the electric field.

Values can not be measured directly for ε_1', ε_2', and σ_2. However, the dielectric constants of water, air, and Ta_2O_5 are well-studied, and we assume that these values describe well the dielectric response of the pores and matrix, respectively. In the case of water-filled pores, $\varepsilon_2' = 80$, while for air-filled pores, $\varepsilon_2' = 1$. The dielectric constant of the matrix is that of Ta_2O_5, $\varepsilon_1' = 23$. With these assumptions and measurements of capacitors formed from these inhomogeneous materials, we aim to deduce information about σ_2, the conductivity of charge carriers within the pores.

At frequencies high enough to freeze out conductivity in the pores, the dielectric constant ε_∞ of the inhomogeneous composite dielectric material is given by

$$\varepsilon_\infty = \varepsilon_1'(1 + \frac{qn(\varepsilon_1' - \varepsilon_2')}{\varepsilon_1'(n-1) + \varepsilon_2'}) \tag{A.4}$$

in which q is the volume fraction of inclusions. In our case, we estimate a porosity of $q = 0.06$ by considering a dense 20 nm diameter column surrounded on 60% of its circumference by a 2 nm thick void. For an air-filled void, we calculate a $\varepsilon_\infty = 21.6$. For a water-filled void, $\varepsilon_\infty = 25.9$.

In accord with Wagner's analysis, we define

$$N \equiv q\frac{n^2\varepsilon_1'}{\varepsilon_1'(n-1)+\varepsilon_2'} \tag{A.5}$$

and

$$\tau \equiv \varepsilon_o\frac{\varepsilon_1'(n-1)+\varepsilon_2'}{4\pi\sigma_2} = \frac{\varepsilon_1'(n-1)+\varepsilon_2'}{\omega\varepsilon_2''}. \tag{A.6}$$

We notice that N is a dimensionless quantity which depends on the fractional volume q of the inhomogeneity, while τ depends on its conductivity and has units of time. We have $N = 0.857$ and $N = 0.670$ for air and water-filled inclusions, respectively.

By calculating the electric potential and power loss in one of these spheroids, Sillars finds an inferred dielectric constant of the composite material of

$$\varepsilon' = \varepsilon_o\varepsilon_\infty + \varepsilon_o\frac{\varepsilon_1'N}{1+\omega^2\tau^2} \tag{A.7}$$

and

$$\varepsilon'' = \varepsilon_o\frac{\varepsilon_1'N\omega\tau}{1+\omega^2\tau^2}. \tag{A.8}$$

Since the loss tangent is the experimentally measured quantity, he also gives

$$\tan\delta = \frac{\varepsilon''}{\varepsilon'} = \frac{N\omega\tau}{N+(1+\omega^2\tau^2)(\varepsilon_\infty/\varepsilon_1')}. \tag{A.9}$$

In Figure A.1, we use Equation A.9 and the relationship between τ and σ_2 (Equation A.6) to plot the accessible $\tan\delta$ values for inclusions of four different aspect ratios, $a : b$. In this plot, we choose to consider a material with a porosity of 6 % with water filled pores. The loss tangent is plotted as a function of the conductivity σ_2 of charge carriers within the pores, assuming a measurement frequency of $\omega = 1$ kHz. We find, as Sillars did, that the highest loss tangents are accessible only for pores elongated along the electric field direction.

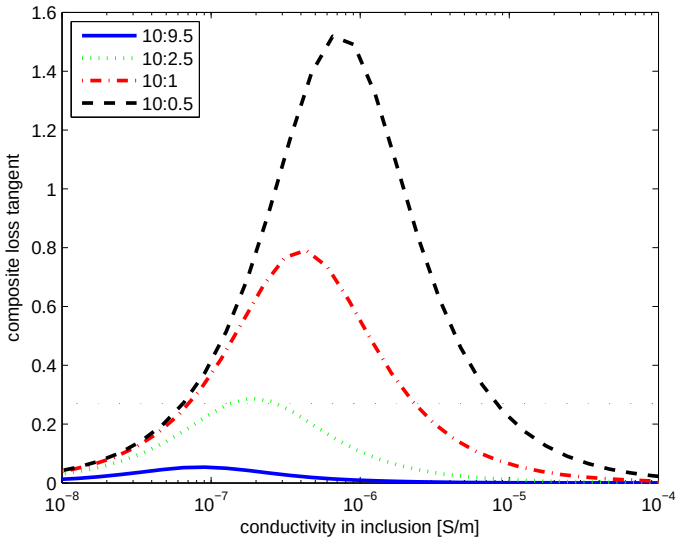

Figure A.1: Loss tangent versus conductivity, a la Sillars, at 1 kHz.

Similarly, in Figure A.2, we use Equations A.6 and A.7 to plot the accessible ε_r values at 1 kHz for composite films of the same inclusions. Again, we find that higher inferred dielectric constants are accessible for elongated pores than spherical ones. Figures A.1 and A.2 are found by assuming a pore shape and density, as well as the dielectric constants of the pore and the matrix, but do not rely on information about the conductivity within the pore nor dielectric measurements of the composite material.

We compare the accessible ε_r and $\tan\delta$ values to the ε_r and $\tan\delta$ values measured for water filled $Ag/Ta_2O_5/TiN$ capacitors formed from Ta_2O_5 deposited 90 ° off-axis without substrate bias (data in Figure 5.10). At 1 kHz, the $Ag/Ta_2O_5/TiN$ capacitors had a $\varepsilon_r = 165$ and a $\tan\delta = 0.27$. The conductivity σ_2 within the pores necessary to effect this high loss factor varies strongly with the aspect ratio of the semiconducting inclusions. For inclusions such as those observed in our TEM images with aspect ratios of 10:2.5, the conductivity

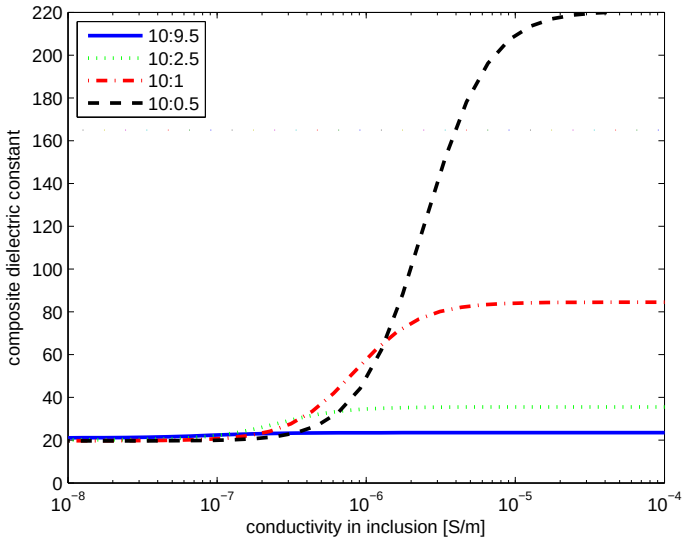

Figure A.2: Dielectric constant versus conductivity, a la Sillars, at 1 kHz.

within the inclusions should be 2×10^{-7} S/m. For longer inclusions, we notice that there are two conductivities that could give rise to the observed loss tangent; for an inclusion with an aspect ratio of 10:1, approximate conductivities of either 7×10^{-8} S/m or 3×10^{-6} S/m would give rise to the same loss tangent. In practice, however, we choose to consider only the lower of the two conductivities by noting that loss tangents should rise with increasing conductivity within the pore.

Sillars additionally considered a Gaussian distribution of the logarithms of the conductivities inside inclusions; the wider this distribution, the wider the peak in $\tan\delta$ [113]. We apply the same argument to the breadth of the dissipation peak seen in Figure 5.10.

To explain the observed enhancement to the dielectric constant, $\varepsilon_r = 165$, Sillars' analysis suggests that the dielectric response must be attributed to inho-

mogeneities with a $a : b$ ratio of greater than 10:1. It would seem then that the enhanced dielectric response is only possible with voids of a higher aspect ratio (longer and thinner) than are observed in the HRTEM images. However, such voids (say, 10 nm deep and 0.5 nm wide) are undoubtedly also present in our films. While not as easily observed in the microscope, they are more effective in raising the dielectric constant and loss tangent.

The dielectric response observed in $Ag/Ta_2O_5/TiN$ capacitors has a pronounced frequency dependence. We anticipate that the AC conductivities within the inclusions are likewise a strong function of frequency. In Figure A.3, we replot the accessible dielectric constants and loss tangents at 1 kHz and at 100 kHz. We again assume a 6 % porosity with semiconducting inclusions of the same four aspect ratios. The accessible range of dielectric constants remains the same as in Figures A.1 and A.2 since the range depends only on the geometry and density of inclusions. However, the AC conductivities required to effect these dielectric constants shift to higher values. At 100 kHz to observe a $\tan\delta = 0.27$ for 6 % volume of 10:2.5 inclusions, the conductivity in the pores would have to be 2×10^{-5} S/m, 100 times larger than getting the same $\tan\delta$ at 1 kHz.

In Figure A.4, we present the AC conductivities calculated from (consistent with) measurements of $Ag/Ta_2O_5/TiN$ capacitors of both the dielectric constant, using Equation A.7, and the loss tangent, using Equation A.9. In this case, we assume an $a : b$ ratio of 10:1. Missing conductivities indicate that the dielectric constant measured at this frequency could not be explained with this simple model. The conductivity is found to increase with frequency, as $\sigma = \sigma_o \omega^s$ with $s = 0.67$ based on dielectric constant results and $s = 1.0$ based on dissipation

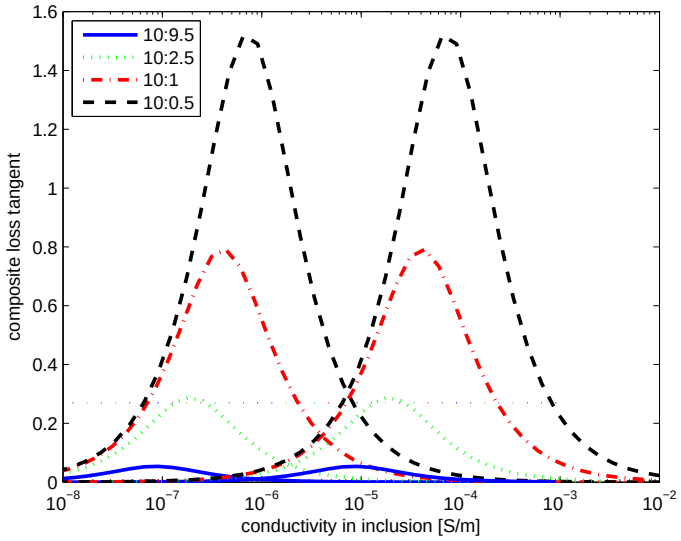

(a) Loss tangent of composite film

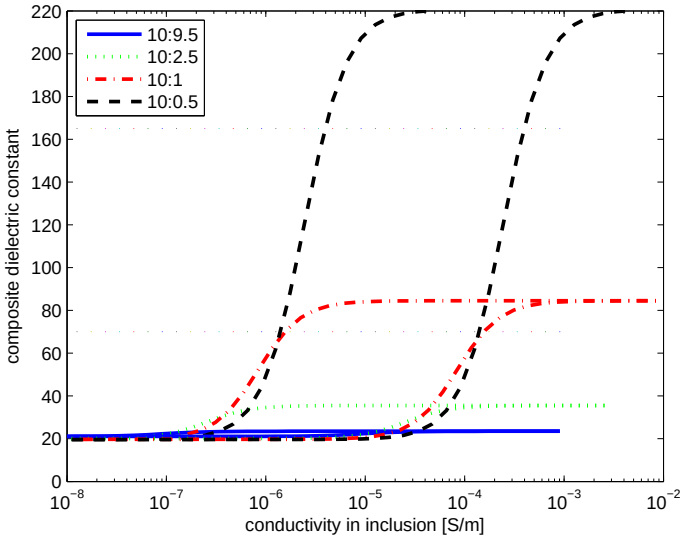

(b) Inferred dielectric constant of composite film

Figure A.3: Dielectric constant and loss tangent versus conductivity, a la Sillars, at 1 kHz and 100 kHz.

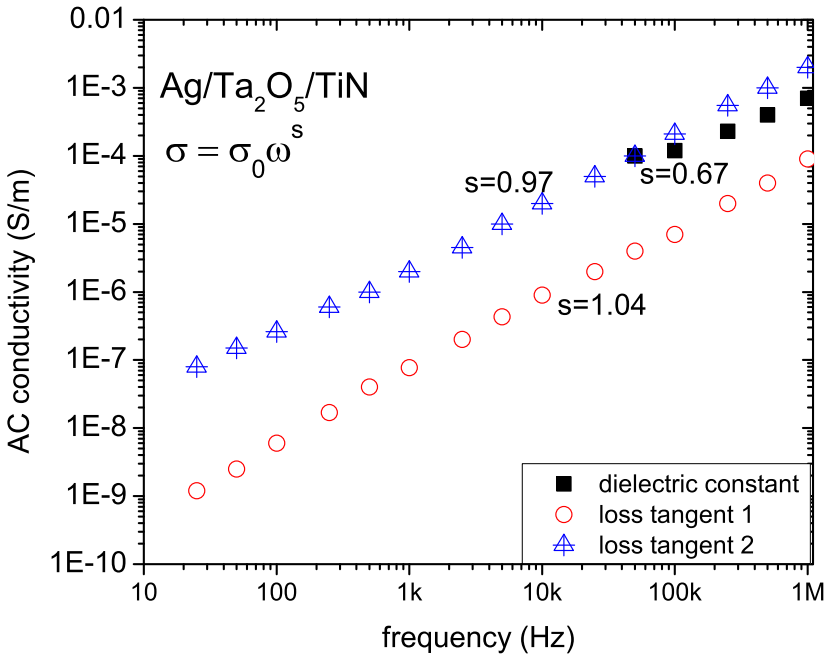

Figure A.4: Sillars AC conductivity versus frequency for $Ag/Ta_2O_5/TiN$ capacitors formed from lightly bombarded Ta_2O_5 in ambient storage. AC conductivities consistent with the observed dielectric constant and loss tangent are given.

results.

Figure A.5 gives the AC conductivities consistent with measurements on $Pt/Ta_2O_5/Pt$ capacitors. We find that the high frequency conductivities are very comparable to those of $Ag/Ta_2O_5/TiN$ capacitors, both in magnitude and frequency dependence, with $s = 0.70$ for conductivities related to the dielectric constant and $s = 0.78$ and $s = 1.2$ for the lower and higher conductivities consistent with loss tangent measurements, respectively. The response of the $Pt/Ta_2O_5/Pt$ and $Ag/Ta_2O_5/TiN$ capacitors diverge at lower frequencies. We note that the

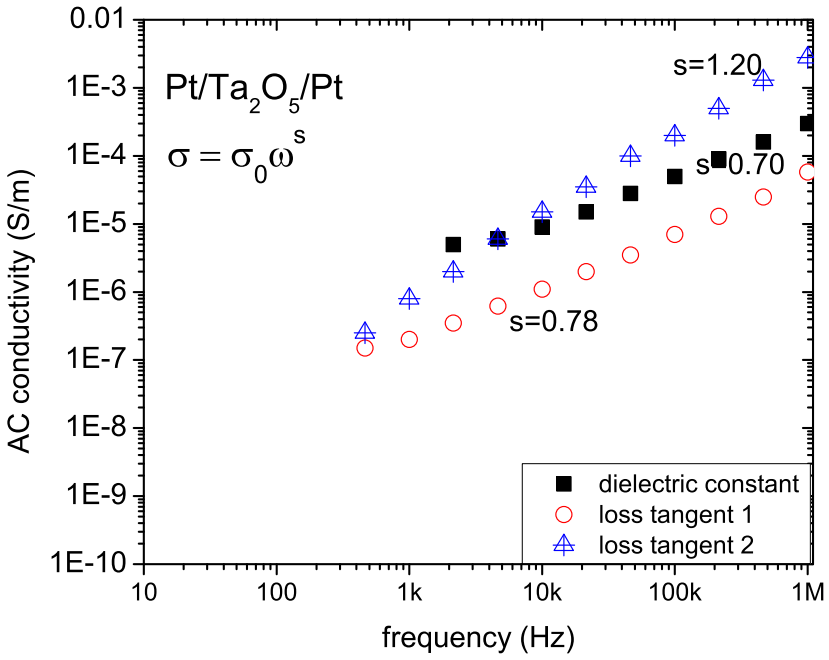

Figure A.5: Sillars AC conductivity versus frequency for $Pt/Ta_2O_5/Pt$ capacitors formed from lightly bombarded Ta_2O_5 in ambient storage. AC conductivities consistent with the observed dielectric constant and loss tangent are given.

difference in top electrode may limit the accessibility of pores to moisture adsorption. Additionally, the $Ag/Ta_2O_5/TiN$ capacitors were deposited ten years before the $Pt/Ta_2O_5/Pt$. While the vacuum chamber remained the same, the precise conditions of the sputtering target and substrate position are undoubtedly altered in the intervening years, as are the conditions of the older electrode and oxide films.

The AC conductivities plotted in Figures A.4 and A.5 require additional context. We do not give the conductivity of the composite Ta_2O_5-pore-water struc-

ture, but rather the conductivity within the pore that would be consistent with the measured dielectric response of the composite. We have assumed that the pore is full of water in ambient conditions. Both adsorbed water and condensed water are possible. Comparison to the conductivity of water is useful, then. The conductivity of pure water is 10^{-6} S/m, while that of salt water is 1 S/m [53]. The conductivity of adsorbed water is difficult to measure and depends on the type and concentration of charge carriers as well as their chemical environment. We suggest, however, that both the concentration of charge carriers and their mobility is less in adsorbed water than liquid water, representing a substantially smaller conductivity. Finally, we note that the conductivity of dense Ta_2O_5 can be as low as 5×10^{-12} S/m [154].

Conduction in adsorbed water is well-described by a hopping conduction of protons and H_3O^+ ions [122] and electrons [121]. Hopping conductivity along localized sites frequently exhibits a frequency dependence $\sigma = \sigma_o\omega^s$ for s close to but less than 1 [48], consistent with some of the behavior observed in Figures A.4 and A.5.

We acknowledge that the AC conductivities consistent with the measured dielectric constants are not identical to those consistent with the measured loss tangents. Sillars' derivation relies on assuming an ideal relationship between the dielectric constant and the loss tangent or imaginary part of the dielectric constant or the conductivity. In the real materials we analyze here, we imagine that additional, non-ideal loss mechanisms may contribute to the loss tangent.

We may hope to gain some insight into moisture adsorption by consulting literature on humidity sensors; see, for example, Ref. [121, 120, 110, 117]. The environmentally sensitive dielectric measurements presented in Chapter 5 dif-

fer from that of humidity sensor researchers, however, in that our dielectric measurements are made as a function of frequency at effectively two relative humidity levels: 0% (vacuum storage) and ~60% (ambient storage). In contrast, application as a humidity sensor necessitates measurements of dielectric response as a function of relative humidity at a single frequency.

Steele *et al.* [110] have fabricated a humidity sensor with a similar structure to our nanoporous Ta_2O_5. They evaporated alumina from an oblique evaporation source on to a rotating substrate and completed the capacitor structure with interdigitated electrodes which ensure a high oxide surface exposed to the atmosphere. They observe an exponential decrease in capacitance at 1 kHz with decreasing relative humidity (85% R.H. to 10% R.H., e.g.). The response time reported is 10s of milliseconds; the response time of our tantalum oxides has not been measured, but capacitance changes occur within 30 minutes and saturate within six hours. The difference in response time is likely due largely to the interdigitated electrodes and the difference in pore size, with larger pores (theirs at ~ 100 nm) leading to more rapid responses [110].

Khanna, Nahar, and Khockle [115, 119] have also used Sillars' analysis (Equations A.7 and A.8) to model the humidity-sensitive capacitive response of porous oxides. They use humidity-dependent adsorption levels to determine ε_2'. The experimental observations of capacitance and loss as a function of relative humidity are fit to Equations A.7 and A.8 using the conductivity within the pores as a fitting parameter. They find that their capacitance measurements are best fit for a distribution of conductivities, centered at $10^{-}5$ S/m at 120 Hz [115].

Other notes on using Sillars model

Sillars' model gives many insights into the effect of semiconducting inclusions to promote a lossy polarization. In particular, he demonstrates that inclusions elongated along the electric field axis have the strongest effect on enhancing the loss tangent and dielectric constant. The simple model employed, however, makes several assumptions that are not easily justified in the material system to which we apply it, namely nanoporous Ta_2O_5.

The first is that the model considers only the shape of the inclusions, not their absolute size. The width of these inclusions (<1 to 3 nm), however, approaches that at which the orientational polarization modes of adsorbed water may be constrained and the available conduction mechanisms vary with decreasing inclusion width. These issues may affect the values of the dielectric constant $\varepsilon_2' = 80$ and AC conductivity σ_2 within the voids.

The shape of the inclusion figures prominently in the calculating the electric field within the inclusion. The porosity is also important in the analysis of the field strength. In fact, the porosity (~6%) we consider is larger than that considered by Sillars, who assumed a sparsity of inclusions such that the enhanced electric field within an inclusion has no effect on neighboring inclusions. A more dense population of inclusions increases the electric field in each inclusion above that derived by Sillars [113]; the loss tangent he derives for the case of sparse inclusions is lower than that expected for a more dense population of inclusions.

We find that compensating for this error has opposite effects of the two AC conductivities derived for the same value of $\tan\delta$. From Figure A.1, we note

that increasing the measured loss tangent increases lower of the two conductivities and decreases the higher. Intuitively, we would argue that increases to the loss tangent should be the result of increases in conductivity, reinforcing our argument that we should consider the lower of the two conductivities consistent with the observed loss tangent.

Conclusions on Maxwell-Wagner-Sillars Polarization

A Maxwell-Wagner polarization in the inhomogeneous film of nanoporous Ta_2O_5 described in Chapter 5 has been described using Sillars' model of spheroidal semiconducting inclusions. We find that an AC conductivity in the inclusions of 5×10^{-8} to 10^{-6} S/m at 1 kHz gives rise to the observed enhancement to the inferred dielectric constant and loss tangent.

Limitations of applying Sillars' model to this material system and a comparison to complementary research in humidity sensors have also been discussed.

Finally, we note that this type of dielectric response attributed to interrupted semiconducting inhomogeneities is observed and exploited as a indicator in diverse materials systems and fields, perhaps most prominently in the earth sciences. For example, conductivity is common indicator of moisture content in soil [155], while inhomogeneities in sandstone give rise to a Maxwell-Wagner polarization [156].

BIBLIOGRAPHY

[1] K. Mistry, C. Allen, C. Auth, B. Beattie, D. Bergstrom, M. Bost, M. Brazier, M. Buehler, A. Cappellani, R. Chau, C.-H. Choi, G. Ding, K. Fischer, T. Ghani, R. Grover, W. Han, D. Hanken, M. Hattendorf, J. He, J. Hicks, R. Huessner, D. Ingerly, P. Jain, R. James, L. Jong, S. Joshi, C. Kenyon, K. Kuhn, K. Lee, H. Liu, J. Maiz, B. Mclntyre, P. Moon, J. Neirynck, S. Pae, C. Parker, D. Parsons, C. Prasad, L. Pipes, M. Prince, P. Ranade, T. Reynolds, J. Sandford, L. Shifren, J. Sebastian, J. Seiple, D. Simon, S. Sivakumar, P. Smith, C. Thomas, T. Troeger, P. Vandervoorn, S. Williams, and K. Zawadzki. A 45 nm logic technology with high-k+metal gate transistors, strained silicon, 9 Cu interconnect layers, 193 nm dry patterning, and 100 percent Pb free packaging. *Electron Devices Meeting, 2007. IEDM 2007. IEEE International*, pages 247–250, Dec. 2007.

[2] Antonio Facchetti, Myung-Han Yoon, and Tobin J. Marks. Gate dielectrics for organic field-effect transistors: New opportunities for organic electronics. *Advanced Materials*, 17(14):1705 – 1725, 2005. Polymeric organic materials;Organic thin-film transistors (OTFT);Radiofrequency identification (RFID);Electronic price tags;.

[3] K. Maex, M. R. Baklanov, D. Shamiryan, F. lacopi, S. H. Brongersma, and Z. S. Yanovitskaya. Low dielectric constant materials for microelectronics. *Journal of Applied Physics*, 93(11):8793–8841, 2003.

[4] Angus I. Kingon, Jon-Paul Maria, and S. K. Streiffer. Alternative dielectrics to silicon dioxide for memory and logic devices. *Nature*, 406:1032–1038, 2000.

[5] Robert M. Wallace and Glen Wilk. High-κ gate dielectric materials. *MRS Bulletin*, 27(3):192–197, March 2002.

[6] G. D. Wilk, R. M. Wallace, and J. M. Anthony. High-κ dielectrics: Current status and materials properties considerations. *Journal of Applied Physics*, 89(10):5243–5275, 2001.

[7] Clemens J. Först, Christopher R. Ashman, Karlheinz Schwarz, and Peter E. Blöchl. The interface between silicon and a high-k oxide, June 2008. `http://info.tuwien.ac.at/theochem/si-srtio3_interface/si-srtio3.html`.

[8] S.-H. Lo, D. A. Buchanan, Y. Taur, and W. Wang. Quantum-mechanical

modeling of electron tunneling current from the inversion layer of ultra-thin-oxide nMOSFETs. *IEEE Electron Device Letters*, 18(5):209–211, 1997.

[9] International Technology Roadmap for Semiconductors. ITRS Home Page, May 2007. `http://www.itrs.net`.

[10] D.A. Muller, T. Sorsch, S. Moccio, F.H. Baumann, K. Evans-Lutterodt, and G. Timp. Electronic structure at the atomic scale of ultrathin gate oxides. *Nature*, 399(6738):758 – 761, 1999.

[11] G. D. Wilk and R. M. Wallace. Stable zirconium silicate gate dielectrics deposited directly on silicon. *Applied Physics Letters*, 76(1):112–114, 2000.

[12] G. D. Wilk and R. M. Wallace. Electrical properties of hafnium silicate gate dielectrics deposited directly on silicon. *Applied Physics Letters*, 74(19):2854–2856, 1999.

[13] H. A. Kurtz and R. A. B. Devine. Role of bond coordination and molecular volume on the dielectric constant of mixed-oxide compounds. *Applied Physics Letters*, 79(15):2342, 2001.

[14] G. Lucovsky, Y. Wu, H. Niimi, H. Yang, J. Keister, and J. E. Rowe. Separate and independent reductions in direct tunneling in oxide/nitride stacks with monolayer interface nitridation associated with the (i) interface nitridation and (ii) increased physical thickness. *Journal of Vacuum Science & Technology A: Vacuum, Surfaces, and Films*, 18(4):1163–1168, 2000.

[15] A. Iqbal, W. B. Jackson, C. C. Tsai, J. W. Allen, and C. W. Bates, Jr. Electronic structure of silicon nitride and amorphous silicon/silicon nitride band offsets by electron spectroscopy. *Journal of Applied Physics*, 61(8):2947–2954, 1987.

[16] J. Kolodzey, E.A. Chowdhury, T.N. Adam, Guohua Qui, I. Rau, J.O. Olowolafe, J.S. Suehle, and Yuan Chen. Electrical conduction and dielectric breakdown in aluminum oxide insulators on silicon. *IEEE Transactions on Electron Devices*, 47(1):121–128, Jan 2000.

[17] Jiang Lu, Yue Kuo, and Jun-Yen Tewg. Hafnium-doped tantalum oxide high-k gate dielectrics. *Journal of The Electrochemical Society*, 153(5):G410–G416, 2006.

[18] M.-Y. Ho, H. Gong, G. D. Wilk, B. W. Busch, M. L. Green, W. H. Lin,

A. See, S. K. Lahiri, M. E. Loomans, Petri I. Räisänen, and T. Gustafsson. Suppressed crystallization of Hf-based gate dielectrics by controlled addition of Al_2O_3 using atomic layer deposition. *Applied Physics Letters*, 81(22):4218–4220, 2002.

[19] K. J. Hubbard and D. G. Schlom. Thermodynamic stability of binary oxides in contact with silicon. *Journal of Materials Research*, 11(11):2757 – 2776, 1996.

[20] Byoung Hun Lee, Laegu Kang, Renee Nieh, Wen-Jie Qi, and Jack C. Lee. Thermal stability and electrical characteristics of ultrathin hafnium oxide gate dielectric reoxidized with rapid thermal annealing. *Applied Physics Letters*, 76(14):1926–1928, 2000.

[21] O. Auciello, W. Fan, B. Kabius, S. Saha, J. A. Carlisles, R. P. H. Chang, C. Lopez, E. A. Irene, and R. A. Baragiola. Hybrid titanium-aluminum oxide layer as alternative high–k gate dielectric for the next generation of complementary metal-oxide-semiconductor devices. *Applied Physics Letters*, 86:042904, 2005.

[22] M. Li, Z. Zhang, S. A. Campbell, W. L. Gladfelter, M. P. Agustin, D. O. Klenov, and S. Stemmer. Electrical and material characterizations of high-permittivity $Hf_xTi_{1-x}O_2$ gate insulators. *Journal of Applied Physics*, 98(5):054506, 2005.

[23] Min Li, Zhihong Zhang, Stephen A. Campbell, Hong-Jyh Li, and Jeff J. Peterson. Hafnium titanate as a high permittivity gate insulator: Electrical and physical characteristics and thermodynamic stability. *Journal of Applied Physics*, 101(4):044509, 2007.

[24] R. B. van Dover. Amorphous lanthanide-doped TiO_x dielectric films. *Applied Physics Letters*, 74(20):3041–3043, May 17 1999.

[25] Tung-Ming Pan and Wei-Hao Shu. Structural and electrical characteristics of a high-*k* $NdTiO_3$ gate dielectric. *Applied Physics Letters*, 91:172904, 2007.

[26] Tung-Ming Pan and Wei-Hao Shu. Influence of titanium content on the structural and electrical properties of $Er_{1-x}Ti_xO_y$ gate dielectrics. *Journal of the Electrochemical Society*, 155:H247–H253, 2008.

[27] S. A. Campbell, H.-S. Kim, D. C. Gilmer, B. He, T. Ma, and W. L. Gladfelter. Titanium dioxide (TiO_2)-based gate insulators. *IBM Journal of Research and Development*, 43(3):383 – 392, 1999.

[28] R. A. McKee, F. J. Walker, and M. F. Chisholm. Physical structure and inversion charge at a semiconductor interface with a crystalline oxide. *Science*, 293(5529):468–471, 2001.

[29] B. El-Kareh, G. B. Bronner, and S. E. Schuster. The evolution of DRAM cell technology. *Solid State Technology*, 40(5):89–&, May 1997.

[30] I. Takeuchi, R. B. van Dover, and H. Koinuma. Combinatorial synthesis and evaluation of functional inorganic materials using thin-film techniques. *MRS Bulletin*, 27(4):301–308, Apr 2002.

[31] D. Brassard, M. A. El Khakani, and L. Ouellet. Substrate biasing effect on the electrical properties of magnetron-sputtered high-k titanium silicate thin films. *Journal of Applied Physics*, 102:034106, 2007.

[32] Byoung Hun Lee, Yongjoo Jeon, Keith Zawadzki, Wen-Jie Qi, and Jack Lee. Effects of interfacial layer growth on the electrical characteristics of thin titanium oxide films on silicon. *Applied Physics Letters*, 74(21):3143–3145, 1999.

[33] Milton Ohring. *Materials Science of Thin Films: Deposition and Structure*. Academic Press, San Diego, 2nd edition, 2002.

[34] Colin H. L. Goodman and Markus V. Pessa. Atomic layer epitaxy. *Journal of Applied Physics*, 60(3):R65–R82, 1986.

[35] S. M. George, O. Sneh, A. C. Dillon, M. L. Wise, A. W. Ott, L. A. Okada, and J. D. Way. Atomic layer controlled deposition of SiO_2 and Al_2O_3 using ABAB... binary reaction sequence chemistry. *Applied Surface Science*, 82-83:460–467, 1994.

[36] Brett W. Busch, Olivier Pluchery, Yves J. Chabal, David A. Muller, Robert L. Opila, J. Raynien Kwo, and Eric Garfunkel. Materials characterization of alternative gate dielectrics. *MRS Bulletin*, 27(3):206–211, March 2002.

[37] Mikko Ritala, Kaupo Kukli, Antti Rahtu, Petri I. Räisänen, Markku Leskelä, Timo Sajavaara, and Juhani Keinonen. Atomic layer deposition of oxide thin films with metal alkoxides as oxygen sources. *Science*, 288(5464):319–321, 2000.

[38] J. J. Cuomo and R. J. Gambino. Incorporation of rare gases in amorphous

sputtered metal films. *Journal of Vacuum Science & Technology*, 14(1):152–157, 1977.

[39] Do-Heyoung Kim, Sung-Lae Cho, Ki-Bum Kim, Jung Ju Kim, Jin Won Park, and Jae Jung Kim. Diffusion barrier performance of chemically vapor deposited TiN films prepared using tetrakis-dimethyl-amino titanium in the Cu/TiN/Si structure. *Applied Physics Letters*, 69(27):4182–4184, 1996.

[40] Thomas Unold, John Hautala, and J. David Cohen. Effect of carbon impurities on the density of states and the stability of hydrogenated amorphous silicon. *Physical Review B (Condensed Matter and Materials Physics)*, 50(23):16985–16994, Dec 1994.

[41] Raghavasimhan Sreenivasan, Paul C. McIntyre, Hyoungsub Kim, and Krishna C. Saraswat. Effect of impurities on the fixed charge of nanoscale HfO_2 films grown by atomic layer deposition. *Applied Physics Letters*, 89(11):112903, 2006.

[42] S. Van Elshocht, A. Hardy, T. Witters, C. Adelmann, M. Caymax, T. Conard, S. De Gendt, A. Franquet, O. Richard, M. K. Van Bael, J. Mullens, and M. Heyns. Aqueous chemical solution deposition. *Electrochemical and Solid-State Letters*, 10(4):G15–G17, 2007.

[43] S. Van Elshocht, A. Hardy, C. Adelmann, M. Caymax, T. Conard, A. Franquet, O. Richard, M. K. Van Bael, J. Mullens, and S. De Gendt. Impact of process optimizations on the electrical performance of high-k layers deposited by aqueous chemical solution deposition. *Journal of The Electrochemical Society*, 155(4):G91–G95, 2008.

[44] Richard P. Feynman, Robert B. Leighton, and Matthew Sands. *The Feynman Lectures on Physics: Mainly Electromagnetism and Matter*. Addison-Wesley Publishing Company, Reading, 1966.

[45] Charles Kittel. *Introduction to Solid State Physics*. John Wiley & Sons, Inc, 7th edition, 1996.

[46] Neil W. Ashcroft and N. David Mermin. *Solid State Physics*. Harcourt, 1976.

[47] Ion Bunget and Mihai Popescu. *Physics of Solid Dielectrics*, volume 19 of *Materials Science Monographs*. Elsevier, New York, 1984.

[48] A. K. Jonscher. *Dielectric Relaxation in Solids*. Chelsea Dielectrics Press, London, 1983.

[49] W. Kuang and S. O. Nelson. Low-frequency dielectric properties of biological tissues: A review with some new insights. *Transactions ASAE*, 41(1):173–184, 1998.

[50] Shang-Di Mo and W. Y. Ching. Electronic and optical properties of three phases of titanium dioxide: rutile, anatase, and brookite. *Physical Review B (Condensed Matter and Materials Physics)*, 51(19):13023–13032, May 1995.

[51] Don T. Cromer and K. Herrington. The structures of anatase and rutile. *Journal of the American Chemical Society*, 77(18):4708–4709, 1955.

[52] S. C. Barron and R. B. van Dover. Molecular volume and polarizability in the amorphous dielectric $Zr_{0.2}Sn_{0.2}Ti_{0.6}O_2$. In R. Ramesh, J.-P. Maria, M. Alexe, and V. Joshi, editors, *Ferroelectric Thin Films XIII*, pages 0902–T10–65, Warrendale, PA, 2006. Mater. Res. Soc. Symp. Proc.

[53] David R. Lide, editor. *CRC Handbook of Chemistry and Physics*. CRC Press / Taylor & Francis, Boca Raton, FL, 88th edition, 2007–2008 (Internet Version 2008).

[54] R. D. Shannon. Dielectric polarizabilities of ions in oxides and fluorides. *Journal of Applied Physics*, 73(1):348–366, 1993.

[55] S. O. Kasap. *Principles of Electronic Materials and Devices*. McGraw-Hill, 2nd edition, 2002.

[56] John Hevey. Optimization of in-situ oxidized TiDy dielectrics. Bachelors of Science, Materials Science and Engineering, Cornell University, Ithaca, NY, May 2007.

[57] Hewlett-Packard, LTD., Hyogo, Japan. *HP 4284A Precision LCR Meter Operation Manual*.

[58] R. M. Fleming, D. V Lang, C. D. W. Jones Jones, M. L. Steigerwald, D. W. Murphy, G. B. Alers Alers, Y.-H. Wong, R. B. van Dover, J. R. Kwo, and A. M. Sergent. Defect dominated charge transport in amorphous Ta_2O_5 thin films. *Journal of Applied Physics*, 88(2), 2000.

[59] S. Banerjee, B. Shen, I. Chen, J. Bohlman, G. Brown, and R. Doering. Conduction mechanisms in sputtered Ta_2O_5 on Si with an interfacial SiO_2 layer. *Journal of Applied Physics*, 65(3):1140 – 6, 1989/02/01.

[60] Leon I. Maissel and Reinhard Glang, editors. *Handbook of Thin Film Technology*. McGraw-Hill, 1st edition, 1970.

[61] M. Morita, T. Ohmi, E. Hasegawa, M. Kawakami, and M. Ohwada. Growth of native oxide on a silicon surface. *Journal of Applied Physics*, 11:1272–1281, 1990.

[62] R. B. van Dover, L. F. Schneemeyer, and R. M. Fleming. Discovery of a useful thin-film dielectric using a composition-spread approach. *Nature*, 392:162, 1998.

[63] R. B. van Dover and L. F. Schneemeyer. Deposition of uniform Zr-Sn-Ti-O films by on-axis reactive sputtering. *IEEE Electron Device Letters*, 19(9):329–331, Sep 1998.

[64] X. B. Lu, Y. P. Wang, H. Q. Ling, and Z. G. Liu. Dielectric properties of Zr-Sn-Ti-O thin films prepared by pulsed laser deposition. *Journal of Non-Crystalline Solids*, 303:88–93, 2002.

[65] O. Nakagawara, Y. Toyta, M. Kobayashi, Y. Yoshino, Y. Katayama, H. Tabata, and T. Kawai. title. *Journal of Applied Physics*, 80(3?):388, 1996.

[66] L. F. Edge, D. G. Schlom, R. T. Brewer, Y. J. Chabal, J. R. Williams, S. A. Chambers, C. Hinkle, G. Lucovsky, Y. Yang, S. Stemmer, M. Copel, B. Holländer, and J. Schubert. Suppression of subcutaneous oxidation during the deposition of amorphous lanthanum aluminate on silicon. *Applied Physics Letters*, 84(23):4629–4631, 2004.

[67] Shun-ichiro Ohmi, Hiroyuki Yamamoto, Junichi Taguchi, Kazuo Tsutsui, and Hiroshi Iwai. Effects of post dielectric deposition and post metallization annealing processes on metal/Dy_2O_3/Si(100) diode characteristics. *Japanese Journal of Applied Physics*, 43(4B), 2004.

[68] Hyelan Lee, Sanghun Jeon, and Hyunsang Hwang. Electrical characteristics of a Dy-doped HfO_2 gate dielectric. *Applied Physics Letters*, 79(16):2615–2617, 2001.

[69] M. Acosta, O. Ares, Victor Sosa, C. Acosta, and J. L. Peña. Influence of the

sputtering variables in the ion bombardment during off-axis deposition of $YBa_2Cu_3O_x$ films. *Journal of Vacuum Science & Technology A: Vacuum, Surfaces, and Films*, 17(5):2879–2884, 1999.

[70] Yi Zhao, Masahiro Toyama, Koji Kita, Kentaro Kyuno, and Akira Toriumi. Moisture-absorption-induced permittivity deterioration and surface roughness enhancement of lanthanum oxide films on silicon. *Applied Physics Letters*, 88(7):072904, 2006.

[71] K. K. Ho and G. P. Carman. Sputter deposition of NiTi thin film shape memory alloy using a heated target. *Thin Solid Films*, 370(1-2):18–29, Jul 17 2000.

[72] Ken K. Ho, Gregory P. Carman, and K.P. Mohanchandra. Examination of the sputtering profile of NiTi under target heating conditions. *Thin Solid Films*, 413(1-2):1 – 7, 2002.

[73] J. P. Biersack and W. Eckstein. Sputtering studies with the Monte Carlo program TRIM.SP. *Applied Physics A: Solids and Surfaces*, A34(2):73 – 94, 1984.

[74] C.S. Kang, H.J. Cho, K. Onishi, R. Nieh, R. Choi, S. Gopalan, S. Krishnan, J.H. Han, and J.C. Lee. Bonding states and electrical properties of ultrathin HfO_xN_y gate dielectrics. *Applied Physics Letters*, 81(14):2593–2595, Sep 30 2002.

[75] Kyu-Jeong Choi, Jeon-Ho Kim, and Soon-Gil Yoon. Characterization of HfO_2 and HfO_xN_y gate dielectrics grown by PE Metallorganic CVD with a TaN gate electrode. *Journal of The Electrochemical Society*, 151(4):G262–G265, 2004.

[76] S. Strite and H. Morkoc. GaN, AlN, and InN: A review. *Journal of Vacuum Science & Technology B: Microelectronics and Nanometer Structures*, 10(4):1237–1266, 1992.

[77] A. Chatterjee, R.A. Chapman, G. Dixit, J. Kuehne, S. Hattangady, H. Yang, G.A. Brown, R. Aggarwal, U. Erdogan, Q. He, M. Hanratty, D. Rogers, S. Murtaza, S.J. Fang, R. Kraft, A.L.P. Rotondaro, J.C. Hu, M. Terry, W. Lee, C. Fernando, A. Konecni, G. Wells, D. Frystak, C. Bowen, M. Rodder, and I.-C. Chen. Sub-100 nm gate length metal gate NMOS transistors fabricated by a replacement gate process. *Electron Devices Meeting, 1997. IEDM '97. Technical Digest., International*, pages 821–824, Dec 1997.

[78] Zhiyong Li, Patricia Beck, Douglas A.A. Ohlberg, Duncan R. Stewart, and R. Stanley Williams. Surface properties of platinum thin films as a function of plasma treatment conditions. *Surface Science*, 529(3):410 – 418, 2003.

[79] A. Grill, W. Kane, J. Viggiano, M. Brady, and R. Laibowitz. Base electrodes for high dielectric constant oxide materials in silicon technology. *Journal of Materials Research*, 7(12):3260 – 3265, 1992.

[80] K. V. Rao and A. Smakula. Dielectric properties of cobalt oxide, nickel oxide, and their mixed crystals. *Journal of Applied Physics*, 36(6):2031–2038, 1965.

[81] Kaupo Kukli, Titta Aaltonen, Jaan Aarik, Jun Lu, Mikko Ritala, Sandro Ferrari, Anders Hrsta, and Markku Leskelä. Atomic layer deposition and characterization of HfO_2 films on noble metal film substrates. *Journal of The Electrochemical Society*, 152(7):F75–F82, 2005.

[82] Chun-Kai Huang, Yan-Kai Chiou, Yan-Chang Chu, Tai-Bor Wu, and Cho-Jen Tsai. Enhancement in ferroelectric properties of $Pb(Zr_{0.4}Ti_{0.6})O_3$ thin-film capacitors with PtO_x electrodes. *Journal of The Electrochemical Society*, 153(6):F115–F119, 2006.

[83] Bing-Yue Tsui and Hsiu-Wei Chang. Formation of interfacial layer during reactive sputtering of hafnium oxide. *Journal of Applied Physics*, 93(12):10119–10124, 2003.

[84] A. Callegari, E. Cartier, M. Gribelyuk, H. F. Okorn-Schmidt, and T. Zabel. Physical and electrical characterization of hafnium oxide and hafnium silicate sputtered films. *Journal of Applied Physics*, 90(12):p6466 – 6475, 20011215.

[85] M Kadoshima, M Hiratani, Y Shimamoto, K Torii, H Miki, S Kimura, and T Nabatame. Rutile-type TiO_2 thin film for high-k gate insulator. *Thin Solid Films*, 424(2):224–228, JAN 31 2003.

[86] Shriram Ramanathan, Glen D. Wilk, David A. Muller, Chang-Man Park, and Paul C. McIntyre. Growth and characterization of ultrathin zirconia dielectrics grown by ultraviolet ozone oxidation. *Applied Physics Letters*, 79(16):2621–2623, 2001.

[87] T. Busani and R. A. B. Devine. Molecular volume and electronic and vibrational polarizibilities for amorphous $LaAlO_3$. *Journal of Applied Physics*, 96(11):6642–6647, 2004.

[88] Kazuhiko Yamamoto, Shigenori Hayashi, Masafumi Kubota, and Masaaki Niwa. Effect of Hf metal predeposition on the properties of sputtered HfO_2/Hf stacked gate dielectrics. *Applied Physics Letters*, 81(11):2053–2055, 2002.

[89] F.F.C. Duval, R.A. Dorey, R.H. Haigh, and R.W. Whatmore. Stable TiO_2/Pt electrode structure for lead containing ferroelectric thick films on silicon MEMS structures. *Thin Solid Films*, 444(1-2):235 – 40, 2003/11/01.

[90] Jin Kun Lan, Ying Lang Wang, Chuan-Pu Liu, Chuen Guang Chao, Chyung Ay, Chi Wen Liu, and Yi Lung Cheng. Mechanisms of circular defects for shallow trench isolation oxide deposition. *Journal of Vacuum Science & Technology B: Microelectronics and Nanometer Structures*, 21(5):2098–2104, 2003.

[91] Zong-Jian Liu, Ning Jiang, Y. G. Shen Shen, and Xiaonian Li. Stress-induced surface damages in TiSiN films grown by magnetron sputtering. *Thin Solid Films*, 516:7609 – 7614, 2008.

[92] J. C. Bean, G. E. Becker, P. M. Petroff, and T. E. Seidel. Dependence of residual damage on temperature during Ar^+ sputter cleaning of silicon. *Journal of Applied Physics*, 48(3):907–913, 1977.

[93] U. Bangert, P. J. Goodhew, C. Jeynes, and I. H. Wilson. Low-energy (2-5 keV) argon damage in silicon. *Journal of Physics D: Applied Physics*, 19(4):589–603, 1986.

[94] M. Bulanova, Yu. Podrezov, Yu. Fartushnaya, K. Meleshevich, and A. Samelyuk. Structure and properties of as-cast Ti-Dy alloys. *Journal of Alloys and Compounds*, 370:L10–L13, 2004.

[95] Seung-Ik Jun, Philip D. Rack, Timothy E. McKnight, Anatoli V. Melechko, and Michael L. Simpson. Electrical and microstructural characterization of molybdenum tungsten electrodes using a combinatorial thin film sputtering technique. *Journal of Applied Physics*, 97(5):054906, 2005.

[96] J. W. Coburn and Eric Kay. Positive-ion bombardment of substrates in rf diode glow discharge. *Journal of Applied Physics*, 43(12):4965–4971, 1972.

[97] R. B. van Dover, M. L. Green, L. Manchanda, L. F. Schneemeyer, and T. Siegrist. Composition-dependent crystallization of alternative gate dielectrics. *Applied Physics Letters*, 83(7):1459 – 1461, 2003.

[98] Shriram Ramanathan, Paul C. McIntyre, Supratik Guha, and Evgeni Gusev. Charge trapping studies on ultrathin ZrO_2 and HfO_2 high-k dielectrics grown by room temperature ultraviolet ozone oxidation. *Applied Physics Letters*, 84(3):389 – 391, 2004. Charge trapping (CT);Gate electrodes;.

[99] V. Edon, M.C. Hugon, B. Agius, L. Miotti, C. Radtke, F. Tatsch, J.J. Ganem, I. Trimaille, and I.J.R. Baumvol. Effects of sputter deposition parameters and post-deposition annealing on the electrical characteristics of $LaAlO_3$ dielectric films on Si. *Applied Physics A (Materials Science Processing)*, A83(2):289 – 93, 2006.

[100] P. Sivasubramani, J. Kim, M.J. Kim, B.E. Gnade, and R.M. Wallace. Effect of nitrogen incorporation on the thermal stability of sputter deposited lanthanum aluminate dielectrics on Si (100). *Applied Physics Letters*, 89(15):152903 – 1, 2006.

[101] N. N. Iosad, G. J. Ruis, E. V. Morks, A. F. Morpurgo, N. M. van der Pers, P. F. A. Alkemade, and V. G. M. Sivel. Dielectric properties of sputtered transition metal oxides. *Journal of Applied Physics*, 15(12):8087–8091, 2004.

[102] A. P. Huang, Paul K. Chu, H. Yan, and M. K. Zhu. Dielectric properties enhancement of ZrO_2 thin films induced by substrate biasing. *Journal of Vacuum Science & Technology, B*, 23(2), 2005.

[103] Orlando Auciello and Roger Kelly, editors. *Ion bombardment modification of surfaces: Fundamentals and applications*, volume 1 of *Beam modification of materials*. Elsevier Science Publishers, New York, 1984.

[104] C. Chaneliere, J. L. Autran, R. A. B. Devine, and B. Balland. Tantalum pentoxide (Ta_2O_5) thin films for advanced dielectric applications. *Materials Science and Engineering Reports*, R22:269–322, 1998.

[105] I. Petrov, L. Hultman, J.-E. Sundgren, and J. E. Greene. Polycrystalline tin films deposited by reactive bias magnetron sputtering: Effects of ion bombardment on resputtering rates, film composition, and microstructure. *Journal of Vacuum Science & Technology A: Vacuum, Surfaces, and Films*, 10(2):265–272, 1992.

[106] K. H. Muller. Stress and microstructure of sputter-deposited of thin films – molecular-dynamics investigations. *Journal of Applied Physics*, 62(5):1796–1799, Sep 1 1987.

[107] Tomoyoshi Motohiro and Y. Taga. Thin film retardation plate by oblique deposition. *Applied Optics*, 28(13):2466–2482, 1989.

[108] D. Le Bellac, A. Azens, and C. G. Granqvist. Angular selective transmittance through electrochromic tungsten oxide films made by oblique angle sputtering. *Applied Physics Letters*, 6(14):1715–1717, 1995.

[109] K. Robbie, D.J. Broer, and M.J. Brett. Chiral nematic order in liquid crystals imposed by an engineered inorganic nanostructure. *Nature*, 399(6738):764 – 766, 1999.

[110] John J. Steele, James P. Gospodyn, Jeremy C. Sit, and Michael J. Brett. Impact of morphology on High-Speed humidity sensor performance. *IEEE Sensors Journal*, 6(1):24–27, 2006.

[111] D. W. Hoffman and John A. Thorton. Effects of substrate orientation and rotation on internal stresses in sputtered metal films. *Journal of Vacuum Science & Technology*, 16(2), 1978.

[112] Maxim M. Noginov. Fabrication of complex amorphous high-k dielectric materials. Masters of Engineering, Applied Physics, Cornell University, Ithaca, NY, May 2008.

[113] R. W. Sillars. Properties of a dielectric containing semi-conducting particles of various shapes. *Journal of the Institution of Electrical Engineers*, 80:378 – 394, 1937.

[114] R. K. Nahar and V. K. Khanna. A study of capacitance and resistance characteristics of an Al_2O_3 humidity sensor. *International Journal of Electronics*, 52(6):p557 –, 19820601.

[115] V. K. Khanna and R. K. Nahar. Effect of moisture on the dielectric properties of porous alumina films. *Sensors and Actuators*, 5(3):187 – 198, 1984.

[116] E. McCafferty and A. C. Zettlemoyer. Adsorption of water vapour on α-Fe_2O_3. *Discuss. Faraday Soc.*, 52:239–254, 1971.

[117] Tsuneharu Nitta, Ziro Terada, and Shigeru Hayakawa. Humidity-sensitive electrical conduction of $MgCr_2O_4$-TiO_2 porous ceramics. *Journal of the American Ceramic Society*, 63(5-6):295–300, 1980.

[118] D. Beaglehole and H. K. Christenson. Vapor adsorption on mica and silicon: entropy effects, layering, and surface forces. *Journal of Physical Chemistry*, 96(8):3395–3403, 1992.

[119] R. K. Nahar, V. K. Khanna, and W. S. Khokle. On the origin of the humidity-sensitive electrical properties of porous aluminium oxide (sensor application). *Journal of Physics D: Applied Physics*, 17(10):2087–2095, 1984.

[120] Enrico Traversa. Ceramic sensors for humidity detection: the state-of-the-art and future developments. *Sensors and Actuators B: Chemical*, 23(2-3):135–156, 1995.

[121] Zhi Chen and Chi Lu. Humidity sensors: A review of materials and mechanisms. *Sensor Letters*, 3:274–295, 2005.

[122] James Hunter Anderson and George A. Parks. Electrical conductivity of silica gel in the presence of adsorbed water. *Journal of Physical Chemistry*, 72(10):3662–3668, 1968.

[123] Abbe T. Kohl, Richard Mimna, Robert Shick, Larry Rhodes, Z. L. Wang, and Paul A. Kohl. Low k, porous methyl silsesquioxane and Spin-On-Glass. *Electrochemical and Solid-State Letters*, 2(2):77–79, 1999.

[124] J. M. Gregoire, M. B. Lobovsky, M. F. Heinz, F. J. DiSalvo, and R. B. van Dover. Resputtering phenomena and determination of composition in codeposited films. *Physical Review B (Condensed Matter and Materials Physics)*, 76(19):195437, 2007.

[125] J. M. Gregoire and R. B. van Dover. A model for calculating resputter rates in codeposition. *54th International AVS Symposium*, 26(4):1030–1036, 2008.

[126] Jack R. Tessman, A. H. Khan, and William Shockley. Electronic polarizabilities of ions in crystals. *Physical Review*, 92(4):890 – 895, 1953.

[127] G. N. Strauss, W. Lechner, and H. K. Pulker. Gas pressures influence on the optical and mechanical properties of ta2o5 films produced by reactive low voltage ion plating (rlvip). *Thin Solid Films*, 351(1-2):53 – 56, 1999.

[128] T. Dimitrova, K. Arshak, and E. Atanassova. Crystallization effects in oxygen annealed Ta_2O_5 thin films on Si. *Thin Solid Films*, 381(1):31 – 38, 2001.

[129] R. B. van Dover. Deposition temperatures and dielectric properties in the ZrO_2-SnO_2-TiO_2 system. Unpublished, 1998.

[130] L. Manchanda, M. D. Morris, M. L. Green, R. B. van Dover, F. Klemens, T. W. Sorsch, P. J. Silverman, G. Wilk, B. Busch, and S. Aravamudhan. Multi-component high-K gate dielectrics for the silicon industry. *Microelectronic Engineering*, 59(1-4):351 – 359, 2001.

[131] X. D. Xiang, Xiaodong Sun, Gabriel Briceno, Yulin Lou, Kai-An Wang, Hauyee Chang, William G. Wallace-Freedman, Sung-Wei Chen, and Peter G. Schultz. A combinatorial approach to materials discovery. *Science*, 268(5218):1738–1740, 1995.

[132] J. J. Hanak. The "multiple-sample concept" in materials research: synthesis, compositional analysis, and testing of entire multicomponent system. *Journal of Materials Science*, pages 964–971, 1970.

[133] R. B. van Dover and L. F. Schneemeyer. The codeposited composition spread approach to high-throughput discovery/exploration of inorganic materials. *Macromolecular Rapid Communications*, 25(1):150–157, Jan 2 2004.

[134] R. B. van Dover, L. F. Schneemeyer, R. M. Fleming, and H. A. Huggins. A high-throughput search for electronic materials thin-film dielectrics. *Biotechnology and Bioengineering*, 61(4):217–225, 1999.

[135] H. M. Christen, S. D. Silliman, and K. S. Harshavardhan. Continuous compositional-spread technique based on pulsed-laser deposition and applied to the growth of epitaxial films. *Review of Scientific Instruments*, 72(6):2673–2678, 2001.

[136] Christoph Schmitz, Mukundan Thelakkat, and Hans-Werner Schmidt. A combinatorial study of the dependence of organic LED characteristics on layer thickness. *Advanced Materials*, 11(10):821–826, 1999.

[137] Ki Woong Kim, Min Ku Jeon, Kwang Seok Oh, Tai Suk Kim, Yun Seok Kim, and Seong Ihl Woo. Combinatorial approach for ferroelectric material libraries prepared by liquid source misted chemical deposition method. *Proceedings of the National Academy of Sciences*, 104(4):1134–1139, 2007.

[138] Karen Elizabeth Downey. *A continuous composition spread approach to synthesizing and screening Er^{3+} oxide host materials sutiable for use as planar opti-*

cal amplifiers. PhD, Materials Science and Engineering, Cornell University, Ithaca, NY, August 2007.

[139] Yuqing Yu. Composition and dielectric properties of cosputtered polycrystalline (barium, strontium) titanium oxide thin films by continuous composition spread method. Masters of Science, Materials Science and Engineering, Cornell University, Ithaca, NY, May 2005.

[140] Mark Prochaska, Jing Jin, Dominic Rochefort, Lin Zhuang, Francis J. Disalvo, Hector D. Abruña, and R.B. van Dover. High throughput screening of electrocatalysts for fuel cell applications. *Review of Scientific Instruments*, 77(5):054104, 2006.

[141] Mark Prochaska. *Use of a combinatorial search for the discovery of new fuel cell anode electrocatalysts*. PhD, Applied Physics, Cornell University, Ithaca, NY, May 2007.

[142] John M. Gregoire, R. B. van Dover, Jing Jin, Francis J. Disalvo, and Hector D. Abruña. Getter sputtering system for high-throughput fabrication of composition spreads. *Review of Scientific Instruments*, 78(7):072212 –, 2007.

[143] Noble C. Woo, Bryan G. Ng, and R. Bruce van Dover. High-throughput combinatorial study of local stress in thin film composition spreads. *Review of Scientific Instruments*, 78(7):072208, 2007.

[144] K. E. Downey, R. B. van Dover, A. Bhagwat, and A. Gaeta. Combinatorial exploration of novel thin film amorphous oxides. *Conference on Lasers and Electro-Optics (CLEO), 2005*, pages 77 – 79, 2005.

[145] Yoshiki Kamata. High-k/Ge MOSFETs for future nanoelectronics. *Materials Today*, 11(1-2), 2008.

[146] Minjoo L. Lee, Eugene A. Fitzgerald, Mayank T. Bulsara, Matthew T. Currie, and Anthony Lochtefeld. Strained Si, SiGe, and Ge channels for high-mobility metal-oxide-semiconductor field-effect transistors. *Journal of Applied Physics*, 97(1):011101, 2005.

[147] Chi On Chui, Hyoungsub Kim, P. C. McIntyre, and K. C. Saraswat. A germanium NMOSFET process integrating metal gate and improved high-κ dielectrics. *IEEE International Electron Devices Meeting (IEDM), 2003*, pages 18.3.1–18.3.4, Dec. 2003.

[148] Tatsuro Maeda, Tetsuji Yasuda, Masayasu Nishizawa, Noriyuki Miyata, Yukinori Morita, and Shinichi Takagi. Ge metal-insulator-semiconductor structures with Ge_3N_4 dielectrics by direct nitridation of Ge substrates. *Applied Physics Letters*, 85(15):3181–3183, 2004.

[149] Yohei Otani, Yasuhiro Itayama, Takuo Tanaka, Yukio Fukuda, Hiroshi Toyota, Toshiro Ono, Minoru Mitsui, and Kiyokazu Nakagawa. Fabrication of Ta_2O_5/GeN_x gate insulator stack for Ge metal-insulator-semiconductor structures by electron-cyclotron-resonance plasma nitridation and sputtering deposition techniques. *Applied Physics Letters*, 90(14):142114, 2007.

[150] Cornell Fuel Cell Institute. Resputter calculator, June 2008. `http://www.cfci.ccmr.cornell.edu/resputter.html`.

[151] C. Corbella, M. Vives, A. Pinyol, I. Porqueras, C. Person, and E. Bertran. Influence of the porosity of RF sputtered Ta_2O_5 thin films on their optical properties for electrochromic applications. *Solid State Ionics*, 165(1-4):15 – 22, 2003.

[152] Z.-Y. Yin and B. K. Garside. Low-loss GeO_2 optical waveguide fabrication using low deposition rate rf sputtering. *Applied Optics*, 21:4324–4328, December 1982.

[153] D. Crouse, Yu-Hwa Lo, A. E. Miller, and M. Crouse. Self-ordered pore structure of anodized aluminum on silicon and pattern transfer. *Applied Physics Letters*, 76(1):49–51, 2000.

[154] B. K. Moon, J. Aoyama, and K. Katori. Ultrathin and highly insulating amorphous-Ta_2O_5 films formed on Ru/TiN/Ti/n(+)-Si substrates. *Applied Physics Letters*, 74(6):824–826, Feb 8 1999.

[155] J. D. Rhoades, P. A. C. Raats, and R. J. Prather. Effects of liquid-phase electrical conductivity, water content, and surface conductivity on bulk soil electrical conductivity. *Soil Science Society of America Journal*, 40(5):651–655, 1976.

[156] Rosemary J. Knight and Amos Nur. The dielectric constant of sandstones, 60 kHz to 4 MHz. *Geophysics*, 52(5):644–654, 1987.